ISSN 1590-8844
Vol. 17 No 02
2016

International Journal of Mechanics and Control

Editor: Andrea Manuello Bertetto

Scopus Indexed Journal

Reference Journal of IFToMM Italy
International Federation for the Promotion of Mechanism and Machine Science

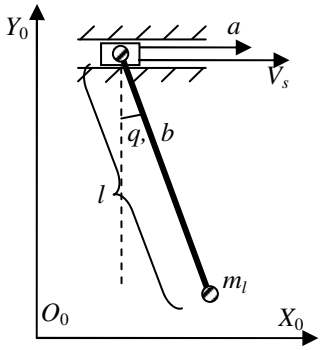

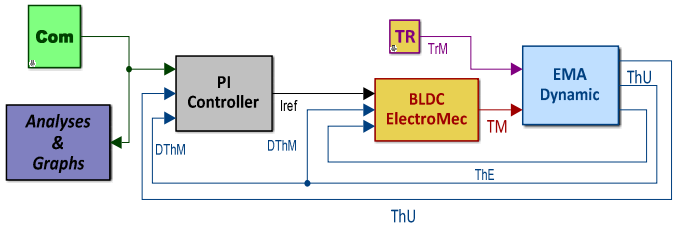

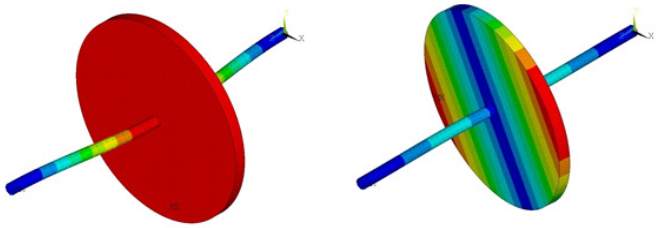

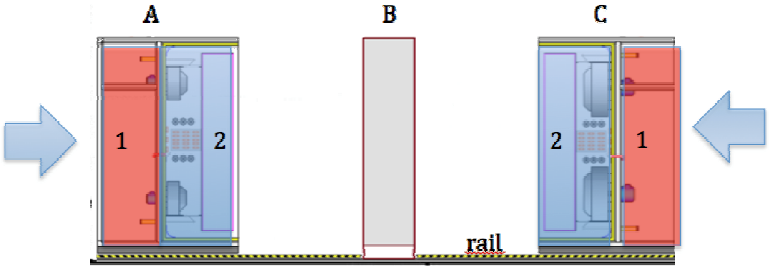

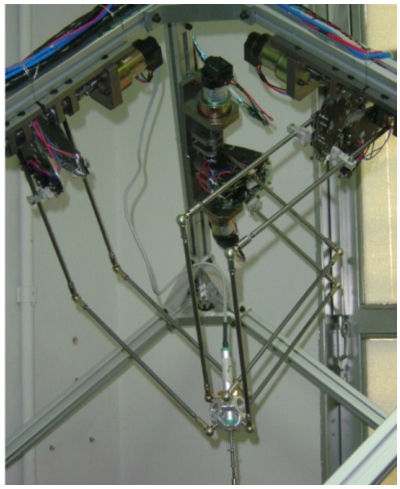

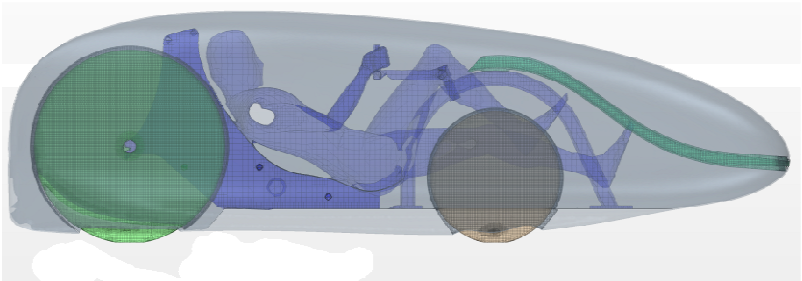

LIBRERIA EDITRICE UNIVERSITARIA
LEVROTTO & BELLA
TORINO

Official Torino Italy Court Registration
n.5390, 5th May 2000

Deposito presso il Tribunale di Torino
numero 5390 del 5 maggio 2000
Direttore responsabile:
Andrea Manuello Bertetto

International Journal of Mechanics and Control

The Journal is addressed to scientists and engineers who work in the fields of mechanics (mechanics, machines, systems, control, structures). It is edited in Turin (Northern Italy) by Levrotto&Bella Co., with an international board of editors. It will have not advertising.

Turin has a great and long tradition in mechanics and automation of mechanical systems. The journal would will to satisfy the needs of young research workers of having their work published on a qualified paper in a short time, and of the public need to read the results of researches as fast as possible.

Interested parties will be University Departments, Private or Public Research Centres, Innovative Industries.

Aims and scope

The *International Journal of Mechanics and Control* publishes as rapidly as possible manuscripts of high standards. It aims at providing a fast means of exchange of ideas among workers in Mechanics, at offering an effective method of bringing new results quickly to the public and at establishing an informal vehicle for the discussion of ideas that may still in the formative stages.

Language: English

International Journal of Mechanics and Control will publish both scientific and applied contributions. The scope of the journal includes theoretical and computational methods, their applications and experimental procedures used to validate the theoretical foundations. The research reported in the journal will address the issues of new formulations, solution, algorithms, computational efficiency, analytical and computational kinematics synthesis, system dynamics, structures, flexibility effects, control, optimisation, real-time simulation, reliability and durability. Fields such as vehicle dynamics, aerospace technology, robotics and mechatronics, machine dynamics, crashworthiness, biomechanics, computer graphics, or system identification are also covered by the journal.

Please address contributions to

Prof. Andrea Manuello Bertetto
PhD Eng. Matteo D. L. Dalla Vedova

Dept. of Mechanical and Aerospace Engineering
Politecnico di Torino
C.so Duca degli Abruzzi, 24.
10129 - Torino - Italy - E.C.

www.jomac.it
e_mail: jomac@polito.it

Subscription information

Subscription order must be sent to
the publisher:

Libreria Editrice Universitaria
Levrotto&Bella
C.so Luigi Einaudi 57/c – 10129 Torino – Italy

www.levrotto-bella.net
e_mail: info@levrotto-bella.net
ph.: +39 011 4275423
mob.: +39 328 5369063
fax: +39 011 4275425

ISSN 1590-8844
International Journal of Mechanics and Control, Vol. 17, No. 02, 2016

REGRESSION MODEL OF REDUCING OF PENDULUM OSCILLATIONS OF LOAD MOVED BY MEANS OF OVERHEAD CRANE WITH RELAY DRIVE

Mikhail S. Korytov* Vitaly S. Shcherbakov* Irina V. Breus*

* Siberian State Automobile and Highway academy (SibADI)

ABSTRACT

With the result of conducted research we obtain the dependencies of acceleration and time of accelerated movement of point of suspension load and also deviation angle of overhead crane rope, by which it is necessary to start braking of suspension point, providing complete reducing of pendulum oscillations of load with simultaneous full stop point of suspension from the initial velocity of the point of suspension and the maximum angle of deflection of the hoist rope. We use simulation model of overhead crane and the simplex method of optimization for these dependencies. The obtained dependences are used to do regression model of reducing of pendulum oscillations of load moved by means of overhead crane with relay drive.

Keywords: regression model, overhead crane, drive

1 INTRODUCTION

It is necessary to damp the residual load pendulum oscillations [1-6] to increase the productivity of overhead cranes (OC) with relay drive. Additional start-up motor drive relay OC causes large inrush currents reducing the service period of the electric engine [7].

It is possible to increase the productivity of overhead cranes by reducing of load pendulum oscillations on flexible rope suspension after its delivery to the aim position.

The well-known methods of load residual oscillations damping [2, 3, 4, 5, 6, 8, 9] have general disadvantages in the authors understanding. They are: complication of implemented mathematical methods and models as well as rather big accuracy of linear coordinates of moved load realization. Uncontrolled component part of pendulum oscillations of load is put down partly. As a rule, the time of displacement by oscillation damping is increasing.

In presented work we set the task to show the possibility of making of rather simple regression model of full load flat pendulum oscillation damping. This load is moved by means of overhead crane with relay drive.

Contact authors: Mikhail Korytov [1], Vitaly Shcherbakov [1]

[1]644080, Omsk, prospect Mira 5, Russian Federation.
E-mail: kms142@mail.ru

It allows to calculate optimum values of acceleration and braking time of load suspension point in real time regime. Damping of load pendulum oscillations on rope suspension must be implemented for current (measured) values of angle of load rope OC deflection from vertical line and motion speed of suspension point.

2 MATERIALS AND METHODS

In this regard, the experimental researches are carried out using a simulation model OC [10]. Researches are connected with pendulum oscillation of the load along one of the coordinates of three-dimensional space by a single braking suspension point until its complete stop by optimizing the values of the deflection angle of the hoist rope from the vertical q_{bb}, where it is optimal to produce the beginning of the braking (bb) of load suspension point, duration of braking ΔT_{brak} and acceleration of braking, a_{brak}. The authors accept that that the speedup of acceleration and deceleration of the suspension point are constant and linear speed of the suspension point in the steady state (after completion of acceleration and before braking) is also constant. The settlement scheme of the OC dynamic system and the corresponding simulation model in the notation SimMechanics Second Generation and Simulink are shown in Figure 1.

Using a simulation model OC with load by means of variation of the speedup of acceleration a_{acc} and acceleration time ΔT_{acc} within the limits

$$a_{acc} = (0{,}25{:}0{,}25{:}2{,}5)\ [\text{m/s}^2];\ T_{acc} = (0{,}25{:}0{,}25{:}2{,}5)\ [\text{s}] \quad (1)$$

it was formed two-dimensional arrays of suspension point speed previous the start time of braking $V_s = f(a_{acc}, \Delta T_{acc})$, the maximum angle of deviation of load rope OC from vertical, previous the beginning of the braking time $q_{max}=f(a_{acc}, \Delta T_{acc})$, the optimal value of the angle of deviation of load rope from the vertical q_{bb} during which we have the beginning of braking of suspension point $q_{bb}=f(a_{acc}, \Delta T_{acc})$, optimal duration of braking $\Delta T_{brak}=f(a_{acc},\Delta T_{acc})$ and optimal constant value of the braking acceleration $a_{brak}= f(a_{acc}, \Delta T_{acc})$.

Length of a hoist rope accepted value l=10 [m], mass of load m_l=100 [kg], damping coefficient on angular coordinate b=100 [N·m/(rad/s)]. Each element of the array $q_{bb} = f(a_{acc}, \Delta T_{acc})$, $\Delta T_{brak}=f(a_{acc}, \Delta T_{acc})$, $a_{brak} = f(a_{acc}, T_{acc})$ was formed as a result of solving the problem of optimizing the values of the parameters defining the braking process (q_{bb}, ΔT_{brak}, a_{brak}) by means of simplex method by the criterion of minimization of indicator

$$y = \dot{q}_{res} + V_{sres} + \Delta y, \quad (2)$$

where the $\dot{q}_{res}$ – maximum residual velocity of angle changing of deflection of hoist rope from the vertical after the moment of ceasing of braking; V_{sres} – maximum residual velocity of the point of load suspension after the moment of ceasing of braking; Δy – penalty function.

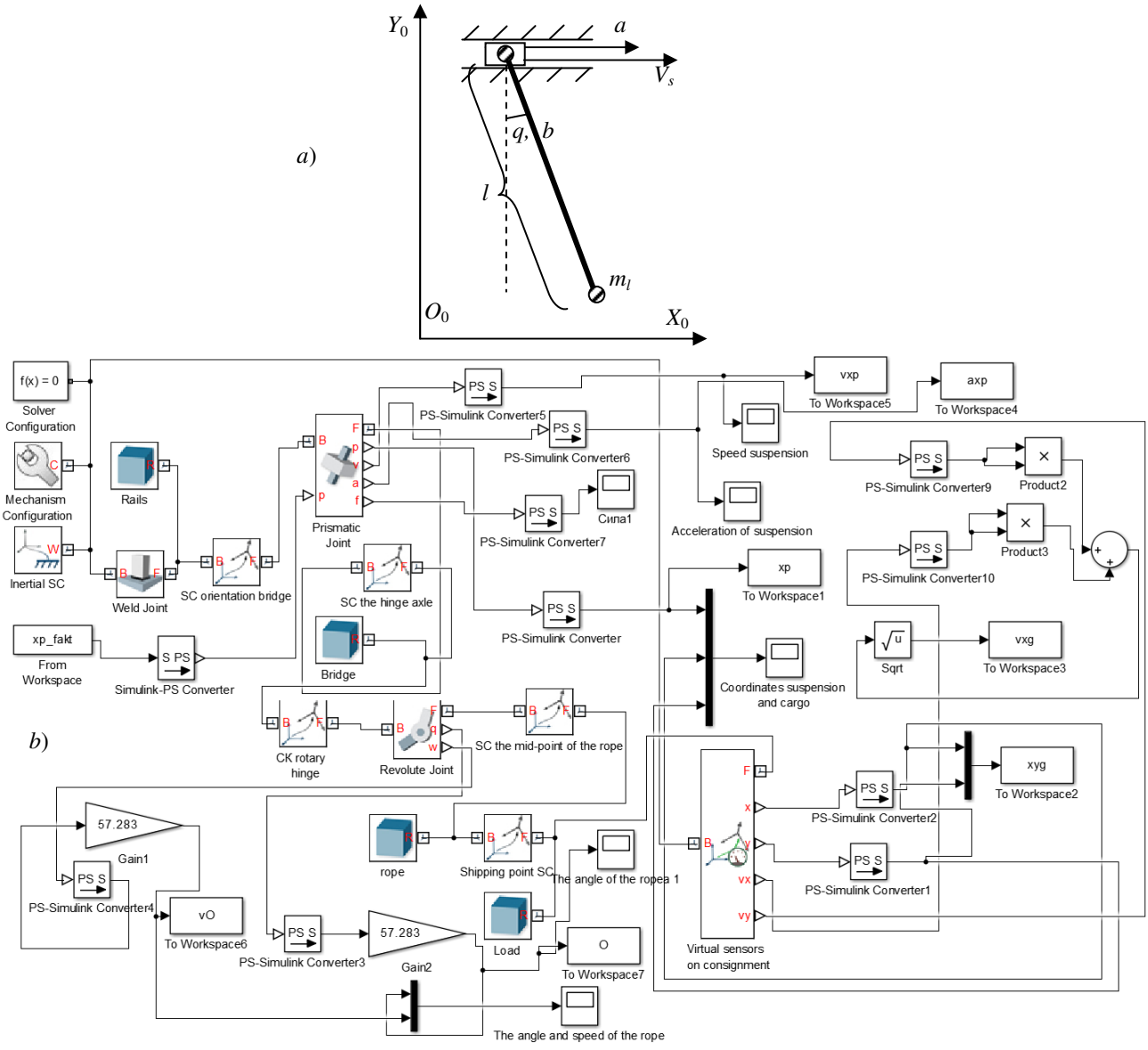

Figure 1 Settlement scheme of the OC dynamic system (a) and the corresponding simulation model in SimMechanics Second Generation and Simulink notation (b).

Given in (2) indicators are determined by means of signal processing of virtual meters in simulation model OC. We use method of adding penalty function [11, 12] to the basic function (2) to mix the problem of imputation optimization to the problem of implicit optimization whose solution we apply the simplex method:

$\Delta y=0$ at $T_{q\max}\geq T_{brak}$;

$\Delta y=k\cdot|(T_{q\max}-T_{brak})|$ at $T_{q\max}<T_{brak}$,

where $T_{q\max}$ – the nearest to the present time past time of reaching q_{max}; T_{brak} – time of braking beginning; k = 100 – empiric penalty coefficient.

3 RESULTS

The results of computational experiments on the simulation model can be presented in graphical form of relations of different parameters from each other (Figure 2).

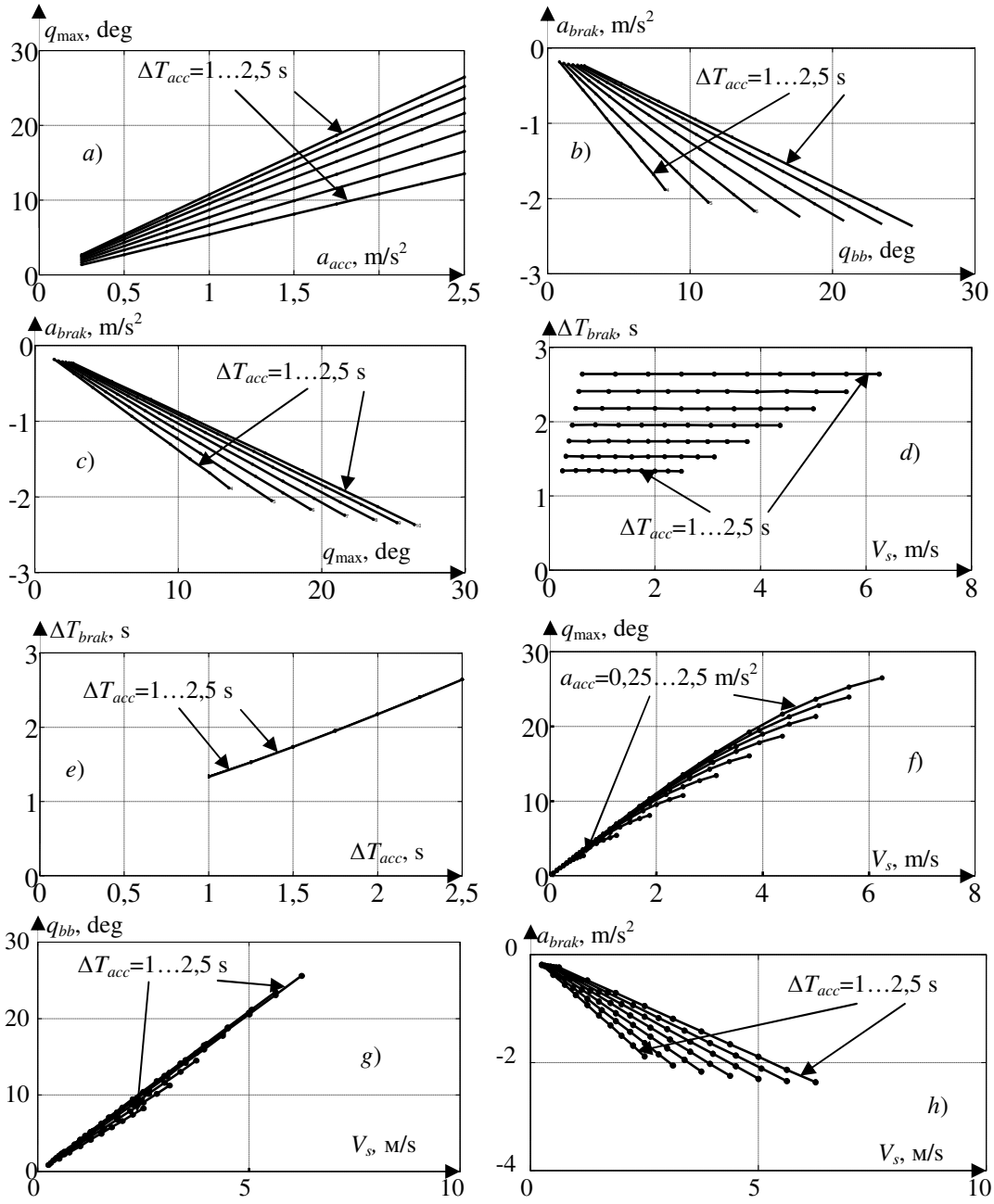

Figure 2 Obtained functional dependencies received during the computational experiments with optimization: a) $q_{\max}$ from a_{acc}; b) a_{brak} from q_{bb}; c) a_{acc} by q_{max}; d) ΔT_{brak} from V_s; d) ΔT_{brak} from ΔT_{acc}; e) $q_{\max}$ from V_s; g) q_{bb} from V_s; h) a_{brak} from V_s.

Table I - The denotations of coefficients bi (i$\in$ [1,36]) of regression equation of the deflection angle from the vertical hoist rope qbb at which it is optimal to produce the beginning of braking of point suspension load, changing Vs and qmax

Coefficient	b_1	b_2	b_3	b_4	b_5	b_6
Denotation	-0,25207	-0,51995	-2,50149	-0,35418	-0,09879	0,002282
Coefficient	b_7	b_8	b_9	b_{10}	b_{11}	b_{12}
Denotation	8,305368	22,72767	5,290067	1,984357	0,006708	-0,00157
Coefficient	b_{13}	b_{14}	b_{15}	b_{16}	b_{17}	b_{18}
Denotation	-56,0639	-21,9505	-12,8091	-0,78185	0,029136	0,000121
Coefficient	b_{19}	b_{20}	b_{21}	b_{22}	b_{23}	b_{24}
Denotation	29,69254	23,63402	6,383197	-0,08011	-0,00633	6,53E-05
Coefficient	b_{25}	b_{26}	b_{27}	b_{28}	b_{29}	b_{30}
Denotation	8,464829	-11,9735	-0,88149	0,067979	-0,00103	4,4E-06
Coefficient	b_{31}	b_{32}	b_{33}	b_{34}	b_{35}	b_{36}
Denotation	-9,25646	3,478413	-0,18614	0,00331	-2,1E-05	2,07E-08

Table II - The denotations of coefficients b_i ($i\in[1, 36]$) of the regression equation of duration of braking ΔT_{brak}, changing V_s and q_{max}

Coefficient	b_1	b_2	b_3	b_4	b_5	b_6
Denotations	0,705817	-4,70412	-0,17287	-0,20991	-0,02189	0,00133
Coefficient	b_7	b_8	b_9	b_{10}	b_{11}	b_{12}
Denotations	31,05741	7,592292	1,719708	0,75559	-0,02932	-0,00028
Coefficient	b_{13}	b_{14}	b_{15}	b_{16}	b_{17}	b_{18}
Denotations	-53,3078	-2,40926	-5,97321	-0,02038	0,014598	-0,00011
Coefficient	b_{19}	b_{20}	b_{21}	b_{22}	b_{23}	b_{24}
Denotations	23,11647	9,422257	2,162298	-0,11461	-0,00058	2,92E-05
Coefficient	b_{25}	b_{26}	b_{27}	b_{28}	b_{29}	b_{30}
Denotations	-2,15499	-4,46324	-0,16366	0,028677	-0,00065	3,66E-06
Coefficient	b_{31}	b_{32}	b_{33}	b_{34}	b_{35}	b_{36}
Denotations	-2,43068	1,172566	-0,07864	0,001549	-4,7E-06	-7,5E-08

Table III - The denotations of coefficients b_i ($i\in[1, 36]$) of the regression equation of braking acceleration a_{brak}, changing V_s and q_{max}

Coefficient	b_1	b_2	b_3	b_4	b_5	b_6
Denotations	-0,0629	-0,24769	-0,4082	-0,16261	-0,03813	-0,00018
Coefficient	b_7	b_8	b_9	b_{10}	b_{11}	b_{12}
Denotations	1,13742	3,488527	2,084317	0,750042	0,027261	-0,00049
Coefficient	b_{13}	b_{14}	b_{15}	b_{16}	b_{17}	b_{18}
Denotations	-8,51162	-7,4824	-4,70546	-0,48964	0,006204	0,000105
Coefficient	b_{19}	b_{20}	b_{21}	b_{22}	b_{23}	b_{24}
Denotations	7,674561	8,548148	2,949286	0,021757	-0,00316	2,41E-05
Coefficient	b_{25}	b_{26}	b_{27}	b_{28}	b_{29}	b_{30}
Denotations	3,078755	-4,87594	-0,51471	0,027577	-0,00035	1,35E-06
Coefficient	b_{31}	b_{32}	b_{33}	b_{34}	b_{35}	b_{36}
Denotations	-3,57426	1,487305	-0,06915	0,001098	-6,6E-06	6,89E-09

Table IV - The denotations of indicators of the the regression (3) of the angle of load rope deviation from the vertical q_{bb} when it is optimal to produce braking beginning of the load suspension point from parameters V_s and q_{max}

Indicator	Denotation
Coefficient of determination R^2	0,999999
Corrected coefficient of determination $\overline{R}^2$	0,999998
Fisher criterion *F*	1106150
Sum of squared residuals *RSS*	0,00237
Standard error of the regression equation *SEE*	0,00835
Maximum relative inaccuracy of approximation δ_{max}, %	0,063

Table V - The denotations of the quality of the regression (3) of the braking duration ΔT_{brak} from parameters V_s and q_{max}

Indicator	Denotation
Coefficient of determination R^2	0,999843
Corrected coefficient of determination $\overline{R}^2$	0,999682
Fisher criterion *F*	6205
Sum of squared residuals *RSS*	0,002
Standard error of the regression equation *SEE*	0,00782
Maximum relative inaccuracy of approximation δ_{max}, %	0,77

Table VI - The denotations of indicators of the regression (3) of accelerating braking a_{brak} from parameters V_s and q_{max}

Indicator	Denotation
Coefficient of determination	0,999987
Corrected coefficient of determination $\overline{R}^2$	0,999975
Fisher criterion *F*	79243
Sum of squared residuals *RSS*	0,000349
Standard error of the regression equation *SEE*	0,0032
Maximum relative inaccuracy of approximation δ_{max}, %	0,26

Analysis of the results allow us to hypothesize that the optimal parameters of braking (q_{bb}, ΔT_{brak}, a_{brak}) depend only on two parameters characterizing the process of motion of a dynamic system OC before braking: on constant velocity of point suspension load motion V_s before braking and on the maximum deviation of the hoist rope OC from vertical prior to the time of braking q_{max}. This hypothesis was confirmed experimentally in imitation model. By the results of computational experiments (using the Levenberg-Markvardt algoritm [13-15]) authors obtained regression dependences of the braking parameters (q_{bb}, ΔT_{brak}, a_{brak}) by V_s and q_{max}, representing symmetric polynomials from two variables predictors V_s and q_{max} in degrees [0; 1; 2; 3; 4; 5] in all possible combinations of degrees of the argument:

$$q_{bb},\ \Delta T_{brak},\ a_{brak} = b_1 \cdot v_{\Pi}^5 \cdot q_{max}^5 + b_2 \cdot v_{\Pi}^5 \cdot q_{max}^4 + b_3 \cdot v_{\Pi}^5 \cdot q_{max}^3 + b_4 \cdot v_{\Pi}^5 \cdot q_{max}^2 + b_5 \cdot v_{\Pi}^5 \cdot q_{max} + b_6 \cdot v_{\Pi}^5 + b_7 \cdot v_{\Pi}^4 \cdot q_{max}^5 + b_8 \cdot v_{\Pi}^4 \cdot q_{max}^4 + b_9 \cdot v_{\Pi}^4 \cdot q_{max}^3 + b_{10} \cdot v_{\Pi}^4 \cdot q_{max}^2 + b_{11} \cdot v_{\Pi}^4 \cdot q_{max} + b_{12} \cdot v_{\Pi}^4 + b_{13} \cdot v_{\Pi}^3 \cdot q_{max}^5 + b_{14} \cdot v_{\Pi}^3 \cdot q_{max}^4 + b_{15} \cdot v_{\Pi}^3 \cdot q_{max}^3 + b_{16} \cdot v_{\Pi}^3 \cdot q_{max}^2 + b_{17} \cdot v_{\Pi}^3 \cdot q_{max} + b_{18} \cdot v_{\Pi}^3 + b_{19} \cdot v_{\Pi}^2 \cdot q_{max}^5 + b_{20} \cdot v_{\Pi}^2 \cdot q_{max}^4 + b_{21} \cdot v_{\Pi}^2 \cdot q_{max}^3 + b_{22} \cdot v_{\Pi}^2 \cdot q_{max}^2 + b_{23} \cdot v_{\Pi}^2 \cdot q_{max} + b_{24} \cdot v_{\Pi}^2 + b_{25} \cdot v_{\Pi} \cdot q_{max}^5 + b_{26} \cdot v_{\Pi} \cdot q_{max}^4 + b_{27} \cdot v_{\Pi} \cdot q_{max}^3 + b_{28} \cdot v_{\Pi} \cdot q_{max}^2 + b_{29} \cdot v_{\Pi} \cdot q_{max} + b_{30} \cdot v_{\Pi} + b_{31} \cdot q_{max}^5 + b_{32} \cdot q_{max}^4 + b_{33} \cdot q_{max}^3 + b_{34} \cdot q_{max}^2 + b_{35} \cdot q_{max} + b_{36}. \quad (3)$$

The coefficients denotations of the regression equation (3) are shown in Table I-III.

Analysis of indicators of the quality of multiple non-linear regression equation (2) (Table IV-VI) shows us that the regression equation of this type gives the best results in terms of accuracy (minimum inaccuracy δ_{max}). All the coefficients of the regression equation are significant according to the Student's t-statistics. The maximum relative inaccuracy of approximation δ_{max} is less than 0,77 % for the duration of braking ΔT_{brak} throughout the considered range of predictors.

Testing of regression equations for damping load show their efficiency (Fig. 3). In the example shown in Fig. 3, acceleration of speed up a_{acc} and duration of speed up ΔT_{acc} are taken equal $a_{acc} = 2$ [m/s^2], $\Delta T_{acc} = 2$ [s].

Residual denotations of velocities change of the deflection angle of the rope $\dot{q}_{res}$ after braking obtained in example for solving the optimizing problem by means of simplex method and using regression equations are 0,088 and 0,108 [deg/s] correspondingly. The residual value of the linear velocity of the point of suspension after braking V_{sres}, obtained in the example for solving the optimization problem by means of simplex method and using the regression equation are 0,0197 and 0,0219 [m/s] correspondingly.

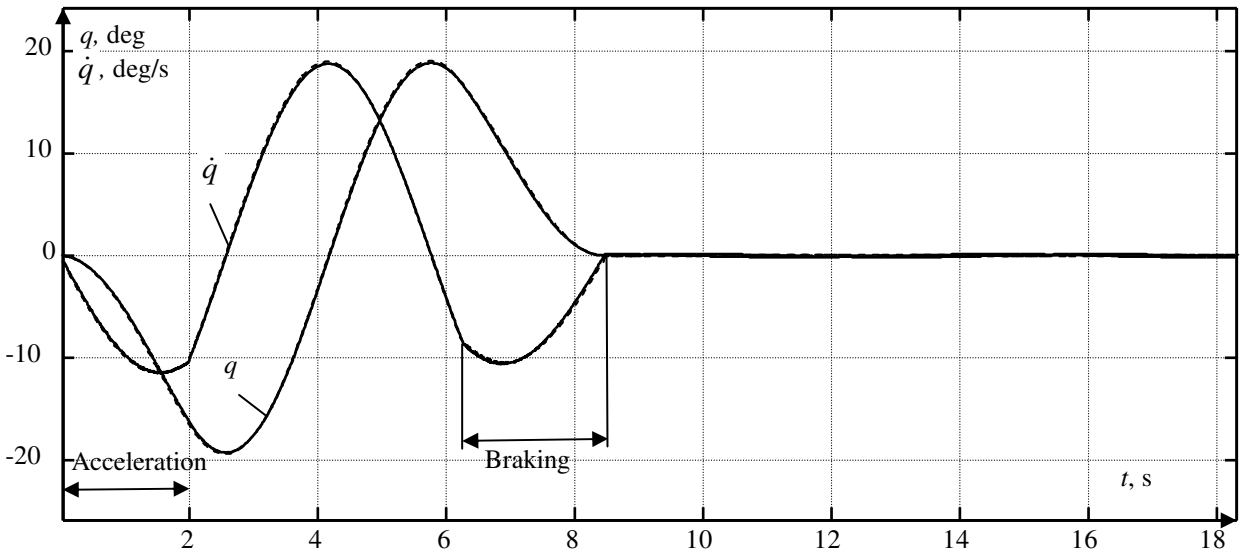

Figure 3 Examples of time dependences of the deflection angle of the hoist rope and rate of change of the deflection angle: solid line - obtained by solving the optimization problem by means of simplex method using a penalty functions; dashed line - obtained by parameters denotations (q_{bb}, ΔT_{brak}, a_{brak}), calculated by regression (3).

As a rule, load OC displacement is carried out not in the one plane (only by bridge movement and trolley movement). It is carried out in combination of two regulated movements, i.e. on space trajectory.

However, space load oscillations for small angles values (less than 5 in most cases of displacement) can be with comparatively little accuracy and be presented as superposition of displacements in two mutually perpendicular planes. I.e. worked out equations of regression can be used for residual load pendulum oscillations damping by its space displacement.

4 CONCLUSIONS

Using imitation model OC we get equations of regression of load pendulum oscillations, moved by overhead crane with relay drive. Application of these equations of regression gives the possibility of the synthesis of acceleration values and braking time in real-time regime. It allows to damp load pendulum oscillations on rope suspension for present (measured) angle values of load rope deviation from vertical line and movement speed of suspension point. Herewith, we do not use imitation modeling which takes a lot of time. The synthesis is carried out by regression equations. Regression models, which are analogous to presented, can be in real-time regime and can be used in the systems of automatic direction OC.

REFERENCES

[1] Shchedrin A.V., Serikov S.A., Kolmykov V.V., Automatic soothing vibrations of the bridge crane to load. *Instruments and systems. Management, monitoring, diagnostics*, No. 8, 2007, pp. 13-17.

[2] Blackburn D., Singhose W., Kitchen J., Patrangenaru V., Lawrence J., Command Shaping for Nonlinear Crane Dynamics. *Journal of Vibration and Control*, No. 16, 2010, pp. 477-501.

[3] Tolochko O.I., Bazhutin D.V., Comparative analysis of methods of damping oscillations of cargo suspended to the mechanism of translational motion of overhead crane. *Electrical machinery and electrical equipment*, No. 75, 2010, pp. 22-28.

[4] Omar H.M., *Control of gantry and tower cranes: PhD Dissertation*. Virginia Polytechnic Institute and State University, Blacksburg, Virginia, 2003.

[5] Abdel-Rahman E.M., Nayfeh A.H., Masoud Z.N., Dynamics and control of cranes: a review. *Journal of Vibration and Control*, No. 9, 2003, pp. 863-908.

[6] Y. Fang, W.E. Dixon, D.M. Dawson and E. Zergeroglu, Nonlinear coupling control laws for an underactuated overhead crane system. *IEEE / ASME Trans. Mechatronics*, No. 3, 2003, pp. 418-423.

[7] Moskalenko V.V., *Electric drive*. Academy Press, Moscow, 2007, pp. 368.

[8] Kim Y.S., A new vision-sensorless anti-sway control system for container cranes, *Industry Applications Conference*, Vol. 1, 2003, pp. 262-269.

[9] Singer N., Singhose W., Seering W., Comparison of filtering methods for reducing residual vibration. *European Journal of Control*, No. 5, 1999, pp. 208-218.

[10] Shcherbakov V., Korytov M., Sukharev R., Volf E., Mathematical modeling of process moving cargo by overhead crane. *Applied Mechanics and Materials*, Vols. 701-702, 2015, pp. 715-720.

[11] Vasiliev F.P., *Optimization Method*. Factorial Press, Moscow, 2002, pp. 824.

[12] Bundy B., *Optimization methods. Introductory course: Lane*. Radio and Communications Press, 1988.

[13] Korytov M.S., Shcherbakov V.S., Kotkin S.V., Construction of regression model of estimating the energy expenditure workflow crane. *Vestnik of VGTU*, Vol. 8, No. 3, 2012, pp. 92-95.

[14] Halafjan, A.A., *STATISTICA 6. Statistic analysis of date*. Binom-Press, Moscow, 2007, pp. 512.

[15] Seber G.A.F, Wild C.J., *Nonlinear Regression*. John Wiley and Sons, New York, 1989. Pp. 781.

ISSN 1590-8844
International Journal of Mechanics and Control, Vol. 17, No. 02, 2016

BENCHMARK OF THE ROTORDYNAMICS CAPABILITIES OF THE MOST PROMINENT FINITE ELEMENT METHOD SOFTWARE

Fabio Bruzzone Carlo Rosso

Dipartimento di Ingegneria Meccanica e Aerospaziale - Politecnico di Torino

ABSTRACT

Aim of this paper is to analyze the performance of the most important solvers for finite element method analyses with particular interest to rotordynamics. In order to benchmark their performance in their capability of modelling the effects of gyroscopic moments, the formulation of the gyroscopic damping matrix will be analyzed for both beam and solid elements. Then two reference models will be described for simple rotor geometries that include gyroscopic effects. Then the same rotor geometries will be built in the different software using both beam and solid elements. The obtained Campbell's diagrams will be compared to each other and to the reference models and the conclusions will be drawn.

Keywords: rotordynamics, FEM, software, benchmark, gyroscopic effects

1 INTRODUCTION

With the advent of always increasing computational power availability, more advanced simulation tools have been created that allow to model and simulate the most complex phenomena. One of the hardest dynamic problems to be analytically solved is that of rotors dynamics on which several forces are applied. One of the phenomena that influences more the dynamics of rotating structures is the gyroscopic effect, which causes an apparent stiffening of the body and changes the frequency evolution of the forward and backward whirling modes at the different rotational velocities. Only some of the commercial software for finite element analyses offer the capability to solve this kind of problems but their performance and the correctness of their results appears to have never been compared. Objective of this paper is hence to benchmark the results of four of the main solvers that offer rotordynamic capabilities. Those are namely: MSC Nastran, NX Nastran, Ansys and Samcef. Those software will be tested by comparing the Campbell's diagrams obtained with the models available in literature for two simple rotor geometries that include the effects of gyroscopic moments.

Contact author: Carlo Rosso[1]

[1]Corso Duca degli Abruzzi,24 - 10129 Torino, Italy.
E-mail: carlo.rosso@polito.it

This benchmarking is always performed using a numerical reference, because the goal of the activity is to compare the capabilities of the codes. For a deeper investigation, an experimental campaign has to be used as a reference.

2 SOFTWARE'S ELEMENTS FORMULATIONS FOR THE GYROSCOPIC DAMPING MATRIX

2.1 BEAM ELEMENTS

Suppose that a structure is rotating with rotational velocity $\Omega_X = \dot{\theta}_X$ around the X axis of a Cartesian (OXYZ) inertial reference frame, hence the displacements in the directions perpendicular to the spin axis are u_Y and u_Z. The corresponding rotations are θ_Y and θ_Z and the angular velocities are $\dot{\theta}_Y$ and $\dot{\theta}_Z$. If a precessional velocity is applied to an axis perpendicular to the spin axis, then a reaction moment, called Gyroscopic moment, appears around an axis that is perpendicular to both the spin and precessional velocity axes. For small rotations θ_Y and θ_Z then the instantaneous angular velocity vector is [1]

$$\{\Omega_P\} = \begin{Bmatrix} -\dot{\theta}_Z\theta_Y + \Omega_x \\ \dot{\theta}_Z \sin(\Omega_x t) + \dot{\theta}_Y \cos(\Omega_x t) \\ \dot{\theta}_Z \cos(\Omega_x t) - \dot{\theta}_Z \sin(\Omega_x t) \end{Bmatrix} \quad (1)$$

The kinetic energy of a lumped mass, obtained using (1) is hence

$$E_{Mass}^{Kin} = \frac{1}{2}\begin{Bmatrix}\dot{u}_Y\\ \dot{u}_Z\end{Bmatrix}^T \begin{bmatrix} m & 0\\ 0 & m\end{bmatrix}\begin{Bmatrix}\dot{u}_Y\\ \dot{u}_Z\end{Bmatrix} + \frac{1}{2}\begin{Bmatrix}\dot{\theta}_Y\\ \dot{\theta}_Z\end{Bmatrix}^T \begin{bmatrix} I_d & 0\\ 0 & I_d\end{bmatrix}\begin{Bmatrix}\dot{\theta}_Y\\ \dot{\theta}_Z\end{Bmatrix} - \Omega_X I_p \dot{\theta}_Z \theta_Y \quad (2)$$

where E_{Mass}^{Kin} is its total kinetic energy, m its mass, I_p and I_d are respectively its polar and diametral inertia. The first two terms of (2) contribute to the mass matrix of the elements, while the last to the gyroscopic one. Beam elements are considered as an infinite series of lumped masses, and so the gyroscopic kinetic energy is obtained integrating this term, obtaining

$$E_{Beam}^{Gyro,Kin} = -2\rho\Omega_X I_X \int_0^L \dot{\theta}_Z \theta_Y \, dX \quad (3)$$

where ρ is the material density, I_X is the moment of inertial normal to X and L is the length of the beam element. By using the shape functions [N] for beam elements the gyroscopic damping matrix is obtained. This formulation is shared by all software analyzed.

2.2 SOLID ELEMENTS

The formulation of the gyroscopic damping matrix is instead different among the software and will be dealt separately. MSC Nastran does not have the capability to solve solid rotordynamic analyses and therefore its formulation will not be shown.

2.2.1 NX Nastran

In this software the gyroscopic term is calculated only for the nodes that have rotational degrees of freedom, which is not the case of solid elements. Hence a "surface coat" of shell elements has to be applied on the surface of the solid model. For the nodes created in this way the gyroscopic matrix is calculated as [2]

$$C = \begin{bmatrix} 0 & 0 & 0 & 0 & 0 & 0 & 0 & 0\\ 0 & 0 & 0 & 0 & 0 & 0 & 0 & 0\\ 0 & 0 & 0 & 0 & 0 & 0 & 0 & 0\\ 0 & 0 & 0 & 0 & 0 & 0 & 0 & 0\\ 0 & 0 & 0 & 0 & 0 & \theta_z & 0 & 0\\ 0 & 0 & 0 & 0 & \theta_z & 0 & 0 & 0\\ 0 & 0 & 0 & 0 & 0 & 0 & 0 & 0\\ 0 & 0 & 0 & 0 & 0 & 0 & 0 & 0 \end{bmatrix} \quad (4)$$

where the term θ_z is the Steiner's term of inertia, calculated as

$$\theta_z = \sum m(dx^2 + dy^2) \quad (5)$$

2.2.2 ANSYS and SAMCEF

These two software share the same formulation of the gyroscopic matrix for solid elements, and its derivation is similar to the one for beam elements, and indeed, using the same notation as paragraph 2.1, the kinetic gyroscopic energy is [3] [4] [5]

$$E_{Solid}^{Gyro,Kin} = -\Omega_x \int_{V_i} x\left(\dot{\theta}_Z y + \ddot{\theta}_Y z\right) dm \quad (6)$$

where in this case V_i is the volume of the ith element. Again, from the kinetic energy, the gyroscopic damping matrix for each element is calculated using the appropriate shape functions [N] for the different kind of solid elements.

3 REFERENCE MODELS

To benchmark the performance of the different software two very well known rotor geometries will be analyzed: the first one is the Stodola/Green rotor, while the second will be the mid-span rotor, often called Jeffcott rotor.

3.1 STODOLA/GREEN ROTOR REFERENCE MODEL

Consider the rotor geometry shown in Figure 1 rotating around the Z axis. The flexible but mass-less shaft has a length S, diameter d and the free end is clamped, so the displacements in any direction, translational or torsional, are denied at this end.

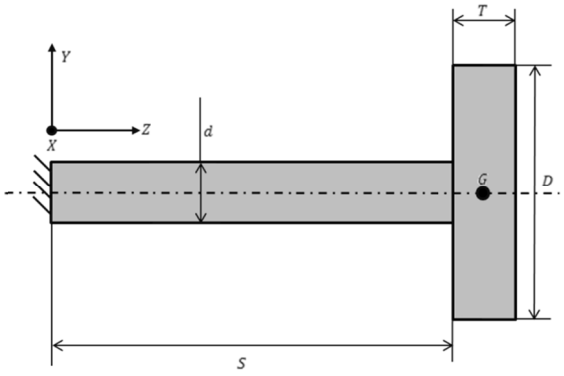

Figure 1 Stodola\Green rotor geometry.

The rigid disk of diameter D, thickness T and total mass m is placed on the other end of the shaft and it is not constrained in any way. The inertia of the shaft and the polar and transverse moments of inertia of the disk can be defined respectively as [6] [7]

$$I = \frac{\pi d^4}{64} \quad (7)$$

$$J_p = \frac{mD^2}{8} \quad (8)$$

$$J_t = \frac{mD^2}{16} \quad (9)$$

The rotor center of mass G will experience the displacements and rotations as depicted in Figure 2, and hence applying Newton's laws and considering that the rotations are small ($\vartheta \approx 0$) the following equations of motion are obtained

$$\begin{cases} m\ddot{x}_G + k_{11}x_G + k_{21}\vartheta_{y,G} = 0 \\ m\ddot{y}_G + k_{11}y_G + k_{12}\vartheta_{x,G} = 0 \\ J_t\ddot{\vartheta}_{x,G} + J_P\Omega\dot{\vartheta}_{y,G} + k_{12}y_G + k_{22}\vartheta_{x,G} = 0 \\ J_t\ddot{\vartheta}_{y,G} - J_P\Omega\dot{\vartheta}_{x,G} + k_{21}x_G + k_{22}\vartheta_{y,G} = 0 \end{cases} \quad (10)$$

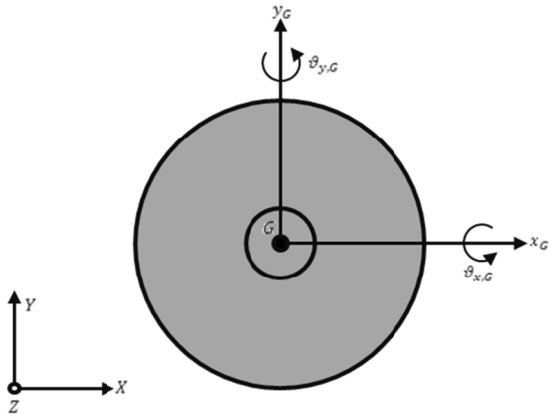

Figure 2 Displacements and rotations experienced by the center of mass G of the disk.

Organizing these equations according to the following vector

$$\{u\} = \begin{Bmatrix} x_G \\ y_G \\ \vartheta_{x,G} \\ \vartheta_{y,G} \end{Bmatrix} \quad (11)$$

and calling $\{\dot{u}\}$ and $\{\ddot{u}\}$ its first and second derivative, the following dynamic system is obtained

$$[M]\{\ddot{u}\} + \Omega[G]\{\dot{u}\} + [K]\{u\} = 0 \quad (12)$$

The stiffness parameters of the shaft are

$$k_{11} = \frac{12EI}{L^3} \quad (13)$$

$$k_{12} = \frac{6EI}{L^2} = -k_{21} \quad (14)$$

$$k_{22} = \frac{4EI}{L} \quad (15)$$

where L is the length of the shaft and E is the Young's modulus of the material. The mass, damping and stiffness matrices obtained are respectively.

$$[M] = \begin{bmatrix} m & 0 & 0 & 0 \\ 0 & m & 0 & 0 \\ 0 & 0 & J_t & 0 \\ 0 & 0 & 0 & J_t \end{bmatrix} \quad (16)$$

$$[\mathrm{G}] = \begin{bmatrix} 0 & 0 & 0 & 0 \\ 0 & 0 & 0 & 0 \\ 0 & 0 & 0 & \mathrm{J_P} \\ 0 & 0 & -\mathrm{J_p} & 0 \end{bmatrix} \quad (17)$$

$$[\mathrm{K}] = \begin{bmatrix} \mathrm{k_{11}} & 0 & 0 & \mathrm{k_{21}} \\ 0 & \mathrm{k_{11}} & \mathrm{k_{12}} & 0 \\ 0 & \mathrm{k_{12}} & \mathrm{k_{22}} & 0 \\ \mathrm{k_{21}} & 0 & 0 & \mathrm{k_{22}} \end{bmatrix} \quad (18)$$

A Matlab code has been developed for computing the results of that model.

3.2 MID-SPAN ROTOR REFERENCE MODEL

Consider now a rotor as shown in Figure 3. The rigid disk of diameter D, thickness T and total mass m is placed at the midpoint of the shaft of total length S and diameter d, so that each portion has length $L = S/2 - T/2$ and both ends are clamped. Proceeding in the same way as in the previous paragraph the same displacement vector (11) and dynamic system (12) are obtained [7] [8], but in this case the matrices are

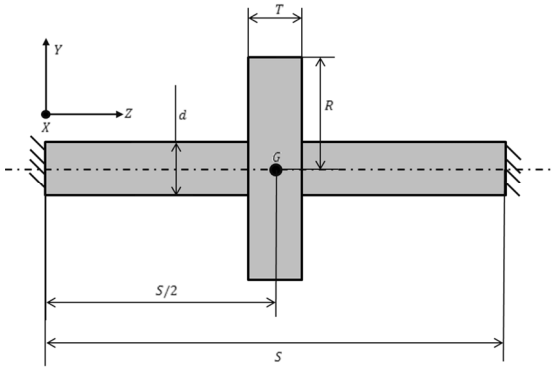

Figure 3 Mid-span rotor geometry.

$$M = \begin{bmatrix} m & 0 & 0 & 0 \\ 0 & m & 0 & 0 \\ 0 & 0 & J_t & 0 \\ 0 & 0 & 0 & J_t \end{bmatrix} \quad (19)$$

$$G = \begin{bmatrix} 0 & 0 & 0 & 0 \\ 0 & 0 & 0 & 0 \\ 0 & 0 & 0 & J_P \\ 0 & 0 & -J_p & 0 \end{bmatrix} \quad (20)$$

$$K = \begin{bmatrix} \alpha & 0 & 0 & 0 \\ 0 & \alpha & 0 & 0 \\ 0 & 0 & \delta & 0 \\ 0 & 0 & 0 & \delta \end{bmatrix} \quad (21)$$

where in this case the inertial properties of the disk are

$$J_p = \frac{mR^2}{2} \quad (22)$$

$$J_t = \frac{m}{4}\left(R^2 + \frac{1}{3}T^2\right) \quad (23)$$

and the stiffness parameters are

$$\alpha = 2 \cdot k \tag{24}$$

$$\delta = k \cdot \left({}^{S}/_{2}\right)^{2} \tag{25}$$

$$k = \frac{48\,EI}{L^3} \tag{26}$$

Solving this system for different rotational velocities Ω the Campbell diagram for the cylindrical (bending) and 1D modes will be plotted, but to obtain more precise results a more accurate approach will also be used for this model. The rotor geometry has been discretized using 61 nodes, forming 60 beam elements according to Timoshenko's beam theory. Each node has four degrees of freedom organized as [9]

$$u_{Node} = \begin{Bmatrix} x \\ y \\ \vartheta_x \\ \vartheta_y \end{Bmatrix} \tag{27}$$

so that for each element the displacement vector is

$$u_{Element} = \{x_1\ x_2\ y_1\ y_2\ \vartheta_{x1}\ \vartheta_{x2}\ \vartheta_{y1}\ \vartheta_{y2}\}^T \tag{28}$$

where the subscripts 1 and 2 indicate the first and second node of each element. The mass matrix is defined as the sum of the translational and rotational contributions so that

$$[M] = [M_t] + [M_r] \tag{29}$$

where

$$M_t = \frac{\rho AL}{420(1+\varphi)^2} \cdot \begin{bmatrix} m_1 & 0 & 0 & m_2 & m_3 & 0 & 0 & -m_4 \\ & m_1 & m_2 & 0 & 0 & m_3 & -m_4 & 0 \\ & & m_5 & 0 & 0 & m_4 & -m_6 & 0 \\ & & & m_5 & m_4 & 0 & 0 & -m_6 \\ & & & & m_1 & 0 & 0 & -m_2 \\ & & & & & m_1 & -m_2 & 0 \\ & & & & & & m_5 & 0 \\ & & & & & & & m_5 \end{bmatrix} \tag{30}$$

$$M_r = \frac{\rho I}{30L \cdot (1+\varphi)^2} \cdot \begin{bmatrix} m_7 & 0 & 0 & m_8 & -m_7 & 0 & 0 & m_8 \\ & m_7 & m_8 & 0 & 0 & -m_7 & m_8 & 0 \\ & & m_9 & 0 & 0 & -m_8 & -m_{10} & 0 \\ & & & m_9 & -m_8 & 0 & 0 & -m_{10} \\ & & & & m_7 & 0 & 0 & -m_8 \\ & & & & & m_7 & -m_8 & 0 \\ & & & & & & m_9 & 0 \\ & & & & & & & m_9 \end{bmatrix} \tag{31}$$

The stiffness matrix is

$$K = \frac{EI}{L^3(1+\varphi)} \cdot \begin{bmatrix} k_1 & 0 & 0 & k_2 & -k_1 & 0 & 0 & k_1 \\ & k_1 & k_2 & 0 & 0 & -k_1 & k_2 & 0 \\ & & k_3 & 0 & 0 & -k_2 & k_4 & 0 \\ & & & k_3 & -k_2 & 0 & 0 & k_4 \\ & & & & k_1 & 0 & 0 & -k_2 \\ & & & & & k_1 & -k_2 & 0 \\ & & & & & & k_3 & 0 \\ & & & & & & & k_3 \end{bmatrix} \tag{32}$$

and the gyroscopic one is simply

$$[G] = 2[M_r] \tag{33}$$

All the coefficients employed in those matrices are listed in Appendix A. As it is evident those matrices are symmetric, especially the gyroscopic one which is instead usually skew-symmetric. Indeed the dynamic system has to be assembled before the solution can proceed, obtaining the following system

$$\begin{bmatrix} [M] & [0] \\ [0] & [M] \end{bmatrix} \{\ddot{u}\} + \Omega \begin{bmatrix} [0] & [G] \\ -[G] & [0] \end{bmatrix} \{\dot{u}\} + \begin{bmatrix} [K] & [0] \\ [0] & [K] \end{bmatrix} \{u\} = \{0\} \tag{34}$$

To model the shaft's clamped ends, the rows and columns corresponding to the first and last nodes of the rotor are deleted: this simulates the eliminations of the degrees of freedom of those two nodes, because with a clamped constraint no displacement or rotation is possible.

3.3 IMPLEMENTATION OF THE REFERENCE MODELS

In order to obtain accurate results, all the previous matrices are used in a tailored Matlab code and considering a high number of degree of freedom. The final problem dimension for the mid-span rotor problem is 472x472. For the same reasons, this approach has also been applied to the Stodola/Green rotor discretizing the geometry using 53 nodes forming 52 beam elements. The final problem dimension is 424x424.

4 BEAM MODELS AND SOFTWARE'S RESULTS

In this paragraph the results obtained from the software for the two rotor cases will be compared. The geometrical, material and FEM model properties are the same for each program and are listed in Table 1 for the Stodola/Green rotor and in Table 2 for the mid-span rotor. The same steel properties will be used throughout this paper and hence will be shown only once. The obtained Campbell's diagrams are compared in Figure 4 and 5 respectively for the Stodola/Green and mid-span rotor with those obtained from the models shown in paragraph 3.1 and 3.2.

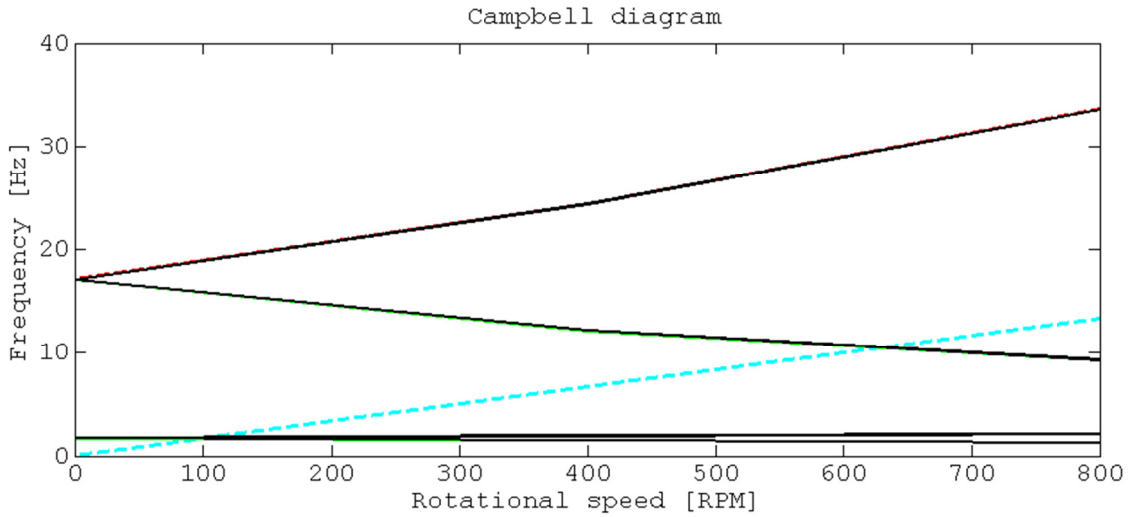

Figure 4 Stodola\Green beam rotor models Campbell's diagrams comparison.

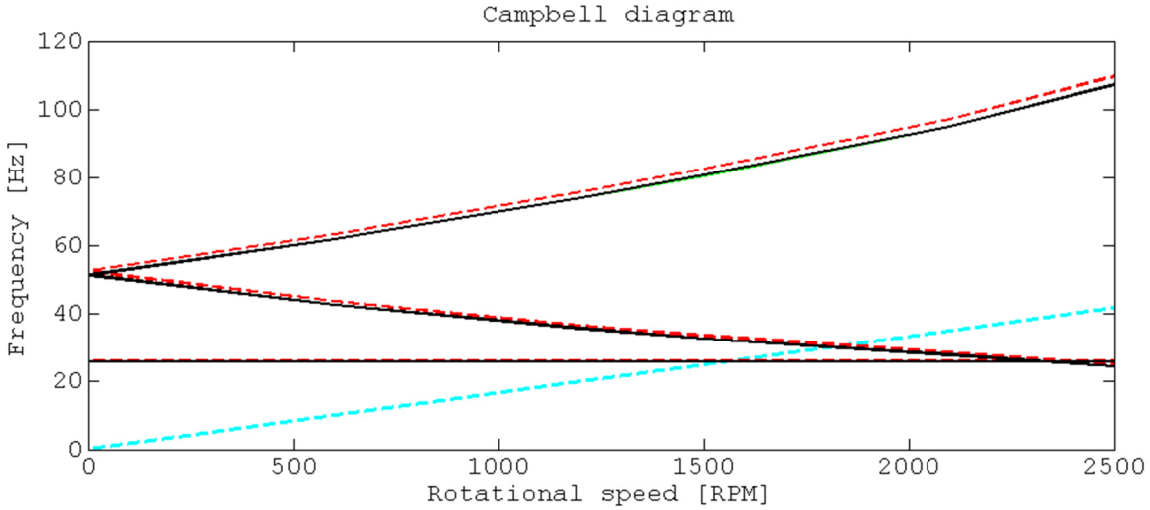

Figure 5 Mid-span beam rotor models Campbell's diagrams comparison.

Table 1: Stodola\Green beam rotor properties

FEM Beam Model	
N° of Nodes	53
N° of Elements	52
Constraint	Clamped end
Ω Range	0÷800 RPM
Material (Steel)	
E	210 GPa
ν	0.3
ρ	7850 kg/m3
Geometrical Properties	
Shaft Diameter	0.05 m
Shaft Length	1.2 m
Disk Diameter	0.6 m
Disk Thickness	0.05 m

Table 2: Mid-span beam rotor properties

FEM Beam Model	
N° of Nodes	61
N° of Elements	60
Constraints	Clamped ends
Ω Range	0÷2500 RPM
Geometrical Properties	
Shaft Diameter	0.04 m
Shaft Length (each)	0.58
Disk Diameter	0.7 m
Disk Thickness	0.04 m

The red dashed lines in those figures represents the results obtained from reference models, the solid black lines are the results from Ansys, the blue ones the results from Samcef, while the green ones are the results from NX Nastran. The cyan dashed line indicates the condition $\Omega = \omega$. The results from MSC Nastran are not shown in those plots because this software only outputs the natural frequencies for the different modes and the rotor energies, but not the evolution of the frequencies at the different rotational speeds.
In the following Table 3 and Table 4, the average relative errors for the bending and 1D modes for the Stodola/Green rotor and for the cylindrical and 1D modes for the mid-span rotor are respectively listed. The average relative error has been calculated as

$$\bar{e} = \frac{\sum_{i=1}^{N} \left(\frac{SOFTWARE_i}{ANALYTICAL_i} - 1 \right) \cdot 100}{N} \tag{35}$$

where N is the number of rotational speeds for which the problem has been solved and i=1,...,N. For MSC Nastran, since the only available frequency is that at 0 RPM the relative error is calculated only for $i = 1$.

Table 3: Stodola\Green beam rotor average relative errors

Bending mode	
MSC Nastran	1.86%
NX Nastran	1.88%
Samcef	1.81%
Ansys	1.81%
1D mode	
MSC Nastran	2.35%
NX Nastran	2.45%
Samcef	2.33%
Ansys	2.31%

Table 4: Mid-span beam rotor average relative errors

Cylindrical mode	
MSC Nastran	1.71%
NX Nastran	2.69%
Samcef	1.18%
Ansys	1.33%
1D mode	
MSC Nastran	1.48%
NX Nastran	1.97%
Samcef	1.08%
Ansys	1.07%

5 SOLID MODELS AND SOFTWARE'S RESULTS

The same geometrical and material properties listed in Table 1 and Table 2 have been used for the solid models for both rotors. 10 nodes tetrahedral solid elements with a mesh size of 2mm has been used in each software for both models, generating 19727 and 21085 elements for the Stodola/Green and mid-span rotor respectively. MSC Nastran has been excluded from this comparison since it is not capable of solving 3D problems [10]. In NX Nastran an additional surface coat of 6 nodes triangular shell elements has been applied for the reasons stated in paragraph 2.2.1. The comparisons of the Campbell's diagrams obtained are shown in Figure 6 and Figure 7 while the average relative errors, calculated again with (35) can be seen in Table 5 and Table 6. The same line colours of Figures 4 and 5 are applied here. The obtained mode shapes from Ansys for the various modes here analyzed can be seen in Figure 8 and Figure 9. As it is evident the errors are larger than for the beam models, which is expected, because the lumped parameters model and the beam formulations are only approximations of the real behavior of the rotors. In the solid models indeed the flexibility of the disks is taken into account. Regarding NX Nastran it is now evident that the approximation in the formulation apparently has negative effects on the prediction of the gyroscopic moment influence, because the evolution of the frequencies as the rotational velocity increases are completely different from the values obtained by the 1D beam model.

Table 5:Stodola\Green solid rotor average relative errors

Bending mode	
NX Nastran	7.82%
Samcef	2.34%
Ansys	2.34%
1D mode	
NX Nastran	47.35%
Samcef	3.71%
Ansys	3.22%

Table 6: Mid-span solid rotor average relative errors

Cylindrical mode	
NX Nastran	4.06%
Samcef	1.86%
Ansys	1.93%
1D mode	
NX Nastran	58.26%
Samcef	4.03%
Ansys	3.59%

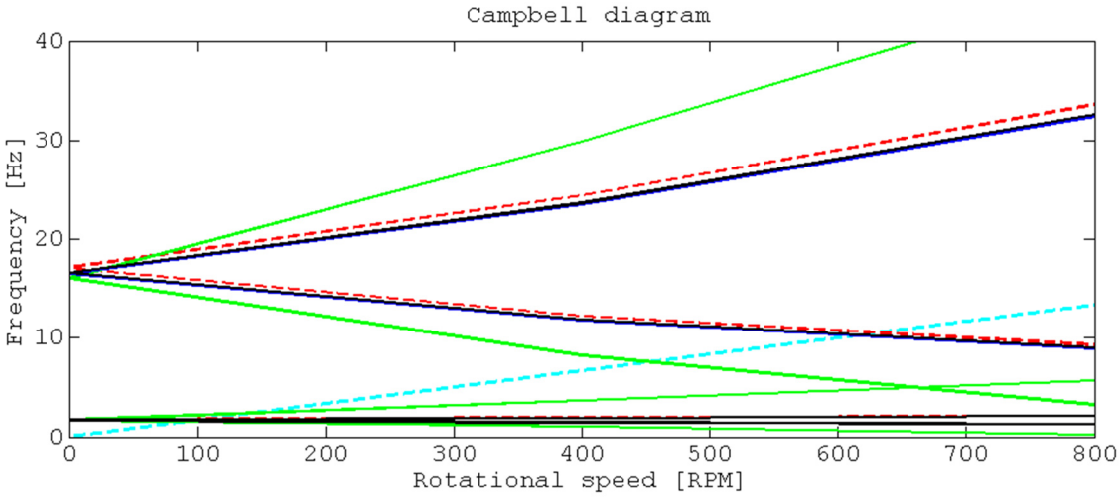

Figure 6 Stodola\Green solid rotor models Campbell's diagrams comparison.

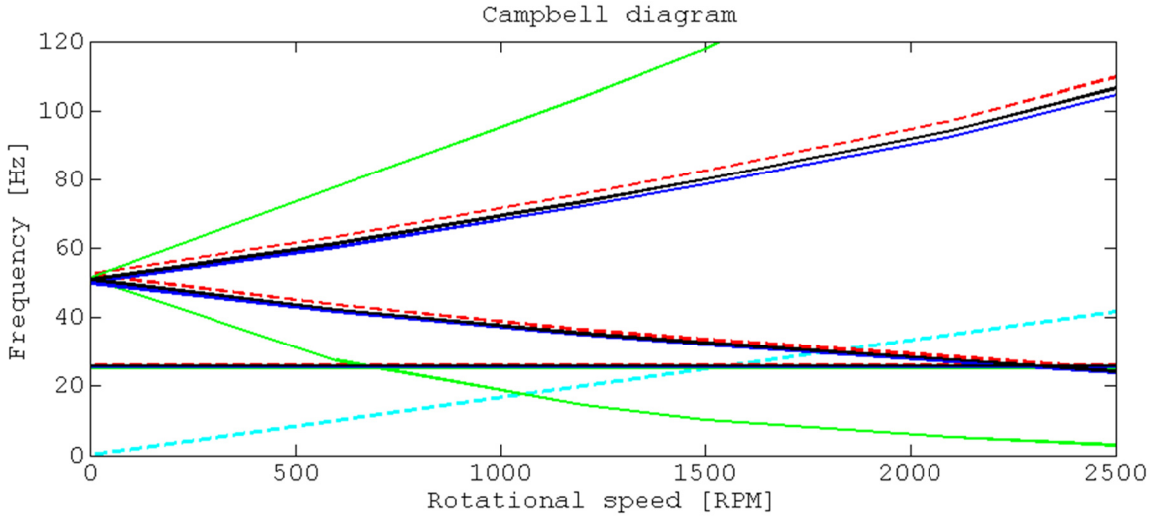

Figure 7 Mid-span solid rotor models Campbell's diagrams comparison.

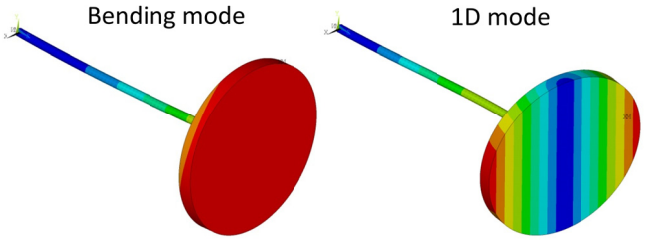

Figure 8 Stodola\Green solid rotor mode shapes obtained from Ansys.

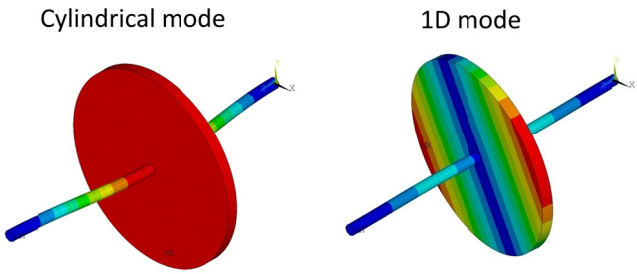

Figure 9 Mid-span solid rotor mode shapes obtained from Ansys.

6 BENCHMARK CONCLUSIONS

Now that the results for all the different beam and solid models from the different software have been compared, it is possible to draw the conclusions. MSC Nastran is not capable of performing any kind of 3D solid rotor dynamic analysis and also the results for this kind of analysis are not complete and clear even for beam models. NX Nastran in theory has those capabilities, but evidently only the beam elements formulation is complete, while the one for solid elements seems to be very approximated, since the results show large discrepancies with the 1D beam model predictions. There is not a real gyroscopic moments formulation, but the software considers only the additional inertia of the shell elements placed on the surface of the model. The results for the beam models are comparable with the other software, but not at all for the solid ones. The last two remaining software, Samcef and Ansys, yield almost the same results in any of the model described before and those are very close to the equivalent 1D beam model, which is widely used and generally accepted as correct. Although both could be hence used in this kind of analyses, Ansys presents an additional feature with respect to Samcef. This is mainly because in Samcef Field many parameters, elements attributes and other aspects of the model are decided by the software and if the user wants to modify some of those values then the text input file to the solver modules are to be modified. This is a difficult task and it is time consuming also because the documentation is not so clear. In Ansys instead the user has the ability to control every aspect of the model if using the Mechanical APDL language. Using this approach it is also possible to setup one "solution script" and use it, with minimal and quick changes, to study very different models, and still be sure of obtaining correct results.

ACKNOWLEDGMENTS

The authors would like to thank the GreatLab facility of GE Avio Aero, born in partnership with Politecnico di Torino, where the analyses in this paper have been performed.

REFERENCES

[1] H.D. Nelson, J.M. McVaugh, The dynamics of rotor-bearing systems using finite elements, *ASME Journal of Manufacturing science and Engineering*, May 1976.
[2] *Siemens PLM NX Nastran User manual*.
[3] M. Geradin, N. Kill, A new approach to Finite Element modelling of flexible rotors, *Engineering Computing*, Vol. 1, 1984.
[4] *Ansys Mechanical APDL User manual*.
[5] *Siemens PLM Samcef User manual*.
[6] D. W. Childs, *Turbomachinery Rotordynamics: Phenomena, Modelling and Analysis*, Wiley&Sons, New York, 1993.
[7] G. Genta, *Dynamics of rotating systems*, Springer, Torino, 2004.
[8] S.Y. Yoon, Z. Lin, P.E. Allaire, *Control of surge in centrifugal compressors by active magnetic bearings*, Springer, New York, 2013.
[9] S. Jones, *Finite elements for the analysis of rotor-dynamic systems that include gyroscopic effects*, Brunel University, 2005.
[10] *MSC Nastran User manual*.

APPENDIX A

The coefficients used in the matrices (30), (31), (32) and (33) are defined as follows:

$$m_1 = 156 + 294\varphi + 140\varphi^2$$
$$m_2 = L(22 + 38.5\varphi + 17.5\varphi^2)$$
$$m_3 = 54 + 126\varphi + 70\varphi^2$$
$$m_4 = L(13 + 31.5\varphi + 17.5\varphi^2)$$
$$m_5 = L^2(4 + 7\varphi + 3.5\varphi^2)$$
$$m_6 = L^2(3 + 7\varphi + 3.5\varphi^2)$$
$$m_7 = 36$$
$$m_8 = L(3 - 15\varphi)$$
$$m_9 = L^2(4 + 5\varphi + 10\varphi^2)$$
$$m_{10} = L^2(1 + 5\varphi - 5\varphi^2)$$
$$k_1 = 12$$
$$k_2 = 6L$$
$$k_3 = L^2(4 + \varphi)$$
$$k_4 = L^2(2 - \varphi)$$

with

$$A = \pi r^2$$
$$\chi = \frac{7 + 6\nu}{6(1 + \nu)}$$
$$\varphi = \frac{12EI\chi}{GAL^2}$$

ISSN 1590-8844
International Journal of Mechanics and Control, Vol. 17, No. 02, 2016

A SMART ELECTROMECHANICAL ACTUATOR MONITOR FOR NEW MODEL-BASED PROGNOSTIC ALGORITHMS

Pier Carlo Berri Matteo D. L. Dalla Vedova Paolo Maggiore

Department of Mechanical and Aerospace Engineering, Politecnico di Torino

ABSTRACT

Prognostic algorithms able to identify precursors of incipient failures of primary flight command electromechanical actuators (EMAs) are beneficial for the anticipation of the incoming fault: an early and correct interpretation of the degradation pattern, in fact, can trig an early alert of the maintenance crew, who can properly schedule the servomechanism replacement. Given that very often these algorithms exploit a model-based approach (e.g. directly comparing the monitor with the real system or using it to identify the fault parameters by means of optimization processes), the design and development of appropriate monitoring models, able to combine simplicity, reduced computational effort and a satisfactory level of sensitivity and accuracy, becomes a fundamental and unavoidable step of the prognostic process. To this purpose, the authors propose a new simplified EMA Monitor Model able to accurately reproduce the dynamic response of the Reference Model in terms of position, speed and equivalent current, even with the presence of various incipient faults; its ability in reproducing the effects of several EMA faults is a good starting point for the implementation of a robust and accurate GA-based optimization, leading to a reliable and early fault isolation.

Keywords: aerospace, EMA, fault detection/identification, model-based, prognostics.

1 INTRODUCTION

Actuators are component responsible for moving or controlling a mechanism or system. They transfer power of various sources (mechanical, electrical, hydraulic, or pneumatic) into motion by means of gearings. With regard to flight commands, in the last years, actuators based on the hydraulic power have been replaced by Electromechanical Actuators (EMAs) because they offer more advantages: easier maintenance, reduced global weight, absence of hydraulic fluid that is often pollutant and inflammable. As some actuators are safety critical, in order to guarantee the system to always operate in safety conditions, it is necessary to schedule programs of maintenance and redundancy; nevertheless, even if, at present, they are the most common means to diminish the risks, in case of unpredicted and severe operative scenarios, they can be insufficient and it becomes necessary to forecast unscheduled maintenance.

Contact author: Matteo D. L. Dalla Vedova[1]

[1]Corso Duca degli Abruzzi 24 – 10129 Torino, Italy
E-mail: matteo.dallavedova@polito.it

In this context, as described in [1-2], there is a discipline called Prognosis and Health Management (PHM) that, through the monitoring of functional parameters of the system involved, tries to predict failures at an early stage and to determine the source of irregular behaviours. In case of EMAs, the PHM can be applied in a more efficient way than in the case of hydromechanical or electrohydraulic actuators, because, on electrical systems, additional sensors are not required. In fact, the application of the PHM strategies normally entails the monitoring of a set of parameters in the form of electric signals and they often use the same sensors of the control scheme and system monitors. For this purpose, according to the "More-electric-aircraft" paradigm [3] and to the "All-electric-aircraft" [4], in this paper EMAs are considered. Concepts and results reported in this paper are related to the design of a reliable and fast prognostic Fault Detection and Identification (FDI) routines focused on the diagnosis model-based approach and, in particular, on the parametric estimation task: to this purpose, the design and development of appropriate EMA monitoring models, able to combine simplicity, reduced computational effort and a satisfactory levels of sensitivity

and accuracy, becomes a fundamental and unavoidable step of the aforesaid prognostic process. To this purpose, in this paper authors propose a new simplified EMA Monitor Model (MM) able to accurately reproduce the dynamic response of the Reference Model in terms of position, speed and equivalent current, even with the presence of various incipient faults. For completeness it is however important to highlight that many different FDI strategies can be found in literature: e.g. model-based techniques centred on the direct comparison between real and monitoring system [5], on the spectral analysis of well-defined system behaviours performed by Fast Fourier Transform [6-7], on appropriate combinations of these methods [8] or on algorithms based on several architectures of Artificial Neural Network [9-13].

2 EMA REFERENCE MODEL

As previously mentioned, the goal of this research is the proposal of a new simplified numerical model able to simulate the behaviours of a real servomechanisms in order to perform an early identification of the symptoms (usually defined as failure precursors) of EMA degradations. First of all, in order to define the architecture of the MM and to evaluate the feasibility, the performances and the robustness of the aforesaid approach, a suitable simulation test bench has been developed in MATLAB/Simulink®. This numerical model, widely described in [13-14], is consistent with the EMA architecture shown in Fig. 1

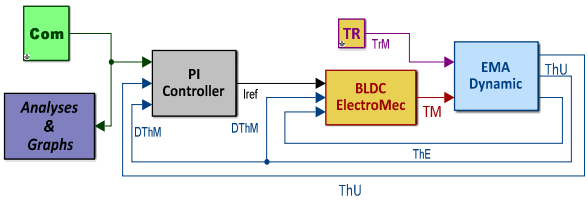

Figure 1 EMA Reference Model [13].

1. *Com*: generates input position commands.
2. *PI Controller*: simulates the actuator control electronics, closing position and speed feedback loops in and computing as output the reference current *Iref*.
3. *BLDC EM Model*: simulates the power drive electronics trough a SimScape model and the trapezoidal BLDC EM behaviour, evaluating torque as a function of three-phase current generated by an ideal H-bridge regulator.
4. *EMA Dynamic Model*: resolves the dynamic equation of mechanical behaviour by a 2 d.o.f. dynamic system.
5. *TR*: input block simulating the aerodynamic torques acting on the moving surface controlled by the actuator.
6. *Analyses & Graphs*: EMA monitoring system.

This numerical model simulates the behaviours of the real EMA taking also into account the effects of BLDC motor non-linearities [15-20], end-of-travels, compliance and backlashes acting on the mechanical transmission [21-22], ADC conversion of the feedback signals, electrical noise acting on the signal lines and electrical offset of the position transducers [5] and dry friction (e.g. acting on bearings, gears, hinges and screw actuators) [23].

3 EMA FAILURES AND DEGRADATION

Main failures in BLCD motors are due to rotor static eccentricity caused by progressive coil short-circuits or bearing wears. Short-circuits usually start between a few coils belonging to the same phase (coil-coil failure) and, then, spreading to adjacent coils. In fact, in short-circuited coils the voltage remains the same and the resistance decreases; as a consequence, a high circulating current arises and generates a localized heating in conductor that helps the propagation. Rotor static eccentricity consists in a misalignment between its rotation axis and the stator axis of symmetry: this usually occurs due to tolerances and imperfections introduced during motor construction or to gradual increase of wear of the rotor shaft bearings. Whenever it occurs, the motor, supposed to have more than one polar couple, generates a periodically variable magnetic flux, as the air gap varies during rotation as a function of the rotor angular position θ [13]. The authors, taking into account coil short-circuit and rotor static eccentricity, have studied the consequences of faults on the performances of the servomechanism [14]: their effects on the electrical features of the BLDC motor (e.g. winding resistance, inductance and back-EMF) are simulated by a simplified numerical model [24-26]. In particular, as reported in [27], authors simulated the effects of faults affecting the magnetic coupling between stator and rotor varying values and angular modulations of back-EMF coefficients. As regards the frictional effects acting on the mechanical transmission it must be noted that an increased dry friction, although does not cause the failure of the entire system, reduces the servomechanism accuracy and can influence the dynamic response of the system generating unexpected behaviour (stick-slip or limit cycles). Wear makes friction coefficients increase and reaction torque becomes higher so that the motor has to provide higher torques to actuate the control surface. Moving parts such as gears, hinges, bearings and particularly screw actuators can be affected by mechanical wear; it can generate backlashes that, acting on the elements of the mechanical transmission, reduce the EMA accuracy and can lead to stiffness and controllability problems [23].

4 EMA MONITOR MODEL

The EMA Reference Model reproduces the actual system dynamic response with the highest possible accuracy; however, its computational cost is not compatible with an iterative optimization method such as a Genetic Algorithm (GA). Then, a Monitor Model (MM) has been developed as a simplified representation of the considered EMA, yet detailed enough to simulate the effect of all the considered faults. In fact, during the optimization, the MM is executed several thousand times iteratively varying the fault parameters, until the MM response features a satisfying matching to the Reference response, which is used in place of the actual system for testing the FDI algorithm, and the quadratic error function, which compares the current signals of the two models, is minimized.

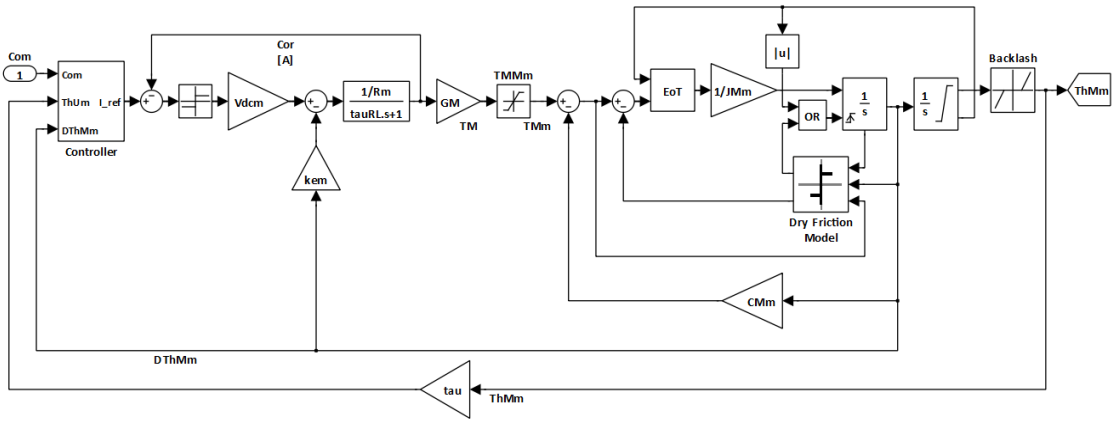

Figure 2 Simulink scheme of the Monitor Model (MM).

To achieve a good accuracy in fault isolation, the MM needs to reproduce the effect of faults with high accuracy: this way, when the same fault parameters are set to both the models, the error function returns a value near to zero, thus producing a well-defined global minimum which can be effectively detected by the genetic algorithm. Then, this paper focuses on the definition of the Monitor Model and in particular on the implementation of the BLDC electrical faults.The main simplification of the MM is the elimination of the three-phase trapezoidal control of the BLDC, replaced by a much simpler and computationally lighter single-phase equivalent scheme, which avoids the complex PWM current regulation an digital-to-analog conversion of signals (as shown in Fig. 2). This solution allows a much longer time step to be employed for the simulation, greatly reducing computing time; however, a complication arises for the simulation of electrical faults, which will be discussed in the following paragraphs.

4.1 MONITOR MODEL FAULT IMPLEMENTATION

The EMA mechanical branch is modelled with a nonlinear second order mechanical system, simulating effects of dry friction and backlash; then, the implementation of mechanical faults is quite straightforward and similar to that employed for the Reference Model. In fact, the Dry Friction fault is simulated by varying both the static and dynamic friction coefficient in the subsystem implementing the *Borello Friction Model* [23] (Fig. 2); in a similar way, the mechanical play is simulated modifying the dead band amplitude in the *Backlash* block from the Simulink libraries. Conversely, the electrical faults in the Reference Model are strictly related to the three-phase electromagnetic subsystem, not implemented in the Monitor. Reproduction of these damages thus requires a different approach. The short circuit fault is, as a first attempt, modelled with an averaged approach varying the electromagnetic parameters of the single-phase monitor electrical branch; as a first approximation, it is possible to define an equivalent N_{equiv}, which is valid for small fault entities, as:

$$N_{equiv} = \frac{N_A + N_B + N_C}{3} \tag{1}$$

where N_A, N_B and N_C are the fractions of working windings of each electrical phase. Then, the electrical parameters of the simplified model are corrected as reported below:

$$\begin{aligned} R_{equiv} &= N_{equiv} R_{equivNC} \\ L_{equiv} &= N_{equiv}^2 L_{equivNC} \\ k_{fcem} &= N_{equiv} k_{fcemNC} \\ G_{Mequiv} &= N_{equiv} G_{MequivNC} \end{aligned} \tag{2}$$

where the *NC* (Nominal Conditions) subscript specifies a quantity referred to a non-faulty condition.
This model does not allow to discriminate the fault in one phase from that in another, but only shows a net increase in equivalent[1] current and maximum actuating speed. Figure 3 shows the equivalent current trend resulting from a chirp command for the reference and monitor model, using the N_{equiv} approximation.

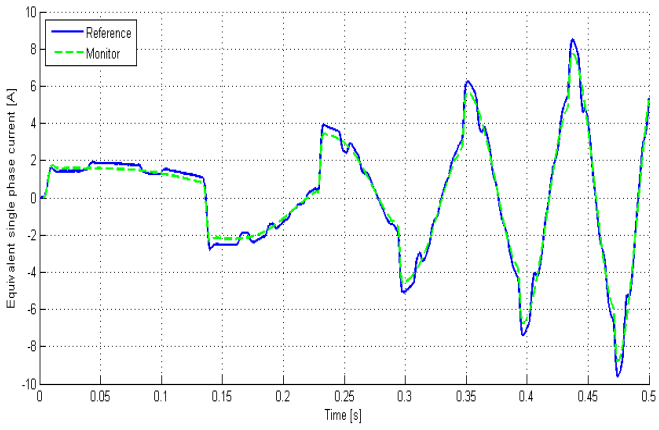

Figure 3 Response of the proposed Monitor Model with the N_{equiv} approximation.

1 Equivalent current refers to the current of the single-phase model for the Monitor; for the Reference Model, it is defined as the envelope of the three phase currents, computed as:

$$I_{ref} = \frac{I_A + I_B + I_C}{2} \cdot sign(T_M)$$

where T_M is the motor torque.

Moreover, the Rotor Static Eccentricity (RE) fault cannot be simulated with the same technique: unlike the Phase Short Circuit (PSC) fault, the RE has little-to-no effect on overall actuator performance intended as position and speed control, even in open-loop response. In fact, this fault causes the Torque Gain (*GM* gain in Fig. 2) and Counter Electromotive Force Gain (*kem*) to increase in some angular positions and to decrease in others so that the disturbance, averaged over one revolution, is null; the mechanical system characteristic time is significantly longer than the electromagnetic system one, so inertial effects of the rotor act as a low-pass filter over the torque signal, suppressing the high frequency noise in the angular velocity of the rotor, which does not differ appreciably from that of the nominal system. For these reasons, some modifications of the MM are required to better simulate the damages, improving the accuracy of optimization-based FDI techniques.

5 ENHANCED EMA MONITOR MODEL

To correctly replicate the Reference response to the electrical faults avoiding the costly simulation of the three-phase electromagnetic model, the MM needs to renounce a strict correlation to the physical phenomena generating the effect of the aforesaid faults on the EMA performance, as in the model-based approaches; the MM is indeed modified to produce the effect of PSC and RE regardless of their physical origin. This is achieved by the introduction of two shape functions used to modulate the electromagnetic parameters of the equivalent single-phase model as a function of fault magnitude and rotor angular position (schematically shown in Fig. 4).

5.1 MODULATING FUNCTION-BASED – PSC FAULT

The approach employed for the PSC fault consists in multiplying the stator resistance, torque gain and back-EMF coefficient by the fraction of windings working at each instant. Since two phases are active at a time, the modulating function is defined as:

$$f(\theta_m) = \begin{cases} \dfrac{N_b + N_c}{2}, & -\dfrac{\pi}{6} < \theta_e < \dfrac{\pi}{6} \\ \dfrac{N_c + N_a}{2}, & \dfrac{\pi}{6} < \theta_e < \dfrac{\pi}{2} \\ \dfrac{N_a + N_b}{2}, & \dfrac{\pi}{2} < \theta_e < \dfrac{5}{6}\pi \end{cases} \tag{3}$$

where $\theta_e = P\,\theta_m$ is the normalized electrical rotor angle, limited in a range of amplitude π. This is equivalent to consider, for the evaluation of the equivalent short circuit parameter, only the two active phases for a given θ_m. Since this modulating function is difficult to express with a syntax compatible with the Simulink *Fcn* block, the subsystem shown in Fig. 5 is adopted. The non-normalized rotor position is fed in input, and the active phase computation block returns the integer values {1,2,3} depending on the active phases; subsequently, the multiport switch block commutates the corresponding constant value, which is returned as output.

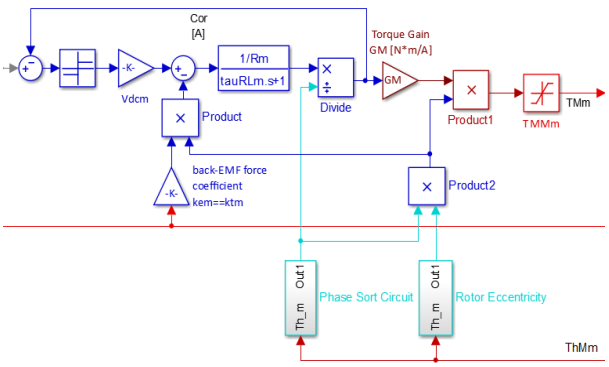

Figure 4 Modification of the Monitor Model to introduce the two shape functions.

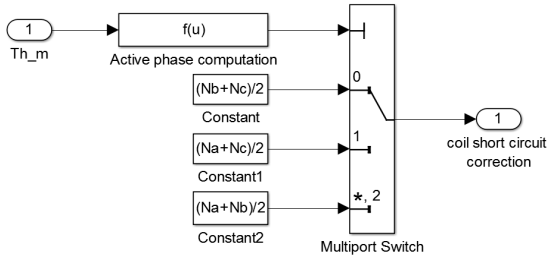

Figure 5 Short circuit subsystem.

The active phase computation block employs the function:

$$f(u) = floor\left[3\left(\frac{Pu}{\pi} + \frac{1}{6}\right) - 3floor\left(\frac{Pu}{\pi} + \frac{1}{6}\right)\right] \tag{4}$$

where P is the number of pole-pairs and $u = \theta_m$ is the block input signal. A simpler alternative would be to call an external MATLAB function, but this would lengthen unacceptably the computing time, even in the Accelerator Mode. With this modification, the equivalent current waveform produced by a PSC is reproduced by the monitor model in a quite accurate way as shown in Fig. 6, allowing an improved recognition of the fault even when considered in combination with other damages. Moreover, the phase affected by PSC can be identified, even if this information may not have a great relevance for maintenance purposes.

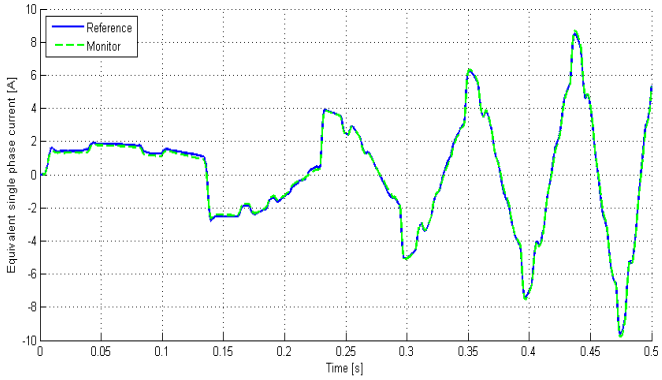

Figure 6 Response of the proposed Monitor Model with a 50% phase A short circuit.

5.2 MODULATING FUNCTION-BASED – RE FAULT

A similar approach to that described in Paragraph 5.1 is employed to model the effect of RE: a modulating function is used to multiply the torque gain (*GM*) and back-EMF coefficient (*kem*) to reproduce the Reference current signal. After some attempts, it is found that the correct waveform is accurately reproduced by using the correction:

$$K_{fcem}^{'} = K_{fcem}\,(1 - Z(\cos(P\theta_m + \phi) + \text{sawtooth}(6P\theta_m - \pi)\sin(P\theta_m + \phi)) \quad (5)$$

This shape function has no physical meaning, but is an effective and computationally light solution for producing the effect of a rotor eccentricity on the Monitor current signal; the parameter Z represents the damage magnitude, since it multiplies the shape function. In order to find the correlation between Z and ζ some optimizations are performed using known values of ζ. For values of ζ ranging from 0 to 1 a value of Z is found to minimize the quadratic error between reference and monitor response, using a gradient-based method. As it can be seen in Fig. 7, a linear function of ζ can be used to accurately approximate the parameter Z. With a least squares method one can find:

$$Z = 0.42\,\zeta \quad (5)$$

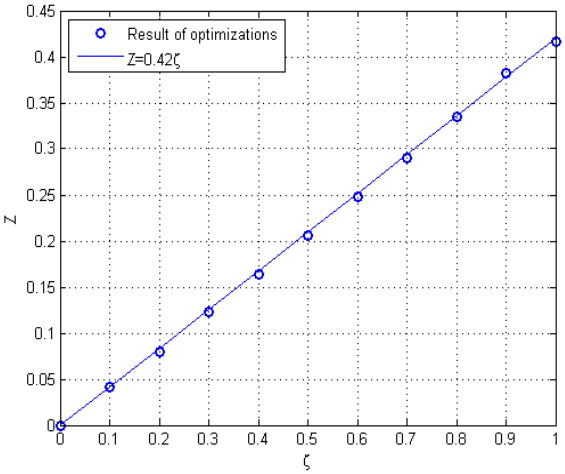

Figure 7 Linear fit of Z.

As shown in Fig. 8, this relation allows representing the correct waveform in a fairly accurate way, which reflects in improving the convergence of the genetic algorithm used for fault detection.

6 RESPONSE OF EMA MONITOR AND REFERENCE MODEL IN FAULTY CONDITIONS

Several combinations of commands and faults have been simulated to check for consistency of response between reference and monitor models. In fact, in order to perform a precise fault isolation, it is of critical importance that the monitor model is able to accurately reproduce the reference dynamic response, both in faulty and nominal conditions.

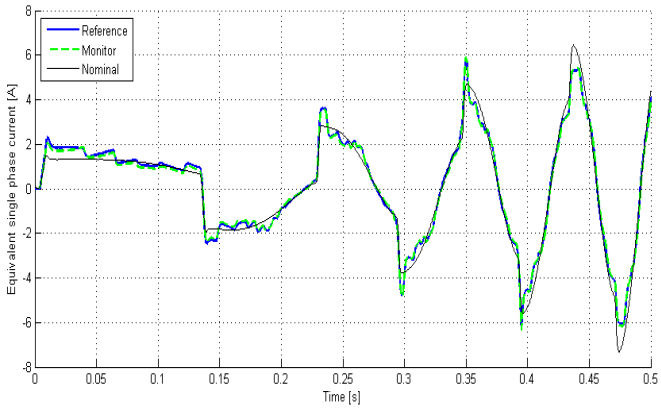

Figure 8 Response of the proposed Monitor Model with rotor eccentricity.

Figure 9 shows the response of Reference and Monitor models in nominal conditions. The proper setting of the MM parameters allows to exactly matching the Reference equivalent current: in this way, the error function returns a null value, ensuring convergence of the optimization. Figure 10 shows the behavior of the two models when multiple faults are introduced. It is possible to notice that the discrepancy between the two curves is small, and all the characteristic patterns produced by the incipient damages are correctly caught by the simplified model, meaning that the quadratic error function features a univocally located global minimum near the reference combination of faults. This should enable the GA optimization to effectively recognize the right damage levels, distributing the error variations among the four faults.

7 CONCLUSIONS

A simplified EMA Monitor Model has been developed to accurately reproduce the dynamic response of the Reference Model in terms of position, speed and equivalent current, even with the presence of various incipient faults. The high accuracy achieved in reproducing the effects of faults is a good starting point for the implementation of a robust and accurate GA-based optimization, leading to reliable and early fault isolation. The computing time for the simulation of a chirp command with the duration of 0.5 [s] is below one second[2] when using the Simulink *Accelerator Mode*. In this regard, it should be noted that the same simulation, performed with the Reference Model (more detailed and numerically burdensome) takes more than one minute: therefore, the computational cost is therefore compatible with a GA optimization for FDI performed during on-field pre-flight checks or scheduled maintenance.

2 The optimizations reported in this paper are performed on a desktop PC with Intel Core i5-3340 processor @ 3.10 GHz (6 MB Cache, up to 3.30 GHz) and 8 GB of RAM, running Windows 10 Home OS (64 bit architecture) and MATLAB R2012b.

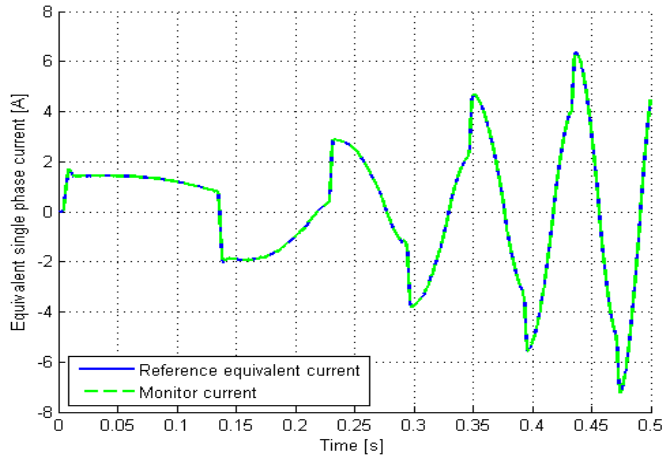

Figure 9 Response of Reference and Monitor models in Nominal Conditions.

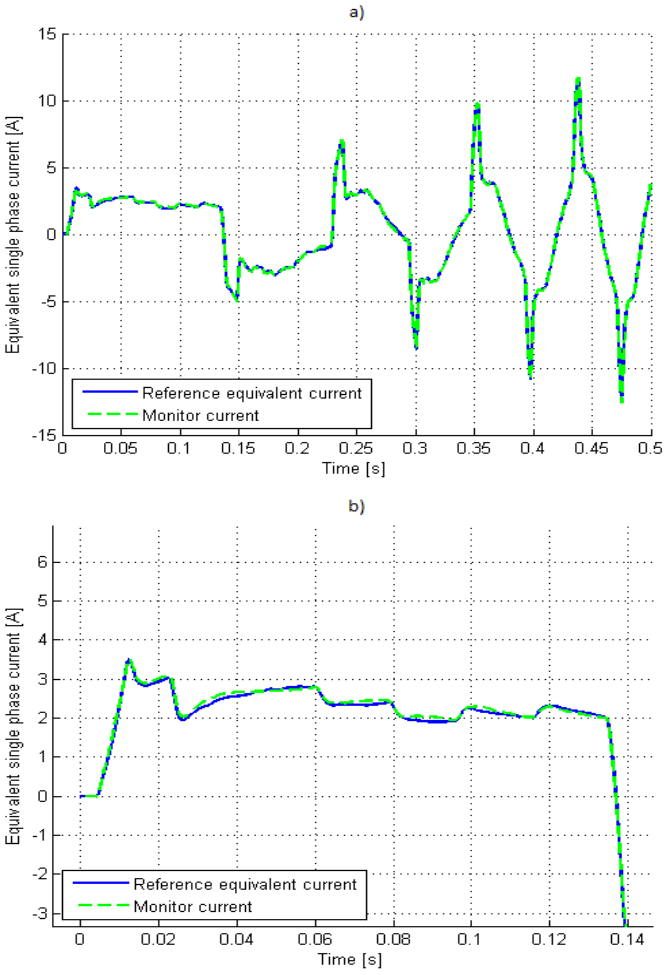

Figure 10 a) Response of the two models with multiple faults (180% of nominal friction, $4 \cdot 10^{-4}$ *rad* of backlash on the output shaft, 20% phase A PSC and RE of 20% the nominal air gap); b) Detail of the first 140 ms of response.

Real time in-flight monitoring is still impracticable, however, this solution would be excluded for other reasons, including regulation issues related to the non-deterministic nature of GAs and the technical difficulty of measuring aerodynamic loads to apply them to the Monitor Model. Future works will include the implementation and tuning of the GA optimization itself, the extension of the prognostic technique to a larger number of faults and possibly a further reduction of computing time, by simplifying the Monitor Model (for example pre-solving the controller current loop) or translating it in a lower level programming language.

REFERENCES

[1] Vachtsevanos G., Lewis F., Roemer M., Hess A., Wu B., *Intelligent Fault Diagnosis and Prognosis for Engineering Systems*. Wiley, 2006.

[2] Byington C.S., Watson W., Edwards D., Stoelting P., A Model-Based Approach to Prognostics and Health Management for Flight Control Actuators. *IEEE Aerospace Conference Proceedings*, 2014, USA.

[3] Quigley R.E.J., More electric aircraft. *Proc. of Eighth Annual IEEE Applied Power Electronics Conference - APEC '93*, San Diego, CA, pp. 906-911, 1993.

[4] Howse, M., All-electric aircraft. *Power Engi*neer, Vol. 17, No. 4, pp. 35-37, 2003.

[5] Borello L., Dalla Vedova M.D.L., Jacazio G., Sorli M., A Prognostic Model for Electrohydraulic Servo-valves. *Annual Conference of the Prognostics and Health Management Society*, San Diego, CA, 2009.

[6] Mamis M.S., Arkan M., Keles C., Transmission lines fault location using transient signal spectrum. *International Journal of Electrical Power and Energy Systems*, Vol. 53, pp. 714–718, 2013.

[7] Dalla Vedova M.D.L., Maggiore P., Pace L., Proposal of Prognostic Parametric Method Applied to an Electrohydraulic Servomechanism Affected by Multiple Failures. *WSEAS Trans. on Environment and Development*, Vol. 10, pp. 478-490, 2014.

[8] Dalla Vedova M.D.L., Maggiore P., Pace L., A New Prognostic Method Based on Simulated Annealing Algorithm to Deal with the Effects of Dry Friction on Electromechanical Actuators. *International Journal of Mechanics*, Vol. 9, 2015. ISSN: 1998-4448.

[9] Su H., Chong K. T., Induction machine condition monitoring using neural network modelling. IEEE Transactions on Industrial Electronics, Vol. 54, No. 1, pp. 241- 249, 2007.

[10] Hamdani S., Touhami O., Ibtiouen R., Fadel M., Neural network technique for induction motor rotor faults classification - dynamic eccentricity and broken bar faults. *IEEE International Symposium on Diagnostics for Electric Machines, Power Electronics & Drives (SDEMPED)*, pp. 626-631, 2011.

[11] Refaat S.S., Abu-Rub H., Saad M.S., Aboul-Zahab E.M., Iqbal A., ANN-based for detection, diagnosis the bearing fault for three phase induction motors using current signal. *IEEE International Conference on Industrial Technology (ICIT)*, pp. 253-258, 2013.

[12] Chopra I., Ganguli R., Haas D.J., Detection of Helicopter Rotor System Simulated Faults Using Neural Networks. *Proceedings of the 37th Structures, Structural Dynamics and Materials Conference*, 1996.

[13] Dalla Vedova M.D.L., De Fano D., Maggiore P., Neural Network Design for Incipient Failure Detection on Aircraft EM Actuator. *International Journal of Mechanics and Control (JoMaC)*, Vol. 17, No. 1, June 2016, pp. 77-83, ISSN: 1590-8844.

[14] Maggiore P., Dalla Vedova M.D.L., Pace L., Desando A., Evaluation of the correlation coefficient as a prognostic indicator for electromechanical servomechanism failures. *International Journal of Prognostics and Health Management*, Vol. 6, No. 1, 2015. ISSN: 2153-2648.

[15] Haskew T.A., Schinstock D.E., Waldrep E., Two-Phase On' Drive Operation in a Permanent Magnet Synchronous Machine Electromechanical Actuator. *IEEE Trans. on Energy Conversion*, Vol. 14, 1999.

[16] Lee B.K., Ehsani M., Advanced Simulation Model for Brushless DC Motor Drives. *Electric Power Components and Systems*, Vol. 31, No. 9, pp. 841-868, 2003. ISSN: 1532-5008.

[17] Hemanand T., Rajesh T., Speed Control of Brushless DC Motor Drive Employing Hard Chopping PWM Technique Using DSP. *Proceedings of India Intern. Conference on Power Electronics,* 2006.

[18] Hua, J., Zhiyong, H., Simulation of Sensorless Permanent Magnetic Brushless DC Motor Control System. *Proceedings of the IEEE International Conference on Automation and Logistics*, September 2008, China.

[19] Halvaei Niasar A., Moghbelli H., Vahedi A., Modelling, Simulation and Implementation of Four-Switch Brushless DC Motor Drive Based On Switching Functions. *IEEE EUROCON 2009*, St. Petersburg, pp. 682 -687, 2009.

[20] Çunkas M., Aydoğdu O., Realization of Fuzzy Logic Controlled Brushless DC Motor Drives using Matlab/Simulink. *Mathematical and Computational Applications*, Vol. 15, pp. 218-229, 2010.

[21] Borello L., Villero G., Dalla Vedova M.D.L., New asymmetry monitoring techniques: effects on attitude control. *Aerospace Science and Technology*, Vol. 13, No. 8, pp. 475-487, 2009.

[22] Borello L., Villero G., Dalla Vedova M.D.L., Flaps Failure and Aircraft Controllability: Developments in Asymmetry Monitoring Techniques. *Journal of Mechanical Science and Technology*, Vol. 28, No. 11, pp. 4593-4603, 2014. ISSN: 1738-494X.

[23] Borello L., Dalla Vedova M.D.L., A dry friction model and robust computational algorithm for reversible or irreversible motion transmission. *International Journal of Mechanics and Control*, Vol. 13, No. 2, pp. 37-4, 2012.

[24] Farooq J.A., Djerdir A., Miraoui A., Modelling and simulation of stator winding inter-turn faults in permanent magnet synchronous motors. *COMPEL - The International Journal for Computation and Mathematics in Electrical and Electronic Engineering*, Vol. 27, No. 4, pp. 887–896, 2008. ISSN: 0332-1649

[25] Kim B.W., Kim K.T., Hur J., Simplified impedance modeling and analysis for inter-turn fault of IPM-type BLDC motor. *Journal of Power Electronics*, Vol. 12, pp. 10-18, 2012. ISSN: 1598-2092

[26] Alamyal, M., Gadoue, S.M., & Zahawi, B., Detection of induction machine winding faults using genetic algorithm. *Diagnostics for Electric Machines, Power Electronics and Drives (SDEMPED), 9th IEEE International Symposium*, Spain, pp. 157-161, 2013.

[27] Dalla Vedova M.D.L, Germanà A., Maggiore P., Proposal of a new simulated annealing model-based fault identification technique applied to flight control EM actuators. *Risk, Reliability and Safety: Innovating Theory and Practice: Proceedings of ESREL 2016*, Glasgow, UK, 25-29 September 2016, pp. 313-321. ISBN: 978-1-138029-97-2.

ISSN 1590-8844
International Journal of Mechanics and Control, Vol. 17, No. 02, 2016

EXTERNAL AND INTERNAL CFD ANALYSIS OF A HIGH-SPEED HUMAN POWERED VEHICLE

Paolo Baldissera Cristiana Delprete

Politecnico di Torino, Department of Mechanical and Aerospace Engineering

ABSTRACT

Human powered vehicle competitions provide a stimulating research field aiming at the development of high-efficiency and sustainable means of transportation. Aerodynamic studies about top-speed bicycles, even if classified as sport engineering, are able to increase the knowledge also for the design of their commuting version such as three-wheeled velomobiles. In the present paper, some of the design and manufacturing features that play a key role in the aerodynamic performance of such vehicles are discussed. Then, a critical review of a case study prototype is presented and five CFD models of the same vehicle are compared and discussed. In particular, two aspects are investigated and quantified in terms of power loss: the negative effects of surface discontinuities on the laminar-turbulent transition of the boundary layer and the crucial role of wheel-wells for a properly working internal ventilation.

Keywords: CFD, HPV, Design, Sport, Cycling

1 INTRODUCTION

Although not included in classical sport disciplines and banned from traditional cycling, Human Powered Vehicles (HPVs) offer an interesting field for educational [1] and research purposes in many disciplines.

While the definition of HPVs indicates a wide general category of vehicles, it is well assessed by the last century results that full faired recumbent bicycles and tricycles are the fastest and the most efficient HPVs. The records sanctioned by national and international HPV associations [2,3] are often similar to traditional cycling such as the classic one hour travelled distance, the standing start kilometre and the flying start 200 m sprint for the top-speed. A special event in this field is the World Human Powered Speed Championship (WHPSC) [4] yearly held in Battle Mountain (Nevada, US). Here, the speed is averaged over a 200 m trap at the end of a quite flat segment (average slope −0.6%) of 8 km on the State Route 305. In September 2015 the Canadian rider Todd Reichert pushed the world record up to 139.45 km/h with the accurately designed and manufactured prototype Eta (Aerovelo Team) [5].

Contact author: Paolo Baldissera[1]

[1] Politecnico di Torino
Dept. of Mechanical and Aerospace Engeneering
Corso Duca degli Abruzzi, 24 - 10129 Torino, Italy
Email: paolo.baldissera@polito.it

Despite the measurement range corresponds to UCI (Union Cycliste Internationale) sprint, the effort is different. Each run requires 3-4 minutes of aerobic activity, around 1 minute of anaerobic power ramp and a maximal effort for the last 40-60 seconds: this is a longer and harder effort compared with the short-time needed in UCI 200 m sprint (current record 77.03 km/h, François Pervis, 2013 [6]).

Scientific papers about HPVs were published in the last decades focusing on many aspects such as ergonomics [7,8], aerodynamics [9-11] and high-speed handling [12]. Another valuable source of short technical information is the magazine collection Human Power [13].

The Policumbent Student Team [14] supervised by the authors had its debut at the WHPSC 2015. The rider Andrea Gallo set the Italian speed record of 116.19 km/h on the prototype PulsaR. The testing and racing experience has given the opportunity to understand both design and manufacturing limitations of the current project. As a consequence, a development program has been started in order to improve the current prototype and to develop a totally new design for challenging the world record in 2017.

In the present article the key aspects in aerodynamic design of high-speed HPVs will be discussed. Through Computational Fluid Dynamics (CFD) analysis with different focuses and modelling approaches on PulsaR, both external and internal flows will be analysed and discussed in comparison with the achieved speed.

2 KEY ASPECTS IN HPV AERODYNAMICS

In the design of full faired HPVs for top speed record attempts, a crucial role is played by the aerodynamic drag. In particular, two key aspects can determine success or failure in this field:

- the knowledge to design a shape with natural laminar flow and with the minimal volume fitting the rider size;
- the ability to keep the laminar flow in real world conditions.

These two aspects will be briefly discussed in the next paragraphs in order to point out vehicle design evolution and possible future developments.

2.1 LAMINAR FLOW DESIGN

The design of a streamlined body allowing for an extended laminar boundary layer at a given range of speed is a challenge that concerns many engineering applications dealing with different fluids.

The boundary layer around a body is defined as laminar when the air particles move in orderly way, which means in parallel layers with no mixing and eddies. When critical conditions are reached, the transition of the boundary layer from laminar to turbulent occurs and the flow starts to mix and to behave in irregular ways. The two conditions are represented in Figure 1 for an observer moving with the body wall. A laminar boundary layer results in a lower skin friction over the immersed body and provide a reduced drag with respect of the turbulent one. For this reason laminar design is a key factor in HPVs and in almost all sport competitions involving vehicle speed.

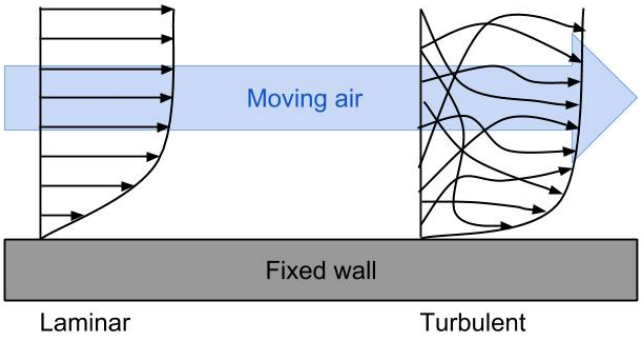

Figure 1 Laminar and turbulent boundary layers.

2.2 FROM THE VIRTUAL TO THE REAL WORLD

The second key point involves the ability to evaluate and to minimize the production imperfections and the external factors that could potentially undermine the original design. Some examples of manufacturing details that are potential sources of turbulence are:

- badly thermoformed front windscreen;
- non-smooth junction of the front windscreen or of any opening for the rider or for the maintenance;
- thick sponsor stickers on the fairing.

In practice, due to strict timeline and inexperience, all these considerations were neglected during the first manufacturing of PulsaR, as pointed out in Figure 2. In particular, the acrylic glass in the upper front of the vehicle was not properly thermoformed and assembled, likely resulting in a strong limitation of the laminar boundary layer extension.

Concerning external conditions in the real world, particular attention should be given to:

- lateral wind up to 6 km/h (legal limit from any direction for record validation);
- vibrations of the external fairing, coming from the road and through the vehicle frame.

Finally, the air flow entering and exiting from the vehicle can also affect its aerodynamic performance and is worthy of a specific discussion in the next paragraph.

2.2.1 Rider ventilation and internal flow

By enclosing the rider into an aerodynamic shell the need for a ventilation system arises. Such system has to meet the following requirements:

- to provide the right amount of oxygen for the required effort and weather conditions;
- to grant a proper temperature and humidity level;
- to ensure proper cooling for the brakes;
- to dry windows (if any) in order to avoid fogging;
- to minimize any additional drag.

The WHPSC competition rules then provide an additional requirement by excluding any additional source of energy for propulsion and for cooling (i.e. no ice-packs or heat storage systems). Ventilation through active fans is allowed only when the required energy is drained from muscular input and then subtracted from propulsion. In other words, the most natural solution is to have one or more air intakes and outlets working progressively with the vehicle speed.

Concerning the first requirement, the overall need in terms of air flow rate can be estimated by taking into account the kind of effort required and physiological data of the rider. The case of endurance disciplines requires to consider the large portion of ventilation aimed at cooling and drying the rider. Indeed, with an overall efficiency of about 25%, the human body deliver a heating power which is three times the mechanical power during cycling. It means that a professional cyclist giving 400 W of mechanical power for one hour will be dissipating 1200 W of power into heat. A detailed study about ventilation for cooling in endurance races can be found in [15].

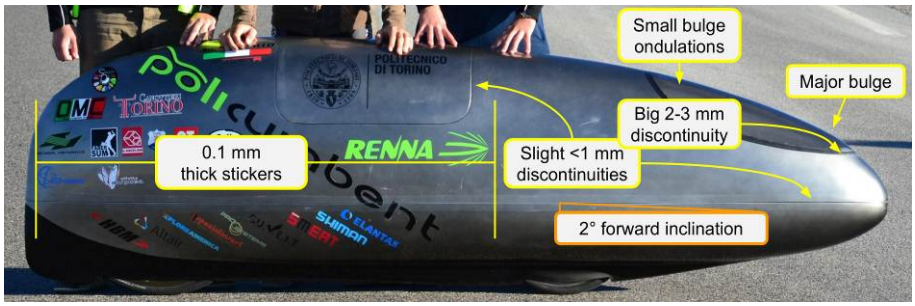

Figure 2 PulsaR 2015 with highlighted turbulent transition sources.

As a comparison, in [10] about 100 l/min are given as a general reference value for the air flow needed to breathe properly in maximal effort conditions, while the overall requirement can rise up to 1200 l/min for cooling the rider in case of endurance competitions.
Technical solutions for collecting and expelling the air in HPVs have some advantages and drawbacks. The practical experience of builders and riders attending the WHPSC suggests that:

- lateral NACA (National Advisory Committee for Aeronautics) ducts are an option, but can induce turbulent transition in the external flow and are more invasive than stagnation point intakes;
- wheel rotation significantly affects the overall drag, and it is strongly suggested to insulate them by means of dedicated wells;
- internal flow plays a not negligible role and is worthy of accurate study and implementation.

A common practice is to have a diffuser cone behind the intake hole in order to obtain a double effect: to reduce the air speed towards the rider and to recover the pressure drop on the nose of the vehicle. Indeed, frontal pressure on streamlined shapes is a double-edged sword: on the one hand it is a direct source of drag, on the other hand a certain amount of pressure is a requirement for the flow to stay laminar along a large portion of the vehicle body.

3 PULSAR CFD MODELS

The CFD analysis is a numerical technique for solving the Navier-Stokes equations that has been developed in the Aerospace and Automotive industrial fields. Thanks to the current accessibility of high computational resources at affordable prices, it is now applied to a wide range of fluid dynamics problems also in sports engineering such as nautical disciplines, from America's Cup [16] to kayak [17] and rowing boats [18-20], in swimming [21-23] and is a well-established method in cycling [24-31].
CFD analysis was used during the design phase of PulsaR in order to assess and optimize its shape. However, after the result obtained in September 2015 in Nevada with this prototype, the critical review and improvement of the CFD model was considered as a key activity for many reasons:

- to improve the model accuracy in assessing the PulsaR design limits in its ideal shape;
- to investigate the manufacturing errors and their possible solutions;
- to identify further potential improvements in order to push the vehicle at its potential top speed;
- to gain awareness of the intrinsic limitations of the vehicle shape in order to start a new project.

Since the above list of purposes involves the study of different phenomena and conditions, two groups of models were implemented in CD-Adapco StarCCM+®:

1. EXT group only considers the external flow over the closed volume of the fairing with the protrusion of the wheels;
2. INT group also includes the internal flow with a simplified representation of the inner structure, the rider and the rotating parts (Figure 3).

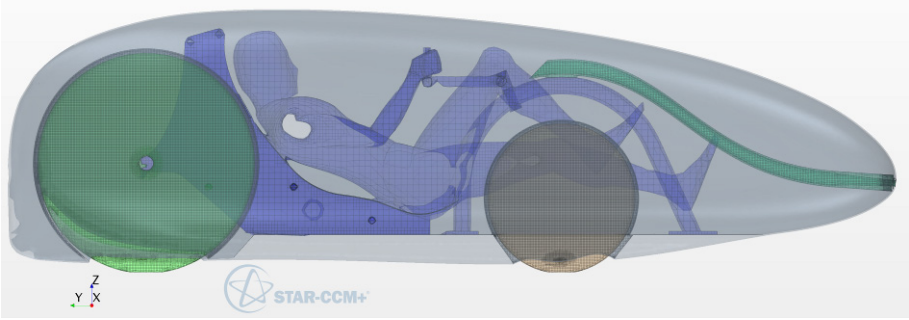

Figure 3 CFD mesh of the simplified internal elements for the INT-YW model (see Table I).

For both groups the simulations were performed at a speed of 125 km/h (as 2016 target) in open road conditions, which means in a large virtual tunnel of 25×6×8 m with PulsaR being 2.8×0.4×0.8 m (Figure 4). For all the models the ground was imposed as moving with the air and with no slip boundary condition.

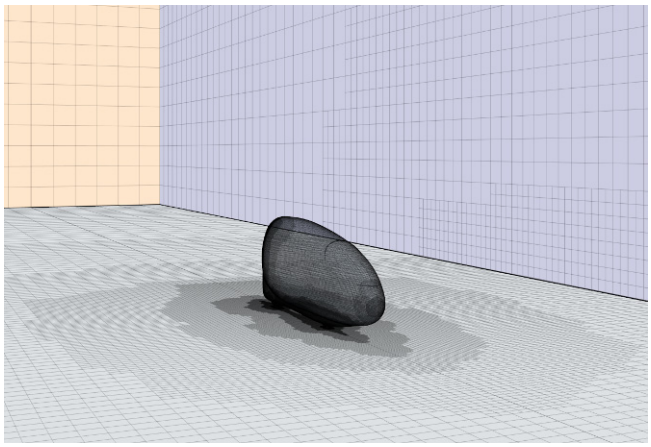

Figure 4 CFD mesh overview.

A speed-coherent rotation of the wheels (or of their protruding portion) was also imposed as boundary condition in both groups.
The EXT group includes three models:

1. EXT-A represents the perfect ideal shape of PulsaR in its horizontal alignment with respect to the ground and with a smooth continuous surface except for the protruding wheels. The model is aimed to an accurate evaluation of the laminar-turbulent transition, with a 30 prism layers for the boundary and Gamma-Re-Theta modelling for the transition;
2. EXT-B is an approximation of the manufactured shape of PulsaR 2015, with 2° forward inclination and bulgy windscreen having an irregular 2-3 mm misalignment with respect to the fairing surface (Figure 5). As for the previous, this model has 30 prism layers and Gamma-Re-Theta transition;
3. EXT-C has the same ideal geometry of model EXT-A, but is simulated with a Spalart-Almaras full turbulent model without laminar flow.

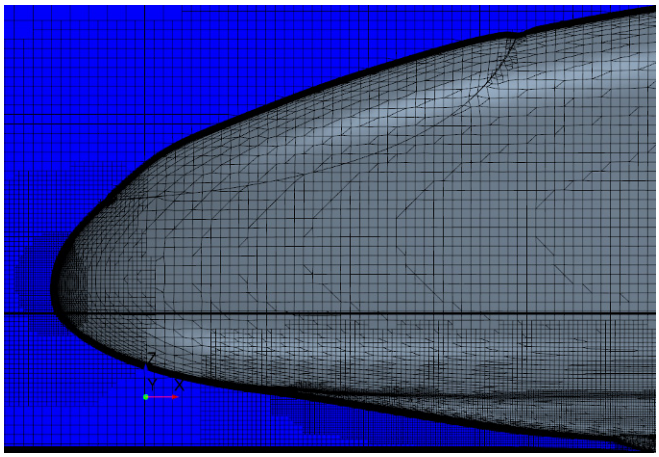

Figure 5 EXT-B model detail of the bulgy windscreen shape and steep junction.

The INT group, due to geometrical complexity and convergence stability, is not suitable for a transitional modelling. As a consequence its sub-models were calculated by using a fully turbulent boundary layer approach based on the Spalart-Almaras formulation. This group includes two models:

1. INT-NW has no wheel-wells as in the 2015 version of PulsaR;
2. INT-YW has front and rear wheel-wells with 7.5 mm clearance that insulates rather totally the rotational air flow from the inner volume, except for a small circular opening close to the rear hub.

A summary of the CFD models is reported in Table I.
For both EXT and INT groups a trimmer mesh was used plus the above mentioned prism layer, that was reduced to 3 levels in the case of the fully turbulent Spalart-Almaras simulations (EXT-C and the two INT models).
The meshing of INT models required the use of the wrapping function in order to identify and simplify the intersections among the various body inside the fairing.
The EXT group models resulted in mesh around 1.2 million cells by taking advantage of longitudinal plane symmetry, while the non-symmetrical INT group models required about 6.6 million cells to be carefully represented, even if the prism layer was limited to the fairing and to the tube.

Table I Summary of the CFD models and their characteristics.

Model	Description	Turbulence model	Transition model
EXT-A	External flow on perfect ideal surface	K-Omega	Gamma-Re-Theta
EXT-B	External flow, bulgy and misaligned windscreen, 2° forward inclination	K-Omega	Gamma-Re-Theta
EXT-C	External flow on perfect ideal surface	Spalart-Almaras	Fully turbulent
INT-NW	External and internal flow without wheel-wells	Spalart-Almaras	Fully turbulent
INT-YW	External and internal flow with both wheel-wells	Spalart-Almaras	Fully turbulent

4 CFD ANALYSIS RESULTS

All the simulations were run on 64 cores (AMD Opteron 2.3 GHz) over two nodes of a high performance computing cluster (ref. Acknowledgements). The EXT models converged in less than 1000 iterations with an overall CPU time of about 12 hours each, while the INT models converged after 1600 iterations for an overall CPU time of 56 hours each.
The results in terms of drag coefficient, force acting against the vehicle and equivalent power at 125 km/h of speed are summarized in Table II.

Table II Calculated drag coefficient, force and power at 125 km/h for the five implemented CFD models.

Model	Drag coefficient C_d	Total drag F_d [N]	Equivalent power [W]
EXT-A	0.0369	6.83	237
EXT-B	0.0505	9.34	324
EXT-C	0.0739	13.66	474
INT-NW	0.0826	15.30	531
INT-YW	0.0789	14.62	508

The results confirm the wide range of performance that can be achieved depending on the external flow conditions and provides useful indications about the role of the internal flow and the potential benefits from wheel-wells.
Moreover, a validation of the model comes from the coast-down measurements performed on a testing track with PulsaR in October 2015. Here, a drag coefficient C_d of 0.0834±0.010 was estimated from three repetition average and with an air density ρ of 1.1899 kg/m^3. Indeed, by considering the drag force F_d derived by definition of C_d and by applying the PulsaR frontal area of 0.259 m^2 it can be estimated for a speed of 125 km/h:

$$F_d = \frac{1}{2}\cdot\rho\cdot C_d\cdot A\cdot v^2 = 15.49\pm 0.37 \text{ N} \quad (1)$$

The obtained value is close to the CFD calculation with model INT-NW, which is in fact the most representative with respect to the tested prototype.
In the following, the specific information that can be argued by comparing the different models will be discussed separately for EXT and INT model groups.

4.1 EXTERNAL FLOW MODEL RESULTS

The drag estimations provided by EXT models A, B and C give support to the above mentioned key role of the manufacturing accuracy on the external surface. The drag resistance is doubled when passing from the maximum laminar boundary extension of model A to the fully turbulent boundary layer of model C. Model B represents a compromise between the other two, pointing out the remarkable influence of the windscreen imperfections on the transitional behaviour and on the final drag. As shown in Figure 6, the impact of such imperfections on the boundary layer is important and the laminar-turbulent transition is anticipated by the misaligned windscreen, especially in the top part of the fairing, where the potential laminar extension is maximum. The cost of this imperfection in terms of power is up to 87 W at 125 km/h.

The analysis points out that also the original design shape in its ideal condition has some limitations concerning the extension of laminar boundary layer. Indeed, the side of the vehicle is rather flat and does not allow to maintain a proper pressure gradient in order to avoid the transition.
Also, the last part of the tail shows an area with a drop in the wall shear stress (deep blue in upper Figure 6), suggesting a potential undesired detach of the flow.
All these considerations, together with the observation of the kind of shapes designed for the fastest prototypes such as the world record holder, provides valuable indications for developing the next speed-bike of the Team.

4.2 EXTERNAL-INTERNAL FLOW MODEL RESULTS

Before analysing the effect of the wheel-wells, it is interesting to discuss the increase in drag from model EXT-C to the INT models. While the EXT-C model represents a “worst condition” among the EXT group, it can be considered as “best ideal condition” with respect to INT models, at least within the fully turbulent approach. Model EXT-C represents the situation in which there is virtually no drawback from the inside flow on the external drag. From this perspective, model INT-NW estimates an increase of 1.64 N (+12%) of the overall drag, while the additional drag is reduced to 0.96 N (+7%) by mounting the wheel-wells as in model INT-YW. Assuming by hypothesis the same additional drag on the transitional model EXT-A the percentage increase is even bigger: +24% without wheel-wells and 14% with them.
In general, the additional drag at the simulated speed can be translated into additional power required for the rider by multiplying force and speed (125 km/h), leading to:

- +56.9 W without wheel-wells;
- +33.3 W with wheel-wells.

It follows that the use of wheel-wells can save 23.6 W at 125 km/h of speed, a significant amount of power when dealing with human effort and top-speed records. By plotting the power required to overcome the air drag as a function of the speed as in Figure 7, it is possible to visualize the improvement and eventually calculate the expected gain in top-speed by entering the measured or estimated 60 s sprint power of the rider on the vertical axis. As an example, the introduction of the wheel-wells could potentially provide an increase of 2 km/h, passing from 125 to 127 km/h with 530 W of power (to be summed to the power required to overcome the tyre rolling resistance). The improvement is clearly more important when passing to transitional models taking into account the portion of laminar boundary layer on the surface.

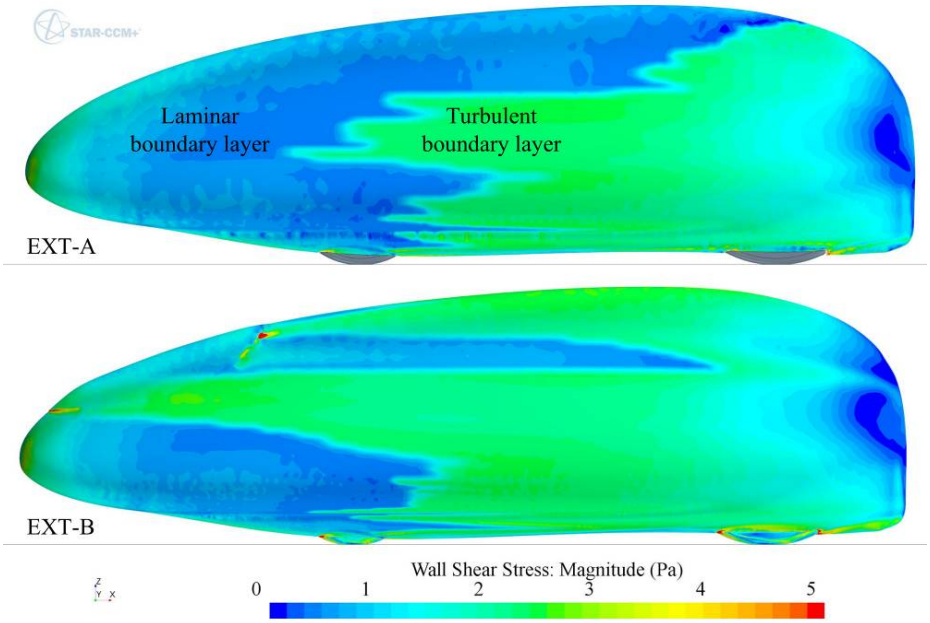

Figure 6 Wall shear stress and laminar boundary layer extension over EXT-A and EXT-B models.

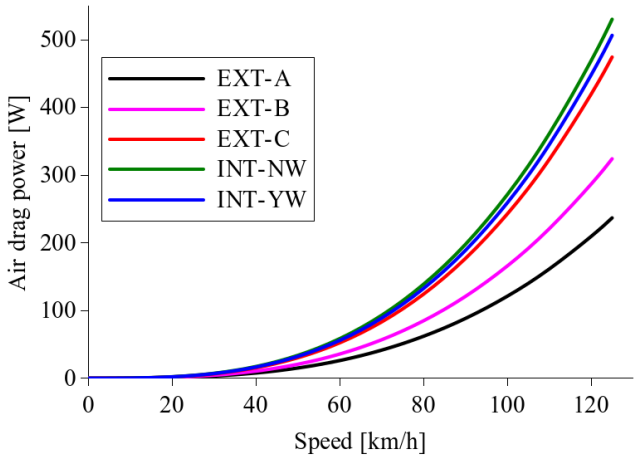

Figure 7 Power vs. speed curves of the CFD models.

Besides the gain in terms of drag, it is interesting to observe what the CFD analysis highlights about the behaviour of the flow inside the vehicle. As shown in Figure 8, the absence of wheel-wells produces a strongly randomized internal flow. Moreover, due to the proximity of the rear wheel to the air outlet cut, the behaviour of the latter is reversed. It means that the air is entering where it was originally designed to exit. This air is then summed to the air entering the front inlet and expelled through the wheels generating an increased turbulence in the bottom part of the vehicle, close to the ground, which is likely to increase the shear stress and thus the drag in that region. This result provides a useful information not only for the purpose of sport records, but also for the proper design of three-wheeled velomobiles [32] for daily commuting over an extended range with respect to standard bicycles. Such kind of vehicles, in many contexts, could represent the missing link between bicycle and cars as solution for a pollution free, healthy and safe personal mobility. One of their main limitation for the use in warm seasons and countries is exactly the internal ventilation to control the rider temperature and to extract the steam.

6 CONCLUSIONS

The key aspects for achieving high aerodynamic efficiency in HPVs were discussed with a focus on some manufacturing details. A critical review of an existing top-speed prototype (PulsaR 2015) was presented and five CFD models were implemented in order to quantify the role of the discussed features. In particular, a special focus was given to two topics, obtaining the following observations and estimations:

1. the surface smoothness and continuity is confirmed to play a crucial role in maintaining an extended laminar boundary layer over the vehicle and the presence of a small discontinuity in the windscreen junction can determine an increase of 37% in the coefficient of drag, which is potentially doubled in the worst case of a fully turbulent vehicle;
2. the use of internal wheel-wells can provide a significant improvement in the aerodynamic performance with a saving of 23.6 W of power at a speed of 125 km/h;
3. another important role of wheel-wells is to maintain a functional airflow inside the vehicle, avoiding the outlet cut to behave as an inlet and reducing the disturbance close to the ground.

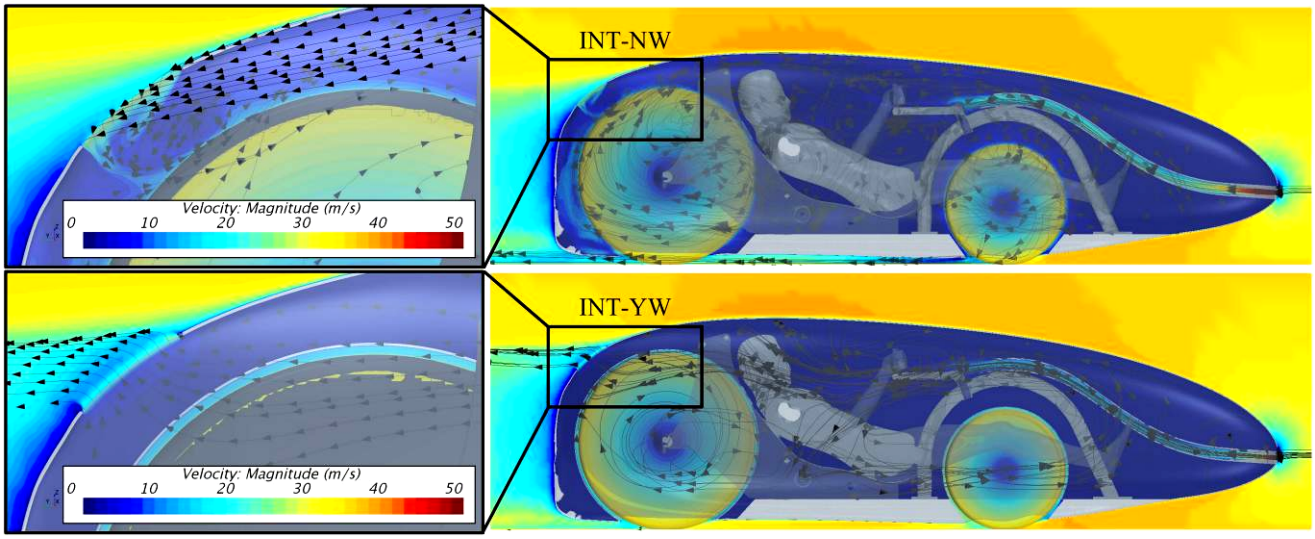

Figure 8 Overview and detail of the CFD calculated external and internal flow without wheel-wells (INT-NW) and with wheel-wells (INT-YW).

After horizontal realignment of the prototype through a fork spacer, replacement of the windscreen with a better one, accurate stuccoing of its junction and implementation of the only rear wheel-well, a rough 10% increase in top-speed was measured on PulsaR during a preliminary track test in Spring 2016. Further improvements and more detailed coast-down assessment are planned in June and July 2016, waiting for the WHPSC trials in Battle Mountain on September 12-17, 2016.

ACKNOWLEDGEMENTS

Computational resources were provided by HPC@POLITO which is a project of Academic Computing within the Department of Control and Computer Engineering at the Politecnico di Torino (http://www.hpc.polito.it).
StarCCM+ licenses were kindly provided by CD-Adapco as official partner of the Policumbent Team project.

REFERENCES

[1] Baldissera P., Delprete C., Human powered vehicle design: a challenge for engineering education. *Procedings of ESDA*, Copenhagen, June 25-27, 2014.

[2] www.ihpva.org, accessed on May 27, 2016.

[3] www.whpva.org, accessed on May 27, 2016.

[4] http://recumbents.com/wisil/whpsc2016/speedchallenge.htm, accessed on May 27, 2016.

[5] www.aerovelo.com, accessed on May 27, 2016.

[6] http://www.uci.ch/mm/Document/News/NewsGeneral/16/60/64/20151009_Historiquedesrecords_HommesElite_Neutral.pdf, accessed on May 27, 2016.

[7] Capelli C., Ardigò L., Schena F., Zamparo P., Energy cost and mechanical efficiency of riding a human-powered recumbent bicycle. *Ergonomics*, Vol. 51, No 10, pp. 1565-1575, 2008.

[8] Reiser II R., Peterson M., Broker J., Anaerobic Cycling Power Output With Variations in Recumbent Body Configuration. *Journal of Applied Biomechanics*, Vol. 17, No. 3, pp. 204-216, 2001.

[9] Kyle C., Burke E., Improving the racing bicycle. *Mechanical Engineering*, Vol. 106, No. 9, p.34, 1984.

[10] Kyle C. R., Weaver M. D., Aerodynamics of human-powered vehicles. *Proc IMechE Part A: Journal of Power and Energy*, Vol. 218, No. 3, 141-154, 2004.

[11] Epema H., Van den Brand S., Gregoor W., Kooijman J., Pereboom H., Wielemaker D., Van der Zweep C.-J., Bicycle Design: A different approach to improving on the world human powered speed records. *Procedia Engineering*, Vol 34, pp. 313-318, 2012.

[12] Patterson W., Leone G., The Application of Handling Qualities to Bicycle Design. *Proceedings of Bicycle and Motorcycle Dynamics*, pp. 1-10, 2010.

[13] *Human power - The technical journal of the international human powered vehicle association* (1977-2004). Accessed on May 27, 2016 at http://www.ihpva.org/hparchive.htm.

[14] www.policumbent.it, accessed on May 27, 2016.

[15] W.B. Schreur, *Human Power eJournal* (2004), published online on http://www.hupi.org, accessed on April 5, 2016.

[16] Nicolopoulos D., Berton E., Gouvernet G. et al., A hybrid numerical method to develop america's cup yacht appendages. *Sports Engineering*, 11(4), pp. 177-185, 2009.

[17] Banks J., Phillips A.B., Turnock S.R. et al., Kayak blade-hull interactions: A body force approach for self-propelled simulations. *Proc IMechE Part P: Journal of Sports Engineering and Technology*, Vol. 228, No. 1, pp. 49-60, 2014.

[18] Coppel A., Gardner T.N., Caplan N. et al., Simulating the fluid dynamic behaviour of oar blades in competition rowing. *Proc ImechE Part P: Journal of Sports Engineering and Technology*, Vol. 224, No. 1, pp. 25-35, 2010.

[19] Sliasas A. and Tullis S., Numerical modelling of rowing blade hydrodynamics. *Sports Engineering*, Vol. 12, No. 1, pp. 31-40, 2009.

[20] Sliasas A. and Tullis S., The dynamic flow behaviour of an oar blade in motion using a hydrodynamics-based shell-velocity-coupled model of a rowing stroke. *Proc IMechE Part P: Journal of Sports Engineering and Technology*, Vol. 224, No. 1, pp. 9-24, 2010.

[21] Bixler B. and Riewald S., Analysis of a swimmer's hand and arm in steady flow conditions using computational fluid dynamics. *Journal of Biomechanics*, Vol. 35, No. 5, pp. 713-717, 2002.

[22] Rouboa A., Silva A., Leal L. et al., The effect of swimmer's hand/forearm acceleration on propulsive forces generation using computational fluid dynamics. *Journal of Biomechanics*, Vol.39, No.7, pp. 1239-1248, 2006.

[23] Hayati A.N., Ghaffari H. and Shams M., Analysis of free-surface effects on swimming by the application of the computational fluid dynamics method. *Proc IMechE Part P: Journal of Sports Engineering and Technology*, published online before print, 2015.

[24] Blocken B., Defraeye T., Koninckx E. et al., CFD simulations of the aerodynamic drag of two drafting cyclists. *Computers & Fluids*, Vol. 71, pp. 435-445, 2013.

[25] Defraeye T., Blocken B., Koninckx E. et al., Aerodynamic study of different cyclist positions: CFD analysis and full-scale wind-tunnel tests. *Journal of Biomechanics*, Vol. 43, No. 7, pp. 1262-1268, 2010.

[26] Defraeye T., Blocken B., Koninckx E. et al., Computational fluid dynamics analysis of cyclist aerodynamics: Performance of different turbulence-modelling and boundary-layer modelling approaches. *Journal of Biomechanics*, Vol. 43, No. 12, pp. 2281-2287, 2010.

[27] Defraeye T., Blocken B., Koninckx E. et al., Computational fluid dynamics analysis of drag and convective heat transfer of individual body segments for different cyclist positions. *Journal of Biomechanics*, Vol. 44, No. 9, pp. 1695-1701, 2011.

[28] Defraeye T., Blocken B., Koninckx E. et al., Cyclist drag in team pursuit: Influence of cyclist sequence, stature, and arm spacing. *Journal of Biomechanics*, Vol. 136, No. 1, 2013.

[29] Griffith M.D., Crouch T., Thompson M.C. et al., Computational fluid dynamics study of the effect of leg position on cyclist aerodynamic drag. *Journal of Fluid Engineering - T ASME*, Vol. 136, No. 10, 2014.

[30] Fintelman D., Hemida H., Sterling M. et al., CFD simulations of the flow around a cyclist subjected to crosswinds. *Journal of Wind Engineering & Industrial Aerodynamics*, Vol. 144, pp. 31-41, 2015.

[31] Blocken B. and Toparlar Y., A following car influences cyclist drag: CFD simulations and wind tunnel measurements. *Journal of Wind Engineering & Industrial Aerodynamics*, Vol. 145, pp. 178-186, 2015.

[32] Baldissera P., Delprete C., Tirelli M., Velomobiles: design guidelines. *International Journal of Mechanics and Control*, Vol. 13, No. 2, pp. 41-49, 2012.

ISSN 1590-8844
International Journal of Mechanics and Control, Vol. 17, No. 02, 2016

A COMPARISON OF STIFFNESS ANALYSIS METHODS FOR ROBOTIC SYSTEMS

Rogério Sales Gonçalves[*], Giuseppe Carbone[**], João Carlos Mendes Carvalho[*], Marco Ceccarelli[**]

* School of Mechanical Engineering, Federal University of Uberlandia, Uberlandia / MG, Brazil

** LARM, DiMSAT, University of Cassino and South Latium, Cassino, Italy

ABSTRACT

A robotic structure consists of a kinematic chain composed by links that can be rigid or flexible, interconnected by joints. One of the outstanding problems in robotic design and operation is to estimate a robot behavior under the action of external loads. In particular, it is needed a standard procedure to obtain the stiffness performance through the whole robot workspace. This paper presents a review about the main available methods to calculate the robotic systems stiffness performance in terms of a local Cartesian stiffness matrix. Specific attention is addressed to methods based on lumped parameters both by using the kinematic and dynamic forces distributions and by using Jacobian matrices. This paper also describes methods based on matrix structural analysis (MSA) and finite element analysis (FEA). Two cases of study have been reported to analyze and compare the above mentioned methodologies for providing a suitable mean to choose the most appropriate method for a given application.

Keywords: stiffness analysis, compliant displacements, matrix structural analysis, jacobian matrix, FEA

1 INTRODUCTION

A robotic structure is based on a kinematic chain composed by links that can be rigid or flexible and are interconnected by joints. One of the open issues in Robotics is to determine the stiffness performance of a robot within a standard procedure although several different stiffness analysis methods are available in a wide literature. Stiffness can be defined as the capacity of a mechanical system to sustain loads without excessive changes of its geometry, which are known as deformations or compliant displacements [1].
Compliant displacements produce negative effects on static behavior, fatigue strength, wear resistance, efficiency (friction losses), accuracy and dynamic stability (vibration), [1-4]. The growing importance of high accuracy and dynamic performance for robots, both with serial and parallel structures, has increased the use of high strength materials and lightweight designs achieving significant reduction of cross-sections and weight.

Contact author: Rogério Sales Gonçalves[1]

[1]Av. João Naves de Ávila, 2121 - Campus Santa Mônica - Uberlândia - MG - CEP 38400-902, Brazil.
E-mail: rsgoncalves@ufu.br

Nevertheless, these solutions also increase structural deformations and may result in intense resonance and self-excited vibrations at high speed [1]. Therefore, the study of the stiffness becomes of fundamental importance for the design of a robotic structure in order to properly choose materials, component geometry, shape and size, and interaction of each component with others.
The overall stiffness of a robot depends on several factors such as the size and material used for links, the mechanical transmission mechanisms, actuators and the controller dynamics as described, for example in [2]. In general, to achieve a high stiffness performance, many parts should be large and heavy. However, to obtain high speed motions most of the parts should be small and light. Additionally, the robot stiffness is greatly affected by robot configuration as reported for example in [3].
The aim of this paper is to describe how to obtain the Cartesian stiffness matrix for robotic structures using different methodologies. Considering an equilibrium situation of a robotic structure subject to a wrench applied on its end-effector if the wrench changes, compliant displacements will occur on the robotic structure. In a general case, translational and rotational displacements occur. The purpose of a stiffness analysis is to describe the stiffness of the overall structure through the derivation of a stiffness matrix that expresses the relationship between the

compliant displacements $\boldsymbol{\Delta x}$ occurring to a frame fixed at the end of the kinematic chain when a wrench $\boldsymbol{\Delta F}$ acts upon the mechanism structure. If necessary, compliant displacements of intermediate elements of the structure can be obtained too. It is to note that a stiffness matrix is obtained as function of the configuration. Thus, one stiffness matrix has to be calculated at each robot configuration. Then, it is also necessary to give a synthetic evaluation of global stiffness performance through the whole workspace, both for analysis and design purposes. For example, a global index of merit can be formulated by referring to the stiffness matrix as proposed in [40,41].

This paper gives an overview of the main available methods to calculate the robot stiffness, namely, methods using lumped parameters, methods using the Matrix Structural Analysis – MSA and methods using the Finite Element Analysis – FEA. Examples of numerical and experimental results are presented in order to analyze and compare those methodologies. In particular, numerical examples have been carried out as referring to a two degrees of freedom (dofs) serial structure and to a 6-RSS parallel structure. The aim of the above examples is to show the effectiveness and complexity of each formulation and to give an aid in choosing the most appropriate formulation for a specific robot application.

2 STIFFNESS MODELS

Hooke's law, or law of elasticity states that, for relatively small deformations, the compliant displacement or size of the deformation is directly proportional to the deforming force or, in other words, compliant displacements, within elastic limits, are proportional to the loads that cause them. Thus, considering a load P acting on a point A of an element, a corresponding displacement u_A is expressed as:

$$u_A = \lambda P \tag{1}$$

where λ is the proportionality coefficient between the force and displacement. This coefficient λ is function of the physical properties of the material, the relative position of point A, the application point of the load and the geometrical characteristics of the mechanical system.

A straight bar j with a uniform cross section will soffer compliant displacement, when moments and forces acts on its extremities, as sketched in Fig. 1(a) and Fig. 1(b).

Reference frames can be defined at the bar extremities i and $i+1$ where δ_x, δ_y, δ_z the linear compliant displacements while ϕ_x, ϕ_y, ϕ_z are the angular compliant displacements, along and about X-, Y- and Z- directions, respectively. Using the elastostatic properties of the bar one can obtain a 6x6 symmetrical stiffness matrix K that relates the applied forces/moments to compliant displacements in the form [4]:

$$\begin{bmatrix} F_x \\ F_y \\ F_z \\ M_x \\ M_y \\ M_z \end{bmatrix} = K \begin{bmatrix} \delta_x \\ \delta_y \\ \delta_z \\ \phi_x \\ \phi_y \\ \phi_z \end{bmatrix} \tag{2}$$

Where:

$$K = \begin{bmatrix} \frac{A_j E_j}{L_j} & 0 & 0 & 0 & 0 & 0 \\ 0 & \frac{12E_jI_{zj}}{L_j^3} & 0 & 0 & 0 & \frac{6E_jI_{zj}}{L_j^2} \\ 0 & 0 & \frac{12E_jI_{yj}}{L_j^3} & 0 & -\frac{6E_jI_{yj}}{L_j^2} & 0 \\ 0 & 0 & 0 & \frac{G_jJ_j}{L_j} & 0 & 0 \\ 0 & 0 & -\frac{6E_jI_{yj}}{L_j^2} & 0 & \frac{4E_jI_{yj}}{L_j} & 0 \\ 0 & \frac{6E_jI_{zj}}{L_j^2} & 0 & 0 & 0 & \frac{4E_jI_{zj}}{L_j} \end{bmatrix} \tag{3}$$

and E_j and G_j are the modulus of elasticity and the shear modulus of element j respectively; L_j is the beam length, I_{yj}, I_{zj} are the moments of areas about the y and z axes, respectively, J_j is the Saint-Venant torsion constant and A_i is the cross-sectional area. The stiffness analysis enables to obtain the stiffness matrix K for a specific robotic structure at a given configuration. The compliance matrix C can be calculated as the inverse of the stiffness matrix K with deformations due to external loads. The main sources of robot structure compliance are the joints (including their actuators), and the links.

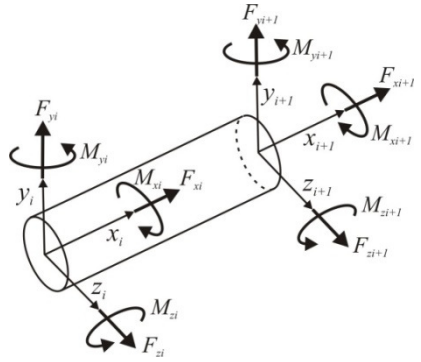

(a)

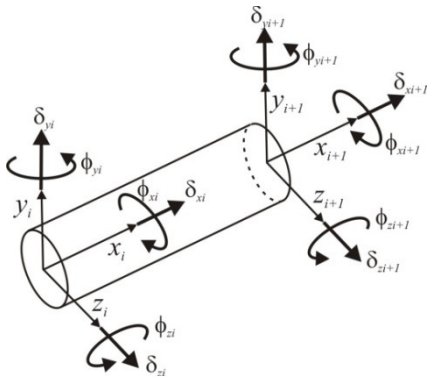

(b)

Figure 1 Forces and moments acting on a link (a); Compliant displacements due to forces and moments acting on the link (b).

Thus, according to the main compliance sources, several methods stiffness analysis have been proposed. One can organize the available methods into the following three groups [5]:

- Methods using lumped parameters; These methods can be divided into two main subgroups according to the used solving methods, namely those using the kinematic and dynamic forces distribution [9;15] and those using the Jacobian matrix [2;6-8;10-15].
- Methods using the Matrix Structural Analysis - MSA [5;16-20];
- Methods using the Finite Element Analysis – FEA [21;22].

It is noteworthy that each method has advantages and disadvantages and the choice of which to use will depend on the required accuracy of the results as well as the amount of computational time that can be considered as acceptable. Additionally, the choice of a specific formulation can also depend on the specific robotic architecture under investigation. In fact, some formulations require close-form kinematics equations that might be not straightforward as for example for some parallel robot architectures.

2.1 STIFFNESS MODEL USING LUMPED PARAMETERS

In general, Lumped parameter model (or lumped component model or lumped element model) is used to simplify the description of a physical system by using discrete entities that are equal or proportional to some average value of the corresponding distributed characteristics . The use of lumped parameters requires some assumptions. For the stiffness model for robotics in general the simplifying assumptions are that all links are rigid bodies with concentrated mass andthe interactions between rigid bodies take place via joints, springs and dampers and, the forces are concentrated. In the following two modeling methods are presented by using lumped parameters: namely, the method that uses the Jacobian matrix and the method that uses the kinematic and forces distribution.

2.1.1 Stiffness Models Using Jacobian Matrix

The Jacobian matrix methods have been studied by several authors as for example in [2;6-8;10-14].

These methods usually take into account only the joints as main compliance source. For a structure with n generalized coordinates and m operational coordinates the torque τ_i, that is transmitted through the *i-th* joint can be related to the corresponding joint small deflections Δq_i by a linear approximation given as [2]:

$$\tau_i = k_i \cdot \Delta q_i \tag{4}$$

where k_i is called the joint stiffness constant (or lumped stiffness parameter). Equation (4) can be written in matrix form for the n generalized coordinates as

$$\boldsymbol{\tau} = K_d \cdot \Delta \boldsymbol{q} \tag{5}$$

where $\boldsymbol{\tau} = [\tau_1, \tau_2, ..., \tau_n]^t$, $\Delta \boldsymbol{q} = [\Delta q_1, \Delta q_2, ..., \Delta q_n]^t$ and $K_d = diag[k_1, k_2, ..., k_n]$ a n x n diagonal matrix.

The vector of joint compliant displacements $\Delta \boldsymbol{q}$ are related to the end-effector compliant displacements $\Delta \boldsymbol{x} = [\delta_x \ \delta_y \ \delta_z \ \phi_x \ \phi_y \ \phi_z]$, though the Jacobian matrix J given by:

$$\Delta \boldsymbol{x} = J \cdot \Delta \boldsymbol{q} \tag{6}$$

The generalized forces $\boldsymbol{F} = [F_x \ F_y \ F_z \ M_x \ M_y \ M_z]^t$ that are applied at the end-effector, , are related to joint reaction forces by the transposed Jacobian matrix of a robotic serial structure in the form:

$$\boldsymbol{\tau} = J^t \cdot \boldsymbol{F} \tag{7}$$

From Equations (4) to (7) one can obtain:

$$\Delta \boldsymbol{x} = C \cdot \boldsymbol{F} \tag{8}$$

where $C = JK_d^{-1}J^t$ is the compliance matrix of the structure. When considering only the joint compliance the stiffness matrix K_s for serial robots can be obtained as:

$$K_s = C^{-1} = J^{-t} \cdot K_d \cdot J^{-1} \tag{9}$$

The compliant displacements due to links were addressed, for example by Komatsu et al. [10-12] in a study on serial robots. The flexibility for a serial structure, according to Yoon et al. [13-14] and Komatsu et al. [10-12] can be obtained using the Jacobian matrix by considering the structure composed of several deformable joints and deformable segments C_{li} where the joints flexibility are represented by C_{joint} and the generalized coordinates are the angles θ_i ($i = 1,..., n$).

From those proposed method the segments and joints compliant displacements can be obtained as:

$$\begin{aligned} C_T &= J_e(\theta, e)\, C_e\, J_e^T(\theta, e) \\ C_e &= diag(C_{e1}\ C_{e2}\ \dots\ C_{en}) \end{aligned} \tag{10}$$

where C_T is the compliance matrix of the end-effector, θ the angle of the joint, $J_e(\theta,e)$ are the Jacobian matrices for each joint and each elastic deformation, C_e is the compliance matrix which is defined by the structural characteristics of all elements, C_{ej} ($j = 1, \dots, n$) is the compliance matrix of each element. For comparison purposes the effect of compliance links and joints can be considered separately by means of equations (4) to (8). In particular, the effect due to compliance links can be computed by means of the following relations:

$$\begin{aligned} C_l &= J_l K_l^{-1} J_l^t \\ K_l &= diag(k_1, k_2, \dots, k_n) \end{aligned} \tag{11}$$

where J_l is the Jacobian Matrix that is obtained as function of k_i ($i = 1, \dots, n$) are the link lumped stiffness parameters.

The amount due to joint compliance can be computed as:

$$\begin{aligned} C_{art} &= J_{art}\, K_{art}^{-1} J_{art}^t \\ K_{art} &= diag(k_{a1}, k_{a2}, \dots, k_{an}) \end{aligned} \tag{12}$$

where J_{art} is the Jacobian Matrix of serial robotic structure and k_{ai} ($i = 1,...,n$) are the joint lumped stiffness parameters. Considering (11) and (12) one can rewrite (10) as:

$$C_T = C_l + C_{art} \tag{13}$$

Yoon et al. [13-14] generalized the proposed method by Komatsu et al. [10-12] when considering also parallel robot structures. In this case, the compliance matrix of parallel manipulators is considered as composed by those of n serial

manipulators, where the point O is the origin (fixed platform) and a point P is the tip position of each limb (serial manipulator). Thus, the tip compliance matrix C_p, of parallel manipulator is given by:

$$C_p^{-1} = C_{s1}^{-1} + C_{s2}^{-1} + \cdots + C_{sn}^{-1} \tag{14}$$

where C_{si} (i = *1,..., n*) is the compliance matrix of each serial manipulator obtained by Eq. (13). The mobile platform and fixed platform are considered as rigid bodies.

2.1.2 Formulation proposed by Tsai

The formulation proposed by Tsai in [2] can be considered equivalent to the model proposed by Komatsu et al. [10-12] when the links are rigid and taking into account only the compliance of joints. Thus, in this case, the calculation of compliance matrix for a serial robot structure can be obtained as:

$$C = J\,K^{-1}J^t$$
$$K = diag(k_1, k_2, \ldots, k_n) \tag{15}$$

where $J = J_{art}$, $K = K_{art}$ are given by (12) and k_i=k_{ai} (i = *1, ..., n*) are the joint lumped stiffness parameters.

Tsai [2] assumes that, similar to serial manipulators, the links are perfectly rigid and he considers only the compliance of joints to obtain the stiffness matrix of a parallel manipulator.

In the case of parallel manipulators some joints are actuated and others are passive. Thus, it is not possible to obtain an independent function between the operational coordinates and generalized coordinates in the form:

$$\boldsymbol{f}(\boldsymbol{x}, \boldsymbol{q}) = 0 \tag{16}$$

where $\boldsymbol{f}$ is a implicit function of the joint coordinates $\boldsymbol{q}$ and the end-effector coordinates $\boldsymbol{x}$, and $\boldsymbol{0}$ is a zeroes vector.

In this case, the joint compliant displacements $\boldsymbol{\Delta q}$ are related with the end-effector compliant displacements $\boldsymbol{\Delta x}$ given by:

$$J_x \boldsymbol{\Delta x} - J_q \boldsymbol{\Delta q} = 0 \tag{17}$$

where

$$J_x = \partial \boldsymbol{f}\,(\boldsymbol{x}, \boldsymbol{q})/\partial \boldsymbol{x}$$
$$J_q = -\partial \boldsymbol{f}\,(\boldsymbol{x}, \boldsymbol{q}) \,/\, \partial \boldsymbol{q} \tag{18}$$

From (17) one can write

$$\boldsymbol{\Delta q} = J_p \cdot \boldsymbol{\Delta x} \tag{19}$$

where $J_p = J_q^{-1} J_x$ is the Jacobian of a parallel manipulator.

The relation between the torque and compliant displacements is given by:

$$\boldsymbol{\tau} = K_d\, J_p\, \boldsymbol{\Delta x} \tag{20}$$

The relation between the torque, $\boldsymbol{\tau}$, in the joints and the forces, $\boldsymbol{F}$, at the mobile platform, is given by:

$$\boldsymbol{F} = J_p{}^t\, \boldsymbol{\tau} \tag{21}$$

Substituting (20) int. (21) one can obtain:

$$\boldsymbol{F} = J_p{}^t\, K_d\, J_p\, \boldsymbol{\Delta x} \tag{22}$$

or

$$\boldsymbol{F} = K_p\, \boldsymbol{\Delta x} \tag{23}$$

where $K_p = J_p{}^T\, K_d\, J_p$ is the stiffness matrix for parallel manipulators.

2.1.3 Model using the kinematic and dynamic forces distribution

This method is based on the computation and composition of 3 matrices as suggested in [9;15;23]. In this case the stiffness of a robot can be given by the stiffness of its components that are described by means of a suitable model of elastic response of those components. A suitable model can refer to lumped stiffness parameters for each component that can be identified by means of suitable linear and torsion springs and using the lumped stiffness model as in [9;15;23;25]. The stiffness matrix can be obtained numerically by defining an appropriate robot model, which takes into account the lumped stiffness model of the links and active joints. The method is also called as *Component Matrix Formulation*. The 3 matrices to be computed are *A*, *B*, *D*. The first matrix *A* gives the wrenches $\boldsymbol{\tau_1}, \ldots, \boldsymbol{\tau_n}$ (n = numbers of components) acting on each component of the robotic system when a wrench $\boldsymbol{\tau}$ acts on its end-effector in the form:

$$\boldsymbol{\tau_L} = A \cdot \boldsymbol{\tau} \tag{24}$$

with $\boldsymbol{\tau}_L = (\boldsymbol{\tau}_{L1}, \ldots, \boldsymbol{\tau}_{Ln})^t$. Therefore, matrix $\boldsymbol{A}$ is a *6n x 6* matrix. The second matrix *B* gives the compliant displacements on the components when the wrenches $\boldsymbol{\tau}_L$ acts on the components and it can be expressed in the form:

$$\boldsymbol{\Delta x}_L = B \cdot \boldsymbol{\tau_L} \tag{25}$$

where $\boldsymbol{\Delta x_L} = (\boldsymbol{\Delta x_{L1}}, \ldots, \boldsymbol{\Delta x_{Ln}})^t$ is a vector of the compliant displacements occurring to all the components of the architecture. Since $\boldsymbol{\Delta x_{L1}}, \ldots, \boldsymbol{\Delta x_{Ln}}$ are n vectors 6 x 1, $\boldsymbol{\Delta x_L}$ is *6n x 1* and the matrix *B* is *6n x 6n* matrix. If one writes $\boldsymbol{\Delta x_{Li}} = B_i\, \boldsymbol{\tau}_{Li}$ with (i=*1,... , n)* then the matrix *B* can be written as:

$$B = \begin{bmatrix} B_1 & 0 & 0 & 0 \\ 0 & \ldots & 0 & 0 \\ 0 & 0 & \ldots & 0 \\ 0 & 0 & 0 & B_n \end{bmatrix} \tag{26}$$

The third matrix *D* is a *6 x 6n* matrix that gives the compliant displacements occurring to the end-effector because of the compliant displacements on each component and it can be formulated in the form:

$$\boldsymbol{\Delta x} = D \cdot \boldsymbol{\Delta x}_L \tag{27}$$

Equation (27) can be obtained by analyzing the kinematics of the manipulator and considering the variation of its kinematic variables due to the deformations and compliant displacements in the legs. Considering (24) to (27):

$$K = (D\,B\,A)^{-1} \tag{28}$$

This approach can require the computation of huge matrices if the number of components n is very high. Moreover, it is necessary to compute the inverse of these matrices that can give numerical problems and can increase significantly the computation time. In some cases it is possible to limit the matrices to a size 6x6 by considering subcomponents of the robotic system instead of single components.

In this case this approach can be convenient for the computation of the stiffness matrix even for complex parallel or serial architectures as proposed in [9;23;24] for humanoid robots and parallel manipulators. However, special care has to be addressed in a proper choice of the subcomponents in order to getsquare invertible matrices. Thus, the stiffness matrix *K* can be computed as (28) that is a way to generalize the Jacobian formulation for clearly marking the dependencies with the 3 main aspects that influence the entries of the Cartesian stiffness matrix in equations (24) to (27).

2.2 STIFFNESS MODEL USING MSA

In this section the *Matrix Structural Analysis* (*MSA*) method, also known as the *displacement method* or *direct stiffness method* (*DSM*) is presented. Structural analysis methods break up a complex system into its component parts, making it a system of discrete structural elements with simple elastic and dynamic properties that can be readily expressed in a matrix form. Since a robotic system is made up of links and joints, this method makes it easy to determine the structure's stiffness matrix. Discrete structures are composed of elements that are joined to each other by connecting nodes. When such a structure is loaded, each node suffers translations and/or rotations, which depend on the structure's configuration and boundary conditions. The nodal displacement can be determined from a complete analysis of the structure. The matrices representing the links and joints are considered building blocks, which, when fitted together according to a set of rules derived from the theory of elasticity, provide the static and dynamic properties of the whole structure [16].

2.2.1. Stiffness of joints and links

The stiffness of a joint can be given by [19;20]:

$$K_{joint} = \begin{bmatrix} K_c & -K_c \\ -K_c & K_c \end{bmatrix} \tag{29}$$

where $K_c = diag(k_{lx}, k_{ly}, k_{lz}, k_{ax}, k_{ay}, k_{az})$; k_{lx}, k_{ly}, k_{lz} are the coefficients for translational stiffness and k_{ax}, k_{ay}, k_{az} the coefficients for rotational stiffness about the *x*, *y* and *z* Cartesian axes. The stiffness matrix of a *j-th* three-dimensional straight bar (beam or link) with a uniform cross-sectional area can be expressed as:

$$K_j = \begin{bmatrix} K_{bj} & -K_{bj} \\ -K_{bj} & K_{bj} \end{bmatrix} \tag{30}$$

where K_{bj} is given by the matrix *K* from Eq. (3).

The application of MSA requires writing the stiffness matrices of all elements in the same reference frame before to assemble the stiffness matrix of the structure. The transformation matrix, $T_j$can be obtained by linear algebra [4]. Thus, the stiffness matrix of the elements in a common reference frame (elementary stiffness matrix), for segments, k_j^e, and for joints $k_{jo\,\mathrm{int}}^e$ can be expressed as:

$$K_j^e = T_j\, K_j\, T_j^t \tag{31}$$

$$K_{joint}^e = T_j\, K_{joint}\, T_j^t \tag{32}$$

After obtaining the stiffness matrix of links and joints in a common reference frame, the stiffness matrix of a structure can be determined using MSA. Based on how the structure elements are connected through their nodes, it is possible to define a connectivity matrix. Since segment and joint stiffness are known, the global stiffness matrix can be obtained by a superposition procedure described in [27].

The methodology described to obtain the global stiffness matrix considers the structure as free or, in other words, without motion constraints that make this matrix be singular. By applying boundary conditions when the displacements are known, a new invertible stiffness matrix *K* can be obtained, and the compliant displacement can then be computed as:

$$\Delta \boldsymbol{x} = K^{-1}\, \boldsymbol{F} \tag{33}$$

where $\Delta \boldsymbol{x}$ are the compliant displacements and $\boldsymbol{F}$ are the applied external wrenches. Methods based on matrix structural analysis are simple and easy to implement computationally. For example the authors of [25] used this approach to derive the stiffness matrix of each element of a Stewart platform and then their assemble the individual elements into the Stewart platform stiffness matrix. This approach is also used in [26] to obtain the stiffness model of a machine frame considered as a substructure. The superposition principle is used to obtain the stiffness model of the machine structure as a whole. Gonçalves [19] applied the MSA method for robotic systems and demonstrated the validity of this method by experimental tests in a structure composed by two links and one spherical joint simulating a closed kinematic chain. The errors between values obtained using MSA and experimental tests were small. Gonçalves and Carvalho [20] applied the MSA method in a 6-RSS parallel structure and once obtained errors compared with experimental results they considered acceptable the results in [27]. They applied the method to obtain the singularities of parallel robots too [18].

2.3 STIFFNESS MODEL USING FEA

Stiffness analysis of structures, through analytical methods, almost always produces equations that are hard to solve or, in some cases, impossible to be solved. In that case, it is necessary to implement a numerical approximation of calculation, so one can obtain results as close as possible to real. The Finite Element Analysis (FEA) method is a numerical analysis technique that is used to obtain approximate solutions to problems governed by differential equations. Although the method was first developed for static analysis of structural systems, it has been used to study a great variety of engineering problems, in the domains such as solid and fluid mechanics, heat transfer and electromagnetism [28]. The FEA method can then be defined as a process of discretization of the problem, which changes the infinite-dimensional condition of the problem to a finite-dimensional condition, limiting the number of unknowns. The method consists in dividing the domain over which the problem is studied in multiple linked regions, named elements.

Each element then is limited by points called nodes, and the group of elements with their nodes is called mesh. After the definition of elements and their respective nodes, inside each element one admits approximate solutions expressed by interpolation functions. It can be also imposed to conditions guarantee a continuous solution in the nodes shared by various elements. The problem's unknowns, called dof, become the values of the field variables in the nodal points, and the number of these unknowns (now finite) is called number of degrees of freedom of the model. Depending on the nature of the problem, after the discretization, the governing mathematical model results on a finite number of ordinary differential equations or algebraic equations, where the numerical solution enables to evaluate the nodal unknowns. Once these unknowns are obtained, the values of the field variables inside the elements can be evaluated using interpolation functions [27]. Many authors have been using FEA for stiffness analysis of robotic structures. Bouzgarrou et al. [21] worked out a stiffness study of the parallel robot 3TR1 by using finite elements that are coupled to a CAD model. Clinton et al. [25] studied the stiffness of the Gough-Stewart platform with all elements subject only to traction and compression solicitations. Each element is studied individually and then assembled in order to study the structure as a whole. In Dong et al. [17] a study using FEA is elaborated in order to determine the stiffness model of a parallel structure that has flexure hinge joints. Zhou et al. [29] used FEA for the modeling of the parallel manipulator 3-PRS. The moving platform is modeled by triangular plate elements and the legs by beam spatial element. The flexibility of the joints is considered by the introduction of virtual springs to the FEA model. As the joints parameters are not known, the FEA numerical model is adjusted through experimental tests according to the frequency response functions. Deblaise [5;30] used FEA modeling to compare the results obtained using the MSA. This study was applied in the modeling of a Delta parallel robot. In the paper, a model considering only the flexibility of the segments not provided consistent results with experiments.
Corradine et al. [22] used FEA to model the H4 robot. Besides the modeling of segments, the spherical and rotational joints were modeled introducing "displacement relaxation" in the FEA model, which allows, for the spherical joints, that all flexible translation displacements between the segments are the same, but not the rotations. For rotational joints all movements, excluding the rotation axis, should be the same. When comparing the results of the FEA model with those from experiments, they were close to each other. Kobel and Clavel [31] developed a reduced size with large workspace robot, named ΦR, for micro manipulation and assembling, using finite elements to evaluate the static behavior of the structure. The bearings in the structure were idealized using 6 springs between inner and outer rings of each revolute joint in order to account for the influence of such bearings. Aginaga et al. [32] presented an analytical method to calculate the stiffness matrix for parallel structures, applying it to the 6-RUS structure.
The finite elements method was then applied to a specific component of the structure, due to its complex geometry, in order to calculate the stiffness indexes of such component. Rezaei et al. [33] held the stiffness analysis of a spatial parallel 3-PSP structure considering the moving platform as flexible. The finite element method was then used as comparison parameter. Gonçalves and Carvalho [20] applied the FEA method to compare with results obtained by MSA method in a 6-RSS parallel structure. In general the FEA method is used to validate analytical models [5; 34-37] and or experimental results [5; 20-22; 29; 33] or even for optimization of structures and parts of structures [32; 38]. The biggest advantage of using the FEA method is the utilization of the mechanical design of structure's project with no simplification, considering its full geometry. For robotic structures with irregular geometry, like industrial serial robots and parallel robotic structures that are subject to not only axial loads, like the Gough-Stewart platform, the use of the FEA method make the stiffness analysis for the robotic structure fairly easy . The disadvantage of the FEA method, when it involves commercial software for analysis, is that it requires great computational efforts, because, since stiffness depends on positions, it is necessary, for each specific position, to build a finite element model [26]. Other advantages of FEA are: elements of different shapes and sizes can be associated to discrete domains of complex geometry; the division of the continuous domain in regions makes the modeling of problems with non-homogeneous domains easier, where physical properties vary; and the method can completely formulated with matrices, making its computational implementation easier. The disadvantages of the method are the uncertainties inherent of the FEA modeling resultant of simplifications of the physical model such as: not considering some physical effects like non-linearity, hysteresis, damping; discretization error; inaccurate values of physical and/or geometrical parameters (elasticity models, density); difficulty in modeling localized effects such as screwed and errors derived of the process of numerical resolutions. A further key disadvantage is that a FEA meshing and calculation should be done for each single configuration of a robot structure.

3 CASES OF STUDY

In this section two cases of study are reported for the main techniques to obtain the compliant displacements. A first case of study refers to a 2 dof planar serial structure considering the compliance of links and joints. The second case of study deals with a prototype of a 6-RSS parallel structure. Finally experimental results are presented for stiffness evaluation. In both cases of study compliant displacements are used as local stiffness performance indices, as also proposed in [5].
It is to note that usually active joints are driven by an actuator through a multiple-stage speed reducer along with several drive shafts. This effect has been considered as combined into an equivalent joint stiffness.

Examples of calculation of the mechanical transmission mechanisms can be found in [1].

3.1 NUMERICAL SIMULATIONS APPLIED ON A SERIAL STRUCTURE

3.1.1 Methods based on Jacobian matrix

Figure 2 shows the sketch of a 2 dof planar serial robotic manipulator with the inertial reference frame $O_0\ x_0\ y_0$, an reference frame $Ax_1\ y_1$ fixed on the first link with length L_1 and $Bx_2\ y_2$ fixed on link with length L_2. The angles θ_1 and θ_2 are the generalized coordinates (joints).

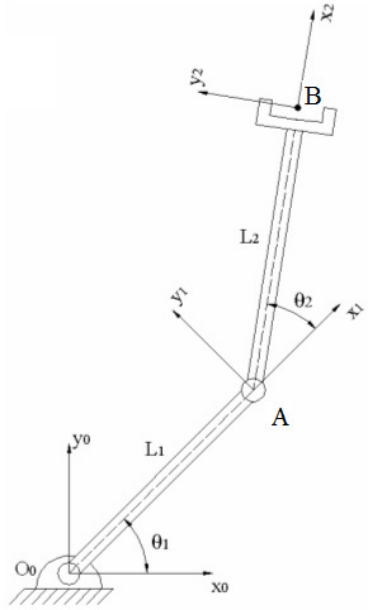

Figure 2 A 2 dof planar serial manipulator.

3.1.2 Applying the methods proposed by Yoon et al. [13-14] and Komatsu et al. [10-12]

Considering the compliant displacements for the scheme in Fig. 3, one can write the coordinates of points A and B as:

$$\begin{aligned} x_A &= L_1 \cos(\theta_1) - \delta_1 \sin(\theta_1) \\ y_A &= L_1 \sin(\theta_1) + \delta_1 \cos(\theta_1) \\ x_B &= x_A + L_2 \cos(\theta_1 + \phi_1 + \theta_2) - \delta_2 \sin(\theta_1 + \phi_1 + \theta_2) \\ y_B &= y_A + L_2 \sin(\theta_1 + \phi_1 + \theta_2) - \delta_2 \cos(\theta_1 + \phi_1 + \theta_2) \end{aligned} \tag{34}$$

From Fig. 3(a) forces F_x and F_y applied at point B can be decomposed in the normal direction of links as, Fig. 3(b):

$$\begin{aligned} F_1 &= F_x\ sen(\theta_2) + F_y \cos(\theta_2) \\ F_2 &= F_y \\ M_1 &= L_2\ F_y \\ M_2 &= 0 \end{aligned} \tag{35}$$

where F_1 and F_2 are the forces obtained from F_x and F_y applied at A and B, perpendicular to links 1 and 2, respectively. M_1 and M_2 are the moments applied at A and B, respectively, due to the force F_y. Applying the elastic differential linear equation [39] for a cantilever, the linear compliant displacements, δ_1 and δ_2, and angular compliant displacements ϕ_1, ϕ_2, due to the forces F_1, F_2, M_1 and M_2, are calculated by:

$$\begin{aligned} \delta_1 &= \frac{L_1^3}{3E_1I_1} F_1 + \frac{L_1^2}{2E_1I_1} M_1 \\ \delta_2 &= \frac{L_2^3}{3E_2I_2} F_2 + \frac{L_2^2}{2E_2I_2} M_2 \\ \phi_1 &= \frac{L_1^2}{2E_1I_1} F_1 + \frac{L_1}{E_1I_1} M_1 \\ \phi_2 &= \frac{L_2^2}{2E_2I_2} F_2 + \frac{L_2}{E_2I_2} M_2 \end{aligned} \tag{36}$$

Substituting equation (35) into (36), and after mathematical manipulations, one can write the angular compliant displacement as [10-12]:

$$\begin{aligned} \phi_1 &= \frac{3}{2L_1} \delta_1 + \frac{3E_2I_2L_1L_2}{2E_1I_1(2L_2^3 + 3L_2^2)} \delta_2 \\ \phi_2 &= \frac{3(L_2^2 + 2L_2)}{2L_2^3 + 3L_2^2} \delta_2 \end{aligned} \tag{37}$$

From Figures 6 and 7, the configuration of end-effector, point B, considering the kinematics model and compliant displacements is given by $\boldsymbol{f_T}$:

$$\boldsymbol{f_T} = \begin{Bmatrix} x_B \\ y_B \\ \theta_T \end{Bmatrix} \tag{38}$$

where

$$\theta_T = \theta_1 + \phi_1 + \theta_2 + \phi_2 \tag{39}$$

The calculation of the links deformation is performed by Eq. (11) applied to the 2 dof serial manipulator:

$$\begin{aligned} C_l &= J_l K_l^{-1} J_l^t \\ K_l &= diag(k_1, k_2) \end{aligned} \tag{40}$$

As J_l is the Jacobian matrix it can be obtained by differentiating Eq. (38) related to deformations $\boldsymbol{x_l}$ as:

$$x_l = \begin{bmatrix} \delta_1 \\ \delta_2 \end{bmatrix} \quad ; \quad J_l = \frac{\partial \boldsymbol{f_T}}{\partial \boldsymbol{x_l}} \tag{41}$$

Then the Jacobian matrix can be obtained as:

$$J_l = \begin{bmatrix} Jl_{11} & Jl_{12} \\ Jl_{21} & J_{22} \\ Jl_{31} & Jl_{32} \end{bmatrix} \tag{42}$$

where

$$\begin{aligned} Jl_{11} &= -sin(\theta_1) - \frac{3L_2 sin(\theta_{aux})}{2L_1} - \frac{3\delta_2 cos(\theta_{aux})}{2L_1} \\ Jl_{12} &= -\frac{3E_2I_2L_1 sin(\theta_{aux})}{4L_2E_1I_1} - sin(\theta_{aux}) - \frac{3\delta_2E_2I_2L_1 cos(\theta_{aux})}{4L_2^2E_1I_1} \\ Jl_{21} &= cos(\theta_1) + \frac{3L_2 cos(\theta_{aux})}{2L_1} - \frac{3\delta_2 sin(\theta_{aux})}{2L_1} \\ Jl_{22} &= \frac{3E_2I_2L_1 cos(\theta_{aux})}{4L_2E_1I_1} + cos(\theta_{aux}) - \frac{3\delta_2E_2I_2L_1 sin(\theta_{aux})}{4L_2^2E_1I_1} \\ Jl_{31} &= \frac{3}{2L_1} \\ Jl_{32} &= \frac{3E_2I_2L_1}{4L_2^2E_1I_1} + \frac{3}{2L_2} \end{aligned} \tag{43}$$

and

$$\theta_{aux} = \theta_1 + \frac{3\delta_1}{2L_1} + \frac{3\delta_2E_2I_2L_1}{4L_2^2E_1I_1} + \theta_2 \tag{44}$$

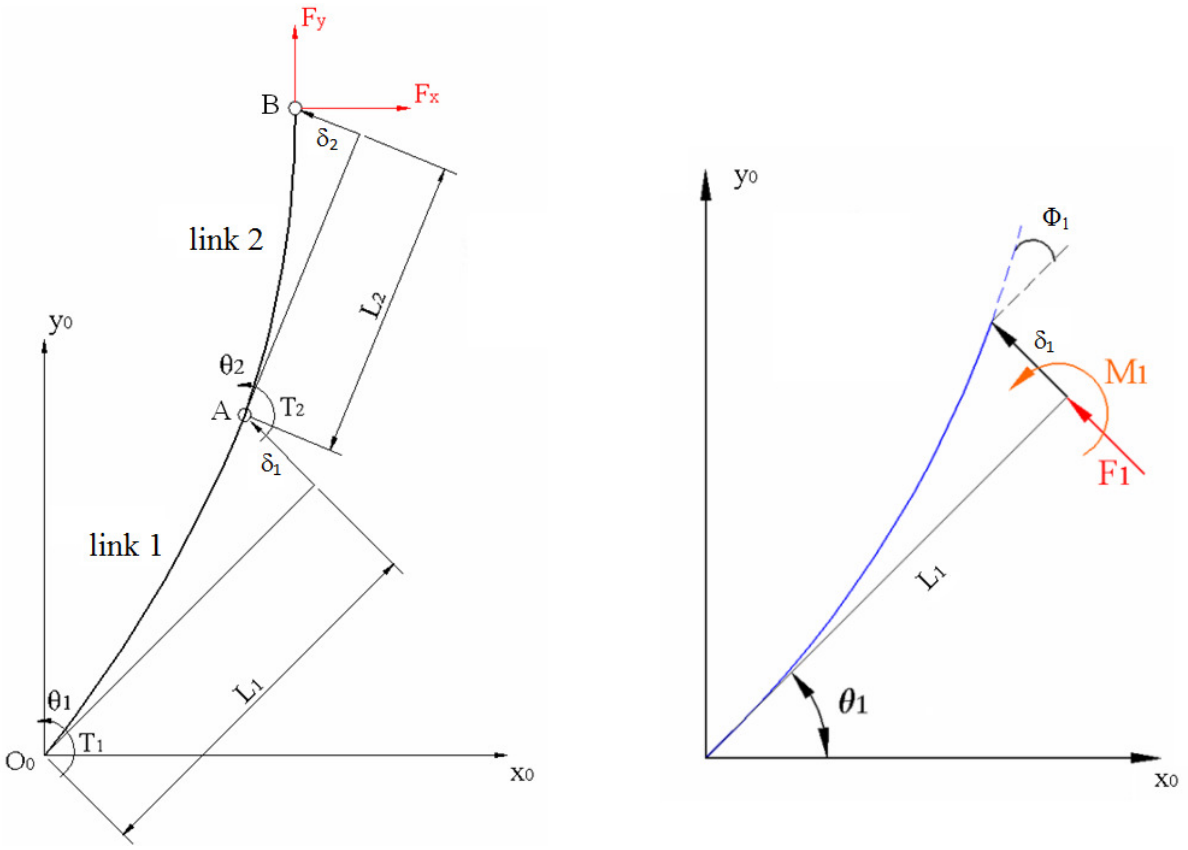

Figure 3 Model for application of the methodology of Komatsu et al. [10-12] (a); Linear compliant displacement (δ_l) and angular compliant displacement (ϕ_l) (b).

Furthermore, to obtain the links compliant matrix, Eq. (40), it is necessary to determine the coefficients k_1, k_{12} and k_2, which are the lumped stiffness coefficients of the first link, the coupling between the links, and the second link, respectively. The calculation of these coefficients is accomplished by using the equation of strain energy for bending [39], Eq. (46), and the strain energy of the system related to δ_1 and δ_2, Eq. (45) [10-12]:

$$U = \frac{(k_1\delta_1^2 + k_{12}\delta_1\delta_2 + k_2\delta_2^2)}{2} \tag{45}$$

$$U = \frac{1}{2E_1I_1}\int_0^{l_1}(F_1x_1 + M_1)^2dx_1 + \frac{1}{2E_2I_2}\int_0^{l_2}(F_2x_2 + M_2)^2dx_2 \tag{46}$$

Solving Equations (45) and (46), and after mathematical simplifications, it can be obtained as:

$$k_1 = \frac{3E_1I_1}{L_1^3} \tag{47}$$

$$k_{12} = 0 \tag{48}$$

$$k_2 = \frac{9L_1L_2E_2^2I_2^2(4L_1 - 4L_1\cos\theta_2 + L_2) + 12E_1I_1E_2I_2L_2^3}{4E_1I_1L_2^6} \tag{49}$$

Thus, one can obtain C_l by replacing Eqs. (47) to (49) and (36) into Eq. (42).

The calculation of the compliance matrix due to joints is obtained by applying Eq. (12) to the model of Fig. 6.

$$C_{art} = J_{art}\,k_{art}^{-1}\,J_{art}^{T}$$
$$k_{art} = diag(k_{a1}, k_{a2}) \tag{50}$$

The calculation of the Jacobian matrix due to joints, J_{art}, is given by differentiating Eq. (38) related to $\boldsymbol{x}_{art}$ as:

$$J_{art} = \frac{\partial \boldsymbol{f}_T}{\partial \boldsymbol{x}_{art}} \;;\; \boldsymbol{x}_{art} = \begin{Bmatrix}\theta_1\\ \theta_2\end{Bmatrix} \tag{51}$$

where θ_{aux} is given by Eq. (44). The values of the stiffness constants k_{a1} and k_{a2} can be done by experimental data or from catalogs. Thus, it is possible, from Eqs. (51) and (52), to obtain the compliance matrix due to the joints.

$$J_{art} = \begin{bmatrix} -L_1sin(\theta_1) - \delta_1cos(\theta_1) - L_2sin(\theta_{aux}) - \delta_2cos(\theta_{aux}) & -L_2sin(\theta_{aux}) - \delta_2cos(\theta_{aux}) \\ L_1cos(\theta_1) - \delta_1sin(\theta_1) + L_2cos(\theta_{aux}) - \delta_2sin(\theta_{aux}) & L_2cos(\theta_{aux}) - \delta_2sin(\theta_{aux}) \\ 1 & 1 \end{bmatrix} \tag{52}$$

Finally, the compliance matrix of the 2 dof serial robotic manipulator is given by:

$$C_T = C_l + C_{art} \tag{53}$$

The stiffness matrix can be calculated as the inverse of C_T.

3.1.3 Matrix Structural Analysis – MSA method

In this section, the stiffness matrix is obtained using the *Matrix Structural Analysis* (*MSA*). Figure 4 illustrates a model for application of the MSA methodology.

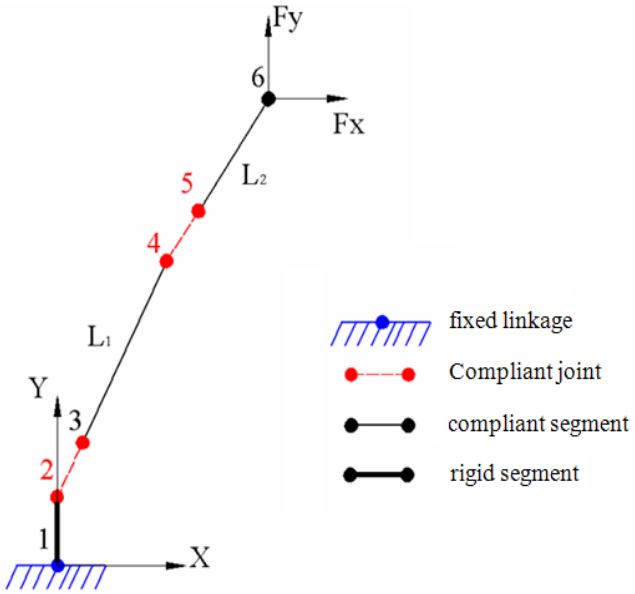

Figure 4 Nodes in the 2 dof serial manipulator for applying the MSA method.

In Figure 4, points 1 to 6 are the nodes, the segment defined by the nodes 1-2 is considered a rigid base and the links defined by the nodes 3-4 and 5-6 are flexible.

The rotational joints are represented by nodes 2-3 and 4-5. It should be emphasized that the nodes which define the rotational joint have the same position. The inertial frame has its origin at node 1. Firstly the stiffness matrices of each element are obtained both for the three segments and two joints. To obtain the stiffness matrix relative to the segments, they are considered as beam elements with circular cross section, neglecting the effects of shear forces that are calculated by Eq. (3). The joint stiffness matrix is given by Eq. (29). In order to obtain the joint compliance matrix the linear stiffness parameters k_{lx}, k_{ly}, k_{lz} and angular stiffness parameters k_{ax}, k_{ay}, k_{az} can be obtained according to the manufacturers' catalog or by experimental tests. Before performing the assembly of the stiffness matrix of the manipulator as a whole the matrices of each element relative to the inertial frame *Oxyz* must be written using the transformation matrix T_j, Eqs. (31) and (32). The nodes coordinates 1 to 6 are obtained by the kinematics model of the robot. The segment defined by nodes 1 and 2, corresponding to the base of the robot, can be considered flexible or not. In this example it is considered as rigid segment. For this, in this element stiffness matrix is considered its modulus of elasticity as 10 times larger than the other segments. From the segments and joints stiffness matrix in relation to the inertial frame can be done the assembly of the stiffness matrix of the whole structure. Since each node has 6 dof, the size of this square matrix is 6n = 36. The assembly of this matrix must conform to the numbering of the nodes shown in Fig. 4. Thus it is possible to establish a connectivity matrix between elements, which indicates, for example, nodes 2 and 3 (forming a rotational joint) have the same linear displacement and angular displacement, except the rotation around the joint axis. Thus, Fig. 4 and Table I, for each node is reported the quantification of dof which represents the number of possible movements.

Table I - Degrees of freedom related to Fig. 4

	Nodes					
Compliant Displacement	**1**	**2**	**3**	**4**	**5**	**6**
Linear compliant displacement on *x* direction (δ_x)	1	7	13	19	25	31
Linear compliant displacement on *y* direction (δ_y)	2	8	14	20	26	32
Linear compliant displacement on *z* direction (δ_z)	3	9	15	21	27	33
Angular compliant displacement around *x* (ϕ_x)	4	10	16	22	28	34
Angular compliant displacement around y (ϕ_y)	5	11	17	23	29	35
Angular compliant displacement aroundz (ϕ_z)	6	12	18	24	30	36

The connectivity matrix can be written as

$$\begin{bmatrix} 1 & 2 & 3 & 4 & 5 & 6 & 7 & 8 & 9 & 10 & 11 & 12 \\ 7 & 8 & 9 & 10 & 11 & 12 & 13 & 14 & 15 & 16 & 17 & 18 \\ 13 & 14 & 15 & 16 & 17 & 18 & 19 & 20 & 21 & 22 & 23 & 24 \\ 19 & 20 & 21 & 22 & 23 & 24 & 25 & 26 & 27 & 28 & 29 & 30 \\ 25 & 26 & 27 & 28 & 29 & 30 & 31 & 32 & 33 & 34 & 35 & 36 \end{bmatrix} \begin{matrix} \rightarrow \text{segment } 1-2 \\ \rightarrow \text{joint } 2-3 \\ \rightarrow \text{segment } 3-4 \\ \rightarrow \text{joint } 4-5 \\ \rightarrow \text{segment } 5-6 \end{matrix} \tag{54}$$

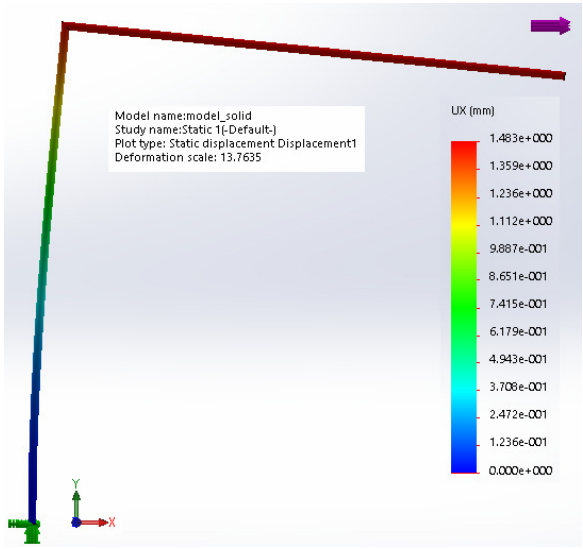

Figure 5 *FEA* model compliant displacements.

The connectivity matrix allows the stiffness matrix assembly of the whole structure. This provides the element position inside the structure stiffness matrix. The obtained matrix is singular because the structure has no restrictions. So, must be applied the boundary condition that, in this case corresponds to a fixed node 1. As in the fixed node all displacements are zero one can eliminate these degrees of freedom of the system (1-6), corresponding to node 1.Thus, the new square matrix is a 30x30 dimensional and is invertible. This procedure is detailed in [27]. In Fig. 4 forces can be applied in all nodes. In this example forces are applied only at node 6, for comparison with other methodologies. Thus, the compliant displacements can be calculated by Eq. (33),where K is a 30x30 matrix and the vector $\boldsymbol{F}$, applied in the nodes 2-6 is a 30x1 vector and the flexible displacement vector $\boldsymbol{\Delta x}$ is a 30x1 vector.

3.1.4 FEA Model -Finite Element Analysis

The example for finite element model and simulation has been carried out by using the commercial software SolidWorks®. The proposed model takes into account only the compliance of links that have modeled as solid body.. Figure 5 presents the model of a 2 dof robotic manipulator at a specific configuration ($\theta_1 = 90^o$ and $\theta_2 = -90^o$).
Elements discretization has been defined by software default. The compliant displacements have been calculated by applying a unit force along x axis.

3.1.5 Comparison and discussion between the results of serial structure

Tables II, III and IV summarize a comparison the methodologies presented by Komatsu et al. and Yoon et al., Tsai, MSA and FEA referring to displacements at point B of 2 dof robotic manipulator configuration that is shown in Fig.3, with: $\theta_1 = 90^o$ and $\theta_2 = -90^o$. Unit force have been applied along the x axis, ($F_x = 1\ N$ and $F_y = 0$). For all models, the links have been considered as made of steel with elastic modulus $E = 2e^{11} N/m^2$ with a length of 0.3 m and circular cross section with a diameter of 0.005 m.

The joints lumped parameters for the models of Komatsu et al., Yoon et al. and Tsai have been set as equal to:

$$k_{a1} = k_{a2} = 1000\ \ N\,m/rad \tag{55}$$

For the joint compliance simulation using the MSA the following values have been considered for numerical simulation:

$$k_{lx} = k_{ly} = k_{lz} = 2e^{11}\ \ N/m$$
$$k_{ax} = k_{ay} = 2e^{11}\ \ N\,m/rad \tag{56}$$
$$k_{az} = 1000\ \ N\,m/rad$$

It has been also assumed $k_{az} = k_{a1} = k_{a2}$.
Table II presents a comparison of results when using only the joints compliance, and segments are rigid. Table III shows the results when considering only the segments flexibility and neglecting the joints flexibility. Table IV presents the results considering both the flexibility of joints and segments.
When considering only the joints flexibility as in Table II, the results using the method of Komatsu et al. and Yoon et al. provide the same results when compared with the model used by Tsai. This is expected because both methods use the calculation of Jacobian matrix. In the procudere using the MSA results are different due to the no knowledge of values corresponding to k_{lx}, k_{ly}, k_{lz}, k_{ax} and k_{ay}. A more close match with the data used by Komatsu et al. and Yoon et al. could be achieved by more accurate matching of the above parameters in the two different models. Considering the model with only the segments flexibility as in Table III, the results are coincident in the methods MSA and FEA and with the methodology of Komatsu et al. and Yoon et al. results are quite similar. By considering joints and segments flexibilities as inTable IV, the results from the procedures of Komatsu et al. and Yoon et al. and MSA are close. Considering only the flexibility of joints as in Table II, the model proposed by Tsai is more convenient since it is derived from the calculation of the Jacobian of the robotic structure. But the calculation of this Jacobian can become complicated when depending on the number of structured and type of structure considered. For example, for a parallel robotic structure the Jacobian matrix is not simple.
When considering only the segments flexibility as in Table III, using the MSA method is more favorable because unlike the methodology used by Komatsu et al. and Yoon et al., it is not necessary to calculate differential equations, it is the case for calculating the Jacobian considering the segments flexibility. As shown by Eqs. (34) to (54) this calculation can be complicated and susceptible to errors. In this example a 2 dof serial robotic manipulator is considered. If the number of dofs is larger, more calculations of differential equations are necessary. Furthermore, the methodology of Komatsu et al. and Yoon et al. requires to calculate the value of the forces acting on each segment, and the computation can be complicated depending on the number of segments and forces and/or moments in the model.
The same comments are valid for the model considering simultaneously the segments and joints flexibilities as forTable IV.

Table II - Results of compliant displacements considering only the joints flexibility

Compliant Displacements	**Methodologies**		
	Komatsu et al. and Yoon et al.	Tsai	MSA
Computational time [s]	0.21	0.01	0.183
δ_x [mm]	0.09	0.09	0.2518
δ_y [mm]	-0.09	-0.09	-0.3249
δ_z [mm]	0	0	0
ϕ_x [rad]	0	0	0
ϕ_y [rad]	0	0	0
ϕ_z [rad]	0	0	-0.0011

Table III - Results of compliant displacements considering only the segments flexibility

Compliant Displacements	**Methodologies**		
	Komatsu et al. and Yoon et al.	MSA	FEA
Computational time [s]	3.095	0.109	3.0
δ_x [mm]	1.4347	1.4668	1.483
δ_y [mm]	-2.1676	-2.2001	-2.198
δ_z [mm]	0	0	0
ϕ_x [rad]	0	0	0
ϕ_y [rad]	0	0	0
ϕ_z [rad]	-0.0073	-0.0073	0

Table IV - Results of compliant displacements considering the joints and segments flexibilities

Compliant Displacements	**Methodologies**	
	Komatsu et al. and Yoon et al.	MSA
Computational time [s]	3.49	0.1818
δ_x [mm]	1.5234	1.5720
δ_y [mm]	-2.2567	-2.3050
δ_z [mm]	0	0
ϕ_x [rad]	0	0
ϕ_y [rad]	0	0
ϕ_z [rad]	-0.0073	-0.0076

3.2 NUMERICAL AND EXPERIMENTAL RESULTS FOR PARALLEL ROBOTS

3.2.1 A 6-RSS parallel structure

The 6-RSS parallel structure is a 6 dof manipulator, which is characterized by a base and a mobile platform, connected by six RS-SS segments, where the R-joint is on the reference frames, two joints by axis. The S-joints on the other extremity of the links are connected at the mobile platform, consisting in a virtual cube where the S-joints are tied on the center of its faces three crossed segments.

Kinematics variables are the input angles α_i (*i=1 to 6*) of the R-joints. The studied structure has the RS-segment and the SS-segment with the same length i.e., $|b_1b_2| = |b_3b_4| = |b_5b_6| = |p_1p_2| = |p_3p_4| = |p_5p_6|$, Fig. 6(a). Figure 6(b) show a prototype built at the Laboratory of Automation and Robotics in Uberlandia,Brazil.Kinematic analysis can be obtained by using a suitable analytical procedure with a vector and matrix formulation as reported in [27].

3.2.2 Stiffness Analysis using the Jacobian matrix

The stiffness matrix of the 6-RSS parallel structure using the Jacobian Matrix can be numerically computed by defining a suitable model of the robot, which takes into account the stiffness properties of each element of the robot. In particular, the lumped stiffness parameters are modeled as linear and torsion springs. A simplified stiffness model of 6-RSS parallel manipulator can be defined as show in Fig. 7. In Figure 7 the spherical and revolute joints are modelled with torsion spring, k_{aij} (*i = 1 to 6 and j=1,2*), and linear springs, k_{lij} (*i = 1 to 6 and j=1,2,3*) represent the forearm and arm. The definition of lumped stiffness parameters for the built prototype 6-RSS is not trivial. Moreover, the Jacobian matrix calculation for parallel structure is not simple. The Jacobian calculation of a "simple model", presented in section 2.1.2, highlights the difficulty of obtaining the stiffness model using the Jacobian matrix, when considering the compliance of joints and links.

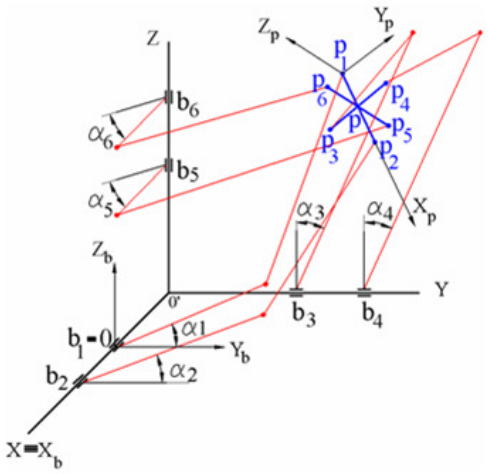

(a)

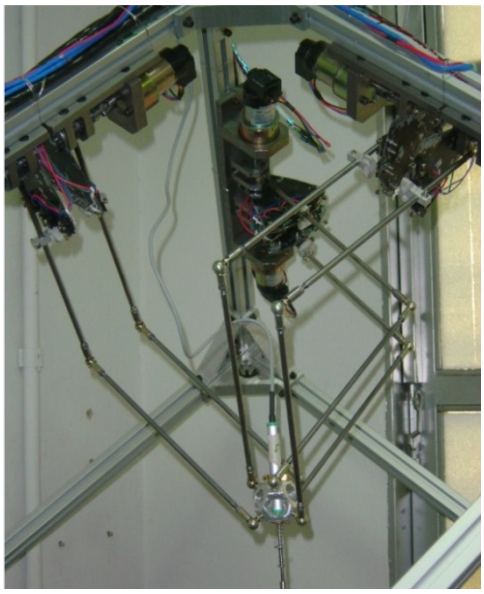

(b)

Figure 6 (a) The 6-RSS parallel structure with generic configuration; (b) The built prototype.

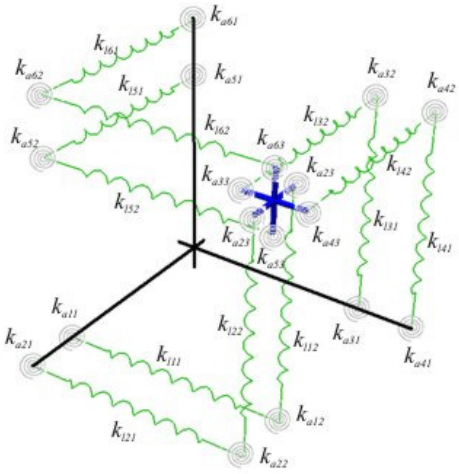

Figure 7 A Stiffness Model for the 6-RSS Parallel Manipulator with lumped stiffness parameters.

3.2.3 Structural Analysis with MSA and FEA methods.

In this section the stiffness model of the 6-RSS parallel structure is presented considering the compliance of links and joints. The arms and forearms are modeled as beams and the stiffness analysis of the structure is carried out according to the elements that are considered in the structure as in Fig. 8. The following parameters were used in the model: length of the arms and forearms equal to *0.3m*; $|b_1b_2| = |b_3b_4| = |b_5b_6| = |p_1p_2| = |p_3p_4| = |p_5p_6| = 0.076m$; the segments are built of steel with ($E = 2 \times 10^{11}$ N/m^2 and $G = 0.8 \times 10^{11}$ N/m^2) the cross-sectional is circular with *0.005m* diameter.

The boundary conditions are given by actuators, that are considered as blocked and, therefore, the forearms can be considered as fixed in the rotational joints (nodes 1, 7, 8, 13, 14 and 19). The external force and torque are applied on node 4, which is the center of the mobile platform. Numerical simulations had been carried out considering both stiffness for links and joints, using translational and rotational stiffness for joints with values in (57) given by:

$$k_{lx} = k_{ly} = k_{lz} = 2e^{11}\ N/m;\ k_{ax} = k_{ay} = k_{az} = 0\ Nm/rad \quad (57)$$

From the nodes that are defined on Fig. 8(b), the structure has 19 nodes with 6 dofs in each node. Thus, the system has 114 dofs with a 18x12 connectivity matrix. The stiffness matrix of the structure after considering the boundary conditions (six fixed rotational joints) becomes a 78x78 matrix. In order to verify the presented analysis using the MSA method, a model was built in FEA using commercial Ansys® software. The used element is a beam type divided in 10 parts. This model does not consider the joint stiffness. Table V provides results that are obtained from the FEA and MSA models. In Table 5 F_e is the external force $F_e = [F_x, F_y, F_z]$ and M_e the external torque $M_e = [M_x, M_y, M_z]$. Results of numerical simulations are presented in Table 5. The results show the soundness of the model also in terms of symmetry of the structure.

One can note that the compliant displacements are the same in the direction of the applied forces when other forces and torques are zero and, if the same effort values are applied, the compliant displacements are equals.

A non-actuated prototype of the 6-RSS was built for experimental tests, Fig. 9. The actuators, which are blocked with bolts and nuts, are used as boundary conditions (nodes 1, 7, 8, 13, 14 and 19), so that the rotational joints can be considered as fixed. Tests were performed with the measurement of compliant displacements in one direction, using a dial indicator. Three different loads $P_1 = 0.9935$ kg, $P_2 = 1.2435$ kg and $P_3 = 1.4915$ kg were applied on the center of the platform, at node 4. The acceleration of gravity is $g = 9.81$ m/s^2. These experimental tests were performed with an initial 6-RSS Parallel Manipulator configuration of $\alpha_1 = \alpha_2 = \alpha_3 = \alpha_4 = \alpha_5 = \alpha_6 = 0°$.

Compliant displacements in the z_b direction, at points 3, 5, 11 and 17, were obtained using a dial indicator with a resolution of 1µm. Statistical analysis was used to determine the required number of measurements of compliant displacements, whose results are listed in Table VI.

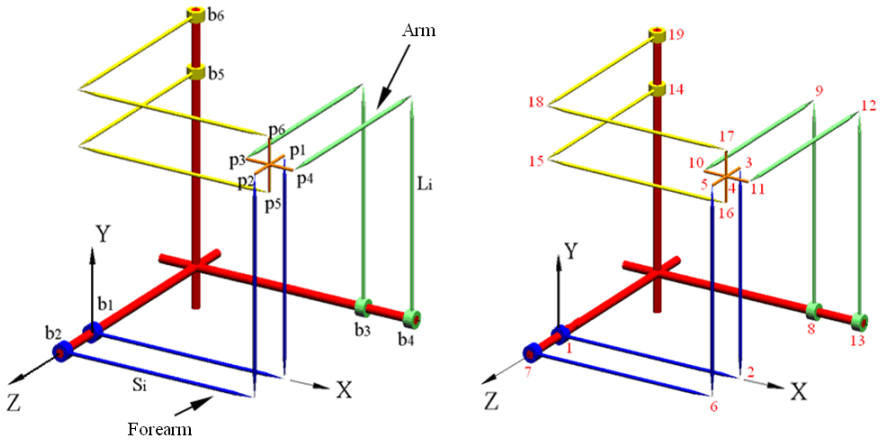

Figure 8 A Stiffness model of a 6-RSS parallel architecture: (a) 3D sketch; (b) Nodal points at joints.

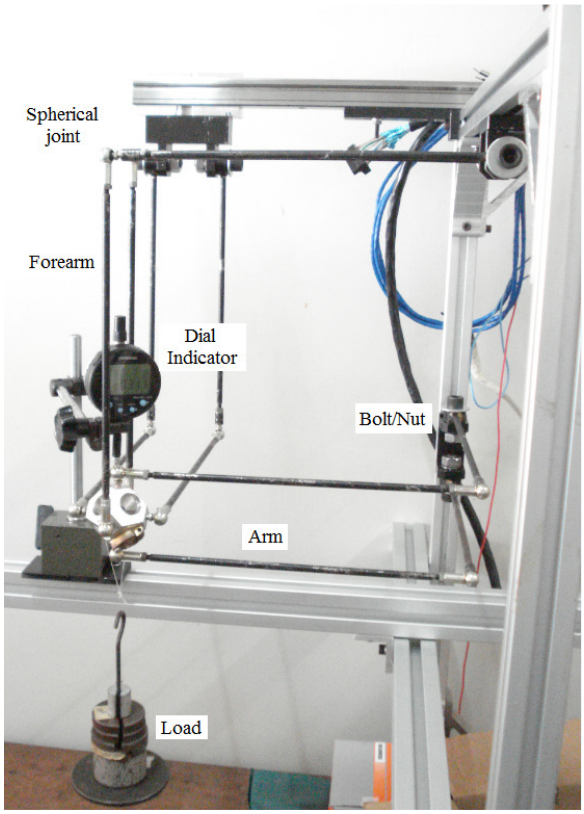

Figure 9 Layout for Experimental stiffness tests of 6-RSS using a dial indicator.

Table V - Computed displacements of node 4 for $\alpha_1=\alpha_2=\alpha_3=\alpha_4=\alpha_5=\alpha_6=0°$ (Forces are given in [N] and torques in [Nm])

U		δ_x [m]	δ_y [m]	δ_z [m]	ϕ_x [rad]	ϕ_y [rad]	ϕ_z [rad]
$F_e=(10,0,0)$	MSA	0.002168	-0.000532	-0.000532	0.000857	0.001701	-0.005384
$M_e=(0,0,0)$	FEA	0.002173	-0.000534	-0.000534	0.000854	0.001727	-0.005378
$F_e=(0,10,0)$	MSA	-0.000532	0.002168	-0.000532	-0.005384	0.000857	0.001701
$M_e=(0,0,0)$	FEA	-0.000534	0.002173	-0.000534	-0.005378	0.000854	0.001727
$F_e=(0,0,10)$	MSA	-0.000532	-0.000532	0.002168	0.001701	-0.005384	0.000857
$M_e=(0,0,0)$	FEA	-0.000534	-0.000534	0.002173	0.001727	-0.005378	0.000854
$F_e=(10,10,10)$	MSA	0.001103	0.001103	0.001103	-0.002826	-0.002826	-0.002826
$M_e=(0,0,0)$	FEA	0.001105	0.001105	0.001105	-0.002796	-0.002796	-0.002796

The results shown in Table VI confirm the validity of the MSA method by which the compliant displacements in the direction of applied force were obtained with an error of less than 9%. Although the FEA and MSA methods use the same equations (29) to (33), the MSA method offers several advantages such as: (a) A robotic structure is composed by links and joints that can be modeled by only two nodes in the MSA method. In contrast, the FEA method needs to divide each link into several nodes. (b) Commercial FEA software do not allow for control of the solver. In contrast, the MSA method allows the assembly of the stiffness matrix to be followed step-by-step. (c) In the FEA method, each change in the structure's configuration requires to redo the mesh, thus increasing the computational cost.
The MSA method requires only an improvement of the inverse kinematic model to map the stiffness of all the configurations of the structure.

Table VI - Measured Compliant displacements of nodes with test-bed in Fig. 3.

Load	δ_y MSA [mm]	Average experimental [mm]	Standard deviation [mm]	Error [%]
Node 17				
P_1	2.136	1.995	0.047	6.6
P_2	2.673	2.696	0.047	0.9
P_3	3.206	3.201	0.049	0.16
Node 11				
P_1	2.250	2.058	0.030	8.5
P_2	2.817	2.736	0.028	2.9
P_3	3.378	3.460	0.004	2.4
Node 5				
P_1	2.062	1.897	0.015	8
P_2	2.581	2.540	0.010	1.7
P_3	3.096	3.260	0.012	5.3
Node 3				
P_1	2.062	2.013	0.004	2.4
P_2	2.581	2.731	0.009	5.8
P_3	3.438	3.663	0.030	6.5

4 CONCLUSIONS

This paper provides a comparison among the main methods for calculating the compliant displacements in robotic structures. In particular, the main available methodologies and formulations have been described and applied to two specific cases of study, namely, a 2 dof serial robotic manipulator and a 6 dof parallel manipulator. The results were compared also through experimental tests.
The experimental results confirm the validity of the MSA and FEA models, that can obtain an accurate estimation of compliant displacements along the direction of applied force.
MSA method is found to require less computational efforts as compared with FEA also because FEA requires a re-modeling and re-meshing at any robot configuration. Lumped stiffness parameters methods can have lower accuracy, but, they can provide a much quicker analysis of the stiffness performance over the whole robot workspace. It is to note that some lumped parameter and Jacobian methods can require complex preliminary calculations of the kinematics/statics models. Accordingly, these methods should not be used when proper close form equations are not available. Additionally, for the choice of a specific stiffness analysis formulation it plays a key role to identify the desired level of accuracy as well as the components that are seen as minimally contributing to the structure compliance so that they can be considered as negligible.

5 ACKNOWLEDGEMENTS

The authors are thankful to CNPq, CAPES and FAPEMIG for the partial financing support of this research work.

REFERENCES

[1] E.I. Rivin. *Stiffness and Damping in Mechanical Design*. Marcel Dekker Inc., New York,1999.
[2] L.W. Tsai. *Robot Analysis: The Mechanics of Serial and Parallel Manipulators*. John Wiley & Sons, New York, 1999.
[3] W.K. Yoon, T. Suehiro, Y. Tsumaki and M. Uchiyama. Stiffness Analysis and Design of a Compact Modified Delta Parallel Mechanism. *Robotica*, Vol. 22, pp.463-475, 2004.
[4] A.A. Shabana. *Dynamics of Multibody Systems*. John Wiley & Sons, 1989.
[5] D. Deblaise, X. Hernot and P. Maurine. A Systematic Analytical Method for PKM Stiffness Matrix Calculation. *Proc. of IEEE Int. Conf. on Robotics and Automation - ICRA 2006,* 2006.
[6] D. Zhang, F. Xi, C.M. Mechefske and S.Y.T. Lang. Analysis of Parallel Kinematic Machine with Kinetostatic Modeling Method. *Robotics and Computer-Integrated Manufacturing*, Vol. 20, No. 02, pp.151-165, 2004.
[7] F. Majou, C.M. Gosselin, P. Wenger and D. Chablat. Parametric Stiffness Analysis of the Orthoglide. *Proc. of the 35th Int. Symp. on Robotics*, Paris, 2004.
[8] O. Company, F. Pierrot and J.C. Fauroux. A Method for Modeling Analytical Stiffness of a Lower Mobility Parallel Manipulator. *Proc. of IEEE ICRA: Int. Conf. on Robotic and Automation*, Barcelona, Spain, 2005.
[9] M. Ceccarelli and G. Carbone. A Stiffness Analysis for CaPaMan (Cassino Parallel Manipulator). *Mechanism and Machine Theory*, Vol. 37, pp.427-439, 2002.
[10] T. Komatsu, M. Uenohara, S. Iikura, H. Miura and I. Shimoyama. Compliance Control for a Two-Link Flexible Manipulator. *The Japan Society of Mechanical Engineers (in Japanese)*, 1990.

[11] T. Komatsu, M. Uenohara, S. Iikura, H. Miura and I. Shimoyama. Dynamic Control for Two-Link Flexible Manipulator. *The Japan Society of Mechanical Engineers (in Japanese)*, 1989.

[12] T. Komatsu, M. Uenohara, S. Iikura, H. Miura and I. Shimoyama. Vibration Control for Two-Link Flexible Manipulator using a Wrist Force Sensor. *The Japan Society of Mechanical Engineers (in Japanese)*, 1990.

[13] W.K. Yoon, T. Suehiro, Y. Tsumaki and M. Uchiyama. Stiffness Analysis and Design of a Compact Modified Delta Parallel Mechanism. *Robotica*, Vol. 22, pp. 463-475, 2004.

[14] W.K. Yoon, T. Suehiro, Y. Tsumaki and M. Uchiyama. A Method for Analyzing Parallel Mechanism Stiffness Including Elastic Deformations in the Structure. *Proc. of the IEEE/RSJ Int. Conf. on Intelligent Robots and Systems IROS'02*, Lausanne, pp. 2875-2880, 2002.

[15] M. Ceccarelli, *Fundamentals of Mechanics of Robotic Manipulation*, Kluwer, Dordrecht, 2004.

[16] J.S. Przemieniecki. *Theory of Matrix Structural Analysis*. Dover Publications, Inc, New York, 1985.

[17] W. Dong, Z. Du and L. Sun. Stiffness Influence Atlases of a Novel Flexure Hinge-Based Parallel Mechanism with Large Workspace. *Proc. of IEEE ICRA: Int. Conf. on Robotic and Automation*, Barcelona, Spain, 2005.

[18] R.S. Gonçalves and J.C.M. Carvalho. Singularities of Parallel Robots Using Matrix Structural Analysis. *Proc. of the XIII Int. Symp. on Dynamic Problems of Mechanics*, Angra dos Reis, RJ, Brazil, 2009.

[19] R.S. Gonçalves, Estudo de Rigidez de Cadeias Cinemáticas Fechadas (*Stiffness Analysis of Closed Loop Kinematic Chains*). Universidade Federal de Uberlândia. Thesis (in Portuguese), 2009.

[20] R.S. Gonçalves and J.C.M. Carvalho. Stiffness Analysis of Parallel Manipulator Using Matrix Structural Analysis. *EUCOMES 2008*, 2nd European Conf. on Mechanism Science, Cassino, Italy, 2008.

[21] B.C. Bouzgarrou, J.C. Fauroux, G. Gogua and Y. Heerah. Rigidity Analysis of T3R1 Parallel Robot with Uncoupled Kinematic. *Proc. of the 35th Int. Symp. on Robotics*, Paris, France, 2004.

[22] C. Corradini, J.C. Fauroux, S. Krut and O. Company. Evaluation of a 4 Degree of Freedom Parallel Manipulator Stiffness. *Proc. of the 11th Word Cong. In Mechanism & Machine Science, IFTOMM 2004*, Tianjin, China, 2004.

[23] M. Ceccarelli. A Stiffness Analysis for CaPaMan. Proc. of Conf. on New Machine Concepts for Handing Manufacturing Device on the Basis of Parallel Structures, *VDI 1427*, Braunschweig, pp. 67-80, 1998.

[24] G. Carbone, H.O. Lim, A. Takanishi and M. Ceccarelli. Stiffness Analysis of the Humanoid Robot WABIAN-RIV: Modelling. *IEEE Int. Conf. on Robotics and Automation ICRA 2003*, Taipei, paper ID10615, 2003.

[25] C.M. Clinton, G. Zhang, and A.L. Wavering. Stiffness Modeling of a Stewart-Platform-Based Milling Machine. *In Trans. of the North America Manufacturing Research Institution of SME*, Vol. 25, pp. 335-340, Lincoln, 1997.

[26] T. Huang, X. Zhao, and D.J. Whitehouse. Stiffness Estimation of a Tripod-Based Parallel Kinematic Machine, *IEEE Trans. on Robotics and Automation*, Vol. 18, No. 1, 2002.

[27] G.D.L. Soares Jr, J.C.M. Carvalho and R.S. Gonçalves, Stiffness Analysis of multibody systems using matrix structural analysis MSA. *Robotica*, pp. 1-18, 2015

[28] S.C. Brenner and L.R. Scott. *The Mathematical Theory of Finite Element Methods*, Texts in Applied Mathematics, Vol. 15, Springer, 2008.

[29] Z. Zhou, J. Xi and C.K. Mechefske. Modeling of a Fully Flexible 3PRS Manipulator for Vibration Analysis, *Journal of Mechanical Design*, Vol. 128, pp. 403-412, 2006.

[30] D. Deblaise. *Contribution à la Modélisation et à L'étalonnage Elasto-Géométriques des Manipulateurs à Structure Parallèle*, Thesis, INSA Rennes, 2006.

[31] P. Kobel and R. Clavel. Micro Robot for Rotary Desktop Assembly Line. *Proc. of IEEE International Symposium on Assembly and Manufacturing,* 2011.

[32] J. Aginaga, I. Zabalza, O. Altuzarra and J. Nájera. Improving Static Stiffness of the 6-RUS Parallel Manipulator Using Inverse Singularities. *Robotics and Computer-Integrated Manufacturing* 28, Spain, 2012.

[33] A. Rezaei, A. Akbarzadeh and M. Akbarzadeh. An Investigation on Stiffness of a 3-PSP Spatial Parallel Mechanism with Flexible Moving Platform Using Invariant Form. *Mechanism and Machine Theory* 51, 2012.

[34] B.S. El-Khasawneh and P.M. Ferreira. Computation of Stiffness and Stiffness Bounds for Parallel Link Manipulator. *Int. J. Machine Tools & Manufacture*, Vol. 39, No. 02, pp. 321-342, 1999.

[35] Y.W. Li, J.S. Wang and L.P. Wang. Stiffness Analysis of a Stewart Platform-Based Parallel Kinematic Machine, *Proc. of IEEE ICRA: Int. Conf. on Robotics and Automation*, Washington, US, 2002.

[36] Q. Liang, D. Zhang, Z. Chi, Q. Song and Y. Ge. Six-dof Micro-Manipulator Based on Compliant Parallel Mechanism with Integrated Force Sensor. *Robotics and Computer-Integrated Manufacturing* 27, China, 2011.

[37] A. Taghvaeipour, J. Angeles and L. Lessard. Online Computation of the Stiffness Matrix in Robotic Structures Using Finite Element Analysis. *Department of Mechanical Engineering and Centre for Intelligent Machines*, McGill University, Canada, 2010.

[38] J. Li. *Design of 3-DOF Parallel Manipulators for Micro-Motion Applications*. Master's Thesis, University of Ontario Institute of Technology, Canada, 2009.

[39] F.P. Beer, E.R. Johnston, J.T. De Wolf and D.F. Mazurek. *Mechanics of Materia*l, 5th Ed., United States, 2009.

[40] G. Carbone, Stiffness Analysis and Experimental Validation of Robotic Systems, *Frontiers of Mechanical Engineering*, Vol. 06, No. 02, pp. 182-196, 2011.

[41] G. Carbone, M. Ceccarelli, A comparison of indices for stiffness performance evaluation, *Frontiers of Mechanical Engineering in China*, Vol.5, No.3, pp. 270-278, 2010.

ISSN 1590-8844
International Journal of Mechanics and Control, Vol. 17, No. 02, 2016

BEHAVIOUR OF A LIGHTWEIGHT EXTERNAL WALL UNDER MEDITERRANEAN CLIMATIC CONDITIONS

Luigi A. Besalduch* Roberto Ricciu* Andrea Manuello Bertetto**

* Department of Civil and Environmental Engineering and Architecture
University of Cagliari - Italy

** Department of Mechanical Engineering, Chemical and Materials
University of Cagliari - Italy

ABSTRACT

The increasing development and use of new lightweight building technologies makes more urgent the evaluation of their energy performance. It is even more necessary in climatic contexts, like the Mediterranean basin, in which the effect of the solar radiation during the summer period should be lessened by high thermal masses. The study here presented deals with the assessment of thermal performance of an opaque envelope designed and built in Sardinia in 2013. The study is focused on the measurement the dynamic parameters of prebuilt wall, made of OSB panels and cellulose. The measurement is compared with the minimum requirements of Italian national standards. The analysis was carried out using a climatic chamber settled in the laboratories of the University of Cagliari. The chamber consists of two shells that create on both faces of a full-scale wall different hygro-thermal conditions. One of the shell simulates the external conditions while the other ones. The data were acquired to measure the heat storage capacity of the specimen, and then the dynamic parameters were calculated according to the EN ISO 13786:2008.

Keywords: lightweight walls, specific heat capacity, thermal transmittance, cellulose loose-fill, thermal dynamic parameters

1 INTRODUCTION

Lightweight materials are an interesting technology for building envelope. If prebuilt they can solve constructive problems and can help to reduce the use of heavy and energy consuming materials for the building bearing elements [1]. However their performances in mild climate, like the Mediterranean one [2], are far to be completely established. Italian legislation sets minimum requirements for periodic thermal transmittance and give a classification for thermal decrement and time lag. These values generally are calculated according to international standards as the EN ISO 13786.
Input data do not limit only to thermal conductivity, but also specific heat and density have to be correctly assessed. As shown in the following, especially the first one, requires complex measurements and the literature data, even for the same material, are not coincident.
In this paper, the measurements of thermal conductivity and specific heat of a wood based envelope are described. They have been carried out through the use of a dedicated climatic chamber. The results are then discussed and compared with Italian legislation requirements [3].

Contact author: Roberto Ricciu[1]

[1] Email: ricciu@unica.it.

2 METHODOLOGY

2.1 CASE STUDY

The sample analyzed is representative of an opaque envelope of a newly constructed wall. In particular the case study corresponds to the construction technology of a residential building, located in northern Sardinia. The building is surrounded by a ventilated woodlands at an altitude of approximately 200 m above sea level. The site is classified in climatic zone C with 1142 DD and an

horizontal solar radiation, during the worst month of the year, I_r=326 W/m^2. The construction consist of platform frame with a steel framework and two OSB plastered panels filled of insufflated cellulose fibers. This is a dry construction method increasingly used, because it permits a fast construction and maximizes steady state thermal properties. The value of thermal transmittance equal to 0,14W/m^{2}K, reached by the envelope for its opaque vertical components, is a high performance level both for a new construction – in a Mediterranean climate – and for an existing building in similar climatic conditions. Considering this value, the technical solution used allows a suitable level of indoor comfort, with a correct balance between the building-enclosure and building-system appliances during wintertime. The relevant question is whether so low thermal transmittance values, accomplishing the limits prescribed by the current legislation, will allow is possible to obtain the same results in the summertime. The envelope is characterized by an areal density M_s=50,7kg/m^2, does not comply with legislative prescriptions regarding surface thermal mass for vertical structural components, but could give a value of periodic thermal transmittance that meets the prescriptions (Y_{ie}=0,12W/m^{2}K).

The inertial behaviour of the thermal envelope is extremely important, in relation to the climatic context, to guarantee the indoor comfort, without needing to overestimate the power of the cooling systems. For this reason, due to the crucial role of the dynamic parameters of the cellulose fiber, a study on this material was carried out.

Determining the actual value of specific heat is not a simple task for the specimen in question. This because cellulose fiber is an extremely porous material, characterized by a low conductivity, and, because of its low density, a low thermal capacity. Cellulose fibers, together with other natural fibers such as wood wool, have already been objects of studies mainly focusing on their fire resistance class.

To determine the specific heat capacity a large number of methods are applied, some of them use very small specimens (i.e. calorimetric methods [4]), that are not representative of real walls. Other are based on the differential thermal analysis (DTA) technique [5] or need an elaborate theoretical analysis of the measured data with idealized boundary conditions [6, 7] Other techniques are the photothermal or photoacoustic ones [8], or transient method using an heat flow meter apparatus (HFM) [9]. In this paper is present a novel easier method to determine the specific heat capacity of real walls, through heat flux meters.

3 EXPERIMENTS

3.1 EXPERIMENTAL SET-UP

The climatic simulation chamber (Fig. 1) used for these analyses, allows testing the full-scaled walls with imposed inner and outer wall climatic conditions [10] and it is designed according to the EN 1934:2000 [11], ISO 9869:1994 [12] and EN 12494:1996 [13] standards.

The apparatus consists of two chambers that fully control the temperature, relative humidity and air velocity and a frame that hosts the specimen.

3.2 TEST SPECIMEN

The test specimen is made by a cellulose based material confined with two OBS panels, 2240 mm high, 1250 mm wide and 395 mm thick (Fig. 2). The cellulose between the two panels was blown until reaching a density of 60 kg/m³. The declared values for the thermal conductivity and the specific heat capacity of this material are respectively 0,038 W/mK and 2544 J/kgK. While instead for the OSB are respectively 0,13 W/mK and 1700 J/kgK, the density is 600 kg/m³.

The specimen was inserted into a frame of XPS having the same depth to minimize the lateral heat dispersion.

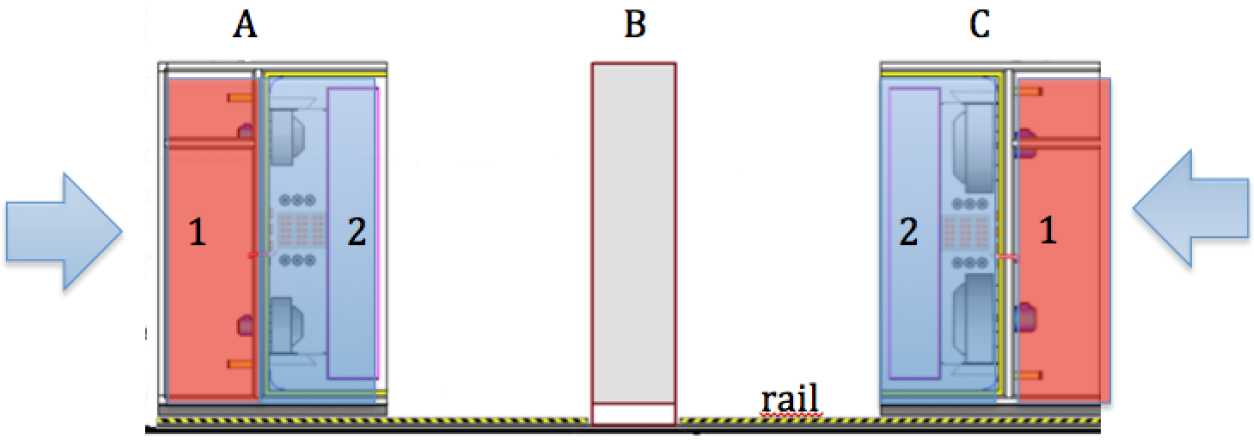

Figure 1 Climatic chamber, vertical section. (A) Indoor chamber, (C) Outdoor Chamber. The specimen is contained in a frame (B) between the two chamber.1 is the compartment electrical control system, 2 is the air handling compartment. The arrows indicate that the chamber A and C move on rails (dashed yellow line at the base of the chamber).

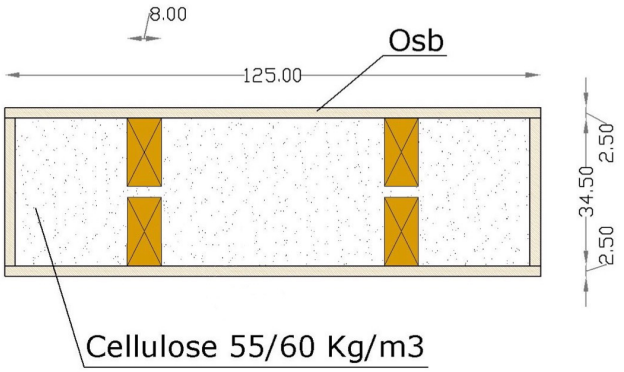

Figure 2 Test specimen (dimensions in cm).

3.3 EXPERIMENTAL METHOD

The test wall is instrumented by means of RTD (resistive temperature detector) sensors for the surface temperature measurement, NTC (negative temperature coefficient) thermistors for the air temperature and heat-flux sensors to measure the surface temperature and heat-flux.

The heat flux sensor is the FE01-3B model. The primary sensing element is a cylindrical thermopile sensor. The contact surface has got an 80 mm radius and its thickness is 5,5 mm. The main metrological characteristics are: span (measurement field): −300 to 300 W/m^2; resolution 0,01 W/m2 ; unbias: ±5%.

The measuring chain is also composed of wireless wiring in the ISM 2,4 GHz band and is compatible with the IEEE 802.15.4 protocol. The system also includes a data logger with an integrated RAM. The main metrological characteristic software and data logger are: resolution 16 bit, 30 channels and maximum sampling speed is 1 min on each of the 30 channels.

In order to obtain sufficient data, fourteen RTD sensors and four heat-flux sensors (which also include four temperature thermopile sensors) are fixed. A sample measurement rate of 5 minutes is chosen, taking into account the velocity variation of the environmental parameters measured. Surface temperatures and heat-flux output data are returned by a wireless data logger, while air temperatures in the two chambers Are measured through TGU2 data loggers. The data are subsequently transferred and processed through dedicated spreadsheets. The instrument scheme is shown in Figure 3.

The method requires the measurement of surface temperatures and heat-flux through the specimen by the use of heat-flux meters, [14, 15]. All sensors and measurement systems are provided with individual calibration certificates by the Italian Calibration Service SIT.

4 EXPERIMENTAL RESULTS

4.1 PRELIMINARY ANALISYS

The first test was aimed at measuring the thermal steady state conductivity. The test was carried out in conditions similar to the winter operating ones.

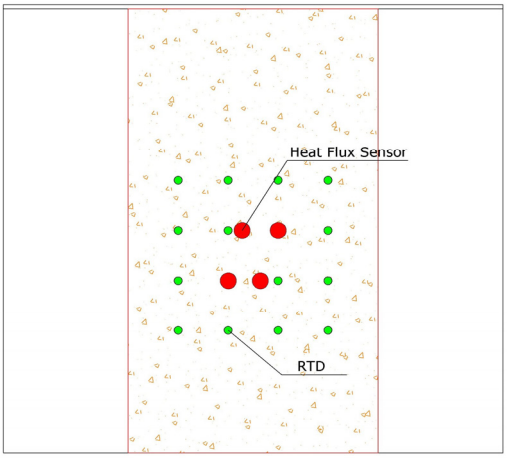

Figure 3 Position of the heat flux sensors (red) and of the RTD (green) in the indoor face.

The details of the environmental parameters are summarized in Table I.

Table I - Simulation conditions

	Indoor Chamber	**Outdoor Chamber**
Air temperature [°C]	22	2
Relative humidity [%]	40	40
Air velocity [m/s]	0,1	1,0

The measurements were carried out maintaining a mean surface temperature difference between the indoor and the outdoor chamber of about 20°C, as in Figure 4.

The heat flux calculated as the surface wall temperature difference became constant (after about 20 hours) maintaining a value approximately of 3,5 W/m²K. A measurement analysis of thermal conductivity was carried out with the progressive means method according to the EN 12494:1996 standard (Figure 5).

The results of the conductance Cs analysis are shown in Figure 5. A peak of 0,105 W/m^{2}K is evident after 8 hours, than after 50 hours, the conductance became constants, assuming a value of approximately 0,145 W/m^{2}K. This value, imposing the declared value for the OSB conductivity (0,130 W/mK), was used to determine the thermal conductivity of the cellulose (0,054 W/mK), different from the declared value, but similar to [16] that found a value of 0,050 W/mK.

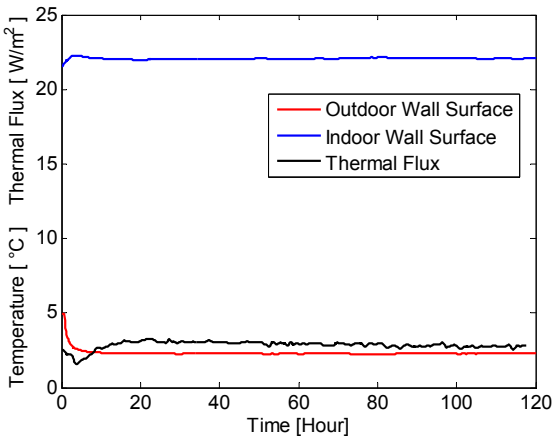

Figure 4 Surface walls temperature in the indoor (blue line) and outdoor (red line) chamber, and thermal flux (black line).

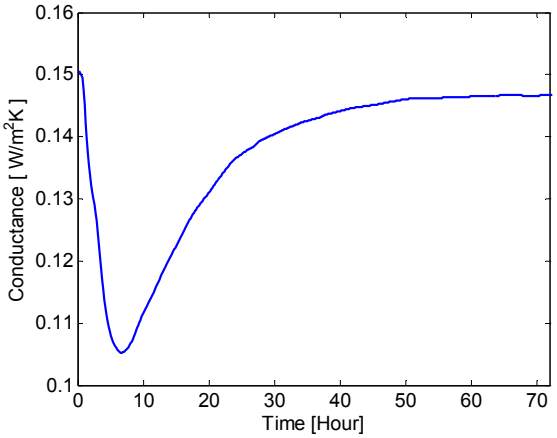

Figure 5 Evolution of conductance measured.

4.2 DETERMINATION OF THE SPECIFIC HEAT CAPACITY OF THE SPECIMEN

In this paper on use an original simple method to calculate the heat capacity throw heat flux meters.

The test began with the following environmental conditions: air temperature: about 40 °C and air velocity about 1 m/s, the relative humidity was set to 22%. Such conditions remained for approximately 10 days, in order to allow the evaporation of the residual humidity, and an isotropic thermal distribution inside the specimen.

Then the indoor and outdoor chambers were brought to 25°C, and the humidity to 50% (to maintain the same vapour pressure between the two faces of the specimen) (Fig. 6). The test run until the temperature variation of the specimen became negligible.

Calculating the heat capacity was calculated as the integral of the thermal flux (Q) measured by heat flux meters, divided by the areal density of the specimen (m), and by the temperature difference (Δt):

$$C = \frac{\int Q}{m \cdot \Delta T} \tag{1}$$

a specific heat of 1277 J/kgK has been evaluated.

4.3 DYNAMIC PARAMETERS UNDER THE EN ISO 13786

The results both for steady state and dynamic analysis are summarized in Table II, where the equivalent wall is a homogeneous wall with the same parameters of the specimen.

Table II - Wall parameters

	s [cm]	λ [W/m²K]	C [J/kgK]	ρ [kg/m³]
Equivalent Wall	39,5	0,0572	1277	128,35

With these data it is possible to evaluate the dynamic characteristics according to [17, 18] (Table III).

Table III - Dynamic values calculated

Thermal transmittance (U)	0,141	[W/(m²K)]
Periodic thermal transmittance (Yie)	0,026	[W/(m²K)]
Thermal lag	11,24	[h]
Decrement Factor (fa)	0,187	[-]
Internal thermal admittance	0,765	[W/(m²K)]
External thermal admittance	0,806	[W/(m²K)]
Internal area heat capacity	10,752	[kJ/(m²K)]
External area heat capacity	11,303	[kJ/(m²K)]

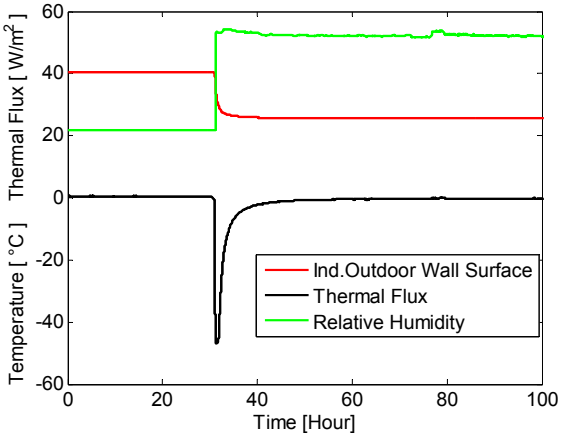

Figure 6 Surface wall temperature in the indoor and outdoor chamber (red line), Thermal Flux (black line) and Relative Humidity (green line).

5 CONCLUSIONS

The tests carried out assessed the thermo-physical values of a light construction technique highlighting both its static and dynamic characteristics. The calculated value of thermal conductance conforms with the performance standards of natural insulating materials present on the currently market. In steady state conditions the tests on the thermal transmittance value of the opaque wall give a good efficiency result, close to the standards for low energy dwellings. The tests on the dynamic parameters allow us to confirm a high specific heat value, which nonetheless, even in the absence of a high volume mass, guarantees sufficient value of thermal lag. The Italian guidelines for energy certification of buildings define the optimal qualitative evaluation for an opaque envelope as being longer than 12h, with an decrement factor below 0,15. The building solution analysed can be classified between the average and sufficient class (II<class<III).

ACKNOWLEDGMENT

The authors wish to thank all ICHNOS19 staff (Ischnos srl Cagliari – Italy), in particular ingg. Fabio Demontis, Silvio Pistis, Mauro Solinas and Mauro Medici for the specimen set-up, Arch. Stefania di Benedetto Ph.D. and Ing. Giuseppe Desogus Ph.D. for their contribute to the Mediterranean Energy Forum in Marrakesh (Marocco), 26-28 March 2015. The testing apparatus was financed by Sardinian Regional Government under the LABMAST project.

REFERENCES

[1] Desogus, G., Di Pilla, L., Mura, S., Pisano, G.L., Ricciu, R., Economic efficiency of social housing thermal upgrade in Mediterranean climate, Energy and Buildings, 57, pp. 354-360, 2013.

[2] Ciulla, G., Galatioto, A., Ricciu, R., Energy and economic analysis and feasibility of retrofit actions in Italian residential historical buildings, Energy and Buildings, 128, pp. 649-659, 2016.

[3] Di Pilla, L., Desogus, G., Mura, S., Ricciu, R., Di Francesco, M., Optimizing the distribution of Italian building energy retrofit incentives with Linear Programming, Energy and Buildings, 112, pp. 21-27, 2016.

[4] ASTM International, " Standard ASTM C 351-82, Standard Test Method for Mean Specific Heat of Thermal Insulation", 1982.

[5] ASTM International, " Standard ASTM E 1356-91, Standard Test Method for Glass Transition Temperature by Differential Scanning calorimetry or Differential Thermal Analysis", 1991.

[6] A. Bouguerra, A. Ait-Mokhtar, O. Amiri, M.B. Diop, "Measurement of thermal conductivity thermal diffusivity and heat capacity of highly porous building materials using transient plane source technique", Int. Comm. Heat Mass Transfer, vol. 28 (8), pp. 1065 - 1078, 2001.

[7] T. Harada, T. Hata, S. Ishihara, "Thermal constants of wood during the heating process measured with the laser flash method", Journal of Wood Science, vol. 44, pp. 425-431, 1998.

[8] G. Leon, J. Cruz-de-Leon, L. Villasenor, "Thermal characterization of pine wood by photoacoustic techniques", Holz als Roh-und Werkstoff, vol. 58, pp. 241-246, 2000.

[9] K. Ghazi Wakili, B. Binder, R. Vonbank, "A simple method to determine the specific heat capacity of thermal insulation used in building construction", Energy and Building, vol. 35, pp. 413-415, 2003.

[10] S. Ferrari, V. Zanotto, "The thermal performance of walls under actual service conditions: Evaluating the results of climatic chamber tests", Construction and Building Materials, vol. 43, pp. 309-316, 2013.

[11] European Committee for Standardization, "Standard EN 1934, Determination of thermal resistance by hot box method using heat flow meter", 2000.

[12] International Standard Organization, "Standard ISO 9869, Thermal insulation - building elements - in situ measurement of thermal resistance and thermal transmittance", 1994.

[13] European Committee for Standardization, "Standard PREN 12494:1996, Building components and elements - in-situ measurement of the surface-to-surface thermal resistance", 1996.

[14] G. Desogus, S. Mura, R. Ricciu, "Comparing different approach to in situ measurement of building components thermal resistance", Energy and Buildings, vol. 43, pp. 2613-2620, 2011.

[15] Pia, G., Casnedi, L., Ricciu, R., (...), Meloni, P., Sanna, U., Thermal properties of porous stones in cultural heritage: Experimental findings and predictions using an intermingled fractal units model, Energy and Buildings, 118, pp. 232-239, 2016.

[16] A. Nicolajsen, "Thermal transmittance of a cellulose loose-fill insulation material", Building and Environment, vol. 40, pp. 907-914, 2005.

[17] International Standard Organization, "Standard ISO 13786, Thermal performance of building components, Dynamic thermal characteristics, Calculation methods", 2008.

[18] Beccali, M., Galatioto, A., Leone, G., Longo, S., Is the NZEB benchmarking approach suitable for assessing energy retrofit design?, Applied Mechanics and Materials, 361-363, pp. 402-407, 2013.

ISSN 1590-8844
International Journal of Mechanics and Control, Vol. 17, No. 02, 2016

TEMPLATE FOR PREPARING PAPERS FOR PUBLISHING IN INTERNATIONAL JOURNAL OF MECHANICS AND CONTROL

Author1* Author2**

* affiliation Author1

** affiliation Author2

ABSTRACT

This is a brief guide to prepare papers in a better style for publishing in International Journal of Mechanics and Control (JoMaC). It gives details of the preferred style in a template format to ease paper presentation. The abstract must be able to indicate the principal authors' contribution to the argument containing the chosen method and the obtained results. (max 200 words)

Keywords: keywords list (max 5 words)

1 TITLE OF SECTION (E.G. INTRODUCTION)

This sample article is to show you how to prepare papers in a standard style for publishing in International Journal of Mechanics and Control.
It offers you a template for paper layout, and describes points you should notice before you submit your papers.

2 PREPARATION OF PAPERS

2.1 SUBMISSION OF PAPERS

The papers should be submitted in the form of an electronic document, either in Microsoft Word format (Word'97 version or earlier).
In addition to the electronic version a hardcopy of the complete paper including diagrams with annotations must be supplied. The final format of the papers will be A4 page size with a two column layout. The text will be Times New Roman font size 10.

Contact author: author1[1], author2[2]

[1]Address of author1.
[2]Address of author2 if different from author1's address
E-mail: author1@univ1.com , author2@univ2.com

2.2 DETAILS OF PAPER LAYOUT

2.2.1 Style of Writing

The language is English and with UK/European spelling. The papers should be written in the third person. Related work conducted elsewhere may be criticised but not the individuals conducting the work. The paper should be comprehensible both to specialists in the appropriate field and to those with a general understanding of the subject.
Company names or advertising, direct or indirect, is not permitted and product names will only be included at the discretion of the editor. Abbreviations should be spelt out in full the first time they appear and their abbreviated form included in brackets immediately after. Words used in a special context should appear in inverted single quotation mark the first time they appear. Papers are accepted also on the basis that they may be edited for style and language.

2.2.2 Paper length

Paper length is free, but should normally not exceed 10000 words and twenty illustrations.

2.2.3 Diagrams and figures

Figures and Tables will either be entered in one column or two columns and should be 80 mm or 160 mm wide respectively. A minimum line width of 1 point is required at actual size. Captions and annotations should be in 10 point with the first letter only capitalised *at actual size* (see Figure 1 and Table VII).

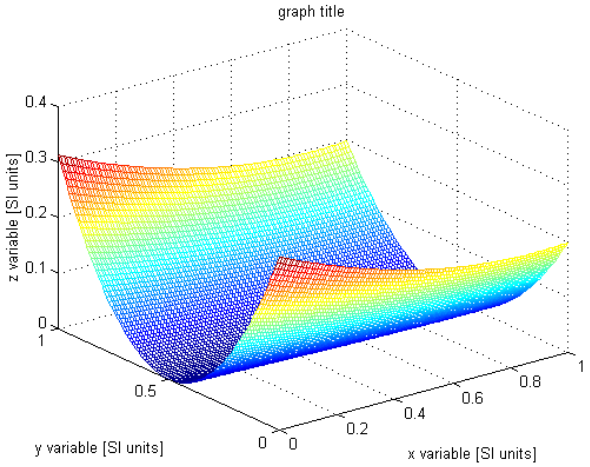

Figure 1 Simple chart.

Table VII - Experimental values

Robot Arm Velocity (rad/s)	Motor Torque (Nm)
0.123	10.123
1.456	20.234
2.789	30.345
3.012	40.456

2.2.4 Photographs and illustrations

Authors could wish to publish in full colour photographs and illustrations. Photographs and illustrations should be included in the electronic document and a copy of their original sent. Illustrations in full colour …

2.2.5 Equations

Each equation should occur on a new line with uniform spacing from adjacent text as indicated in this template. The equations, where they are referred to in the text, should be numbered sequentially and their identifier enclosed in parenthesis, right justified. The symbols, where referred to in the text, should be italicised.

- point 1
  - point 2
    - point 3

1. numbered point 1
   2. numbered point 2
      3. numbered point 3

$$W(d) = G(A_0, \sigma, d) = \frac{1}{T}\int_0^{+\infty} A_0 \cdot e^{-\frac{d^2}{2\sigma^2}} dt \qquad (1)$$

3 COPYRIGHT

Authors will be asked to sign a copyright transfer form prior to JoMaC publishing of their paper. Reproduction of any part of the publication is not allowed elsewhere without permission from JoMaC whose prior publication must be cited. The understanding is that they have been neither previously published nor submitted concurrently to any other publisher.

4 PEER REVIEW

Papers for publication in JoMaC will first undergo review by anonymous, impartial specialists in the appropriate field. Based on the comments of the referees the Editor will decide on acceptance, revision or rejection. The authors will be provided with copies of the reviewers' remarks to aid in revision and improvement where appropriate.

5 REFERENCES (DESCRIPTION)

The papers in the reference list must be cited in the text. In the text the citation should appear in square brackets [ ], as in, for example, "the red fox has been shown to jump the black cat [3] but not when...". In the Reference list the font should be Times New Roman with 10 point size. Author's first names should be terminated by a 'full stop'. The reference number should be enclosed in brackets.

The book titles should be in *italics*, followed by a 'full stop'. Proceedings or journal titles should be in *italics.* For instance:

REFERENCES (EXAMPLE)

[1] Smith J., Jones A.B. and Brown J., *The title of the book*. 1st edition, Publisher, 2001.

[2] Smith J., Jones A.B. and Brown J., The title of the paper. *Proc. of Conference Name*, where it took place, Vol. 1, paper number, pp. 1-11, 2001.

[3] Smith J., Jones A.B. and Brown J., The title of the paper. *Journal Name*, Vol. 1, No. 1, pp. 1-11, 2001.

[4] Smith J., Jones A.B. and Brown J., *Patent title*, U.S. Patent number, 2001.

International Journal of Mechanics and Control – JoMaC
Published by Levrotto&Bella
TRANSFER OF COPYRIGHT AGREEMENT

NOTE: Authors/copyright holders are asked to complete this form signing section A, B or C and mail it to the editor office with the manuscript or as soon afterwards as possible.	*Editor's office address:* Andrea Manuello Bertetto Matteo D. L. Dalla Vedova *Dept. of Mechanical and Aerospace Engineering* *Politecnico di Torino* *C.so Duca degli Abruzzi, 24 – 10129 Torino – Italy* *e_mail: jomac@polito.it* *fax n.: +39.011.564.6999*

The article title:

By:_____

To be Published in ***International Journal of Mechanics and Control JoMaC***
Official legal Turin court registration Number 5320 (5 May 2000) - reg. Tribunale di Torino N. 5390 del 5 maggio 2000

A Copyright to the above article is hereby transferred to the JoMaC, effective upon acceptance for publication. However the following rights are reserved by the author(s)/copyright holder(s):
1. All proprietary rights other than copyright, such as patent rights;
2. The right to use, free or charge, all or part of this article in future works of their own, such as books and lectures;
3. The right to reproduce the article for their own purposes provided the copies are not offered for sale.

To be signed below by all authors or, if signed by only one author on behalf of all co-authors, the statement A2 below must be signed.

A1. All authors:

SIGNATURE_____DATE_____ SIGNATURE_____DATE_____

PRINTED NAME_____ PRINTED NAME_____

SIGNATURE_____DATE_____ SIGNATURE_____DATE_____

PRINTED NAME_____ PRINTED NAME_____

A2. One author on behalf of all co-authors:
"I represent and warrant that I am authorised to execute this transfer of copyright on behalf of all the authors of the article referred to above"

PRINTED NAME_____

SIGNATURE_____ TITLE_____ DATE_____

B. The above article was written as part of duties as an employee or otherwise as a work made for hire. As an authorised representative of the employer or other proprietor. I hereby transfer copyright to the above article to *International Journal of Mechanics and Control* effective upon publication. However, the following rights are reserved:
1. All proprietary rights other than copyright, such as patent rights;
2. The right to use, free or charge, all or part of this article in future works of their own, such as books and lectures;
3. The right to reproduce the article for their own purposes provided the copies are not offered for sale.

PRINTED NAME_____

SIGNATURE_____ TITLE_____ DATE_____

C. I certify that the above article has been written in the course of employment by the United States Government so that no copyright exists, or by the United Kingdom Government (Crown Copyright), thus there is no transfer of copyright.

PRINTED NAME_____

SIGNATURE_____ TITLE_____ DATE_____

CONTENTS

next issue titles will be from the papers of:

RAAD 2016

26th International Conference on Robotics in Alpe-Adria-Danube Region

Torino, Italy
21 – 23 June 2017

Scopus Indexed Journal

Reference Journal of IFToMM Italy
International Federation for the Promotion
of Mechanism and Machine Science